

Reduction of TCE and Chromate by Granular Iron in the Presence of Dissolved CaCO₃

by
YanQi Yang

A thesis
presented to the University of Waterloo
in fulfillment of the
thesis requirement for the degree of
Master of Science
in
Earth Sciences

Waterloo, Ontario, Canada, 2006

©YanQi Yang 2006

Author's Declaration

I hereby declare that I am the sole author of this thesis. This is a true copy of the thesis, including any required final revisions, as accepted by my examiners.

I understand that my thesis may be made electronically available to the public.

Abstract

Iron permeable reactive barriers (PRBs) have been installed at sites contaminated with various reducible organic and inorganic chemicals, particularly chlorinated solvents, worldwide. Many geochemical factors can affect the performance of iron PRBs. Chemicals such as nitrate and Cr(VI) may act as competing oxidants when co-exist with chlorinated solvents. Previous studies observed declines in the rate of TCE degradation by granular iron in the presence of nitrate. Passive oxide formation on the iron surface and an increase in corrosion potential of the iron were determined to be the mechanisms for the decline. Cr(VI), being a stronger oxidant than nitrate, may have a similar but greater effect on the iron reactivity. In addition, chromium oxide as well as dissolved CaCO₃, a common groundwater constituent, form secondary precipitates and are likely to further affect the iron reactivity. The primary objective of this study was to determine the effects of Cr(VI) and dissolved CaCO₃ on the iron reactivity towards TCE and Cr(VI) reduction and to provide mechanistic explanations for the observation. In addition, the applicability of a modified reactive transport model (Jeen, 2005) to the system in which chromate and CaCO₃ co-exist with TCE was evaluated.

Column experiments, including measurements of corrosion potential and surface film composition using Raman spectroscopy were conducted. Five column tests were carried out with input solutions consisting of different combinations of TCE (5 mg/L), Cr(VI) (10 mg/L) and dissolved CaCO₃ (300 mg/L) for eight months.

The results from the column receiving only Cr(VI) showed that Cr(VI) was reduced rapidly by the granular iron and was not detected beyond 10 cm from the influent end of the column by the end of the experiment. However, Cr(VI) profiles migrated from the influent end further into the column overtime, suggesting progressive passivation of the iron near the influent end of the column. The gradual increase in corrosion potential (up to 180 mV positive shift) at the port 3 cm from the inlet with the migration of Cr(VI) profiles suggests the formation and accumulation of higher valent iron oxides, such as hematite and goethite, together with Cr(III) products on the iron surface, passivating iron material. Raman spectroscopic measurements confirmed the presence of passive iron oxides at the end of the experiment. For the column receiving Cr(VI) + TCE, the co-existence of TCE did not affect Cr(VI) reduction kinetics. However, the presence of Cr(VI) affected TCE degradation significantly. Two segments in the migration of TCE profiles are identified: the first segment near the influent end of the column, where the iron was still active towards Cr(VI) reduction

but inactive towards TCE degradation, and the second segment where Cr(VI) was fully removed and the TCE degradation continued to follow pseudo-first-order kinetics. The migrations in Cr(VI) and TCE profiles suggest that iron was passivated by Fe(III)/Cr(III) products, and Cr(VI), being a stronger oxidant, was reduced much more rapidly than TCE. It is expected that the first segment of TCE profiles would extend gradually with the migration of Cr(VI) profiles over time.

When dissolved CaCO₃ was added to the columns with Cr(VI) and TCE, either as single contaminant, or as co-contaminants, the pH values near the influent end of the columns remained relatively low (~ pH 7), thus, the presence of dissolved CaCO₃ resulted in a stable corrosion potential and faster degradation rates of TCE and Cr(VI). Over time, however, Cr(VI) reduction and iron corrosion produced OH⁻ and shifted the carbonate-bicarbonate equilibrium, resulting in the precipitation of secondary carbonate minerals, as detected by Raman analysis in the three columns containing CaCO₃. The precipitation and accumulation of the secondary minerals on the iron surface gradually decreased iron reactivity, as indicated from the progressive migrations of TCE profiles in the column receiving TCE +CaCO₃ and of second segment TCE of profiles in the column receiving TCE + Cr(VI) + CaCO₃. Over the experimental period, the enhancement of dissolved CaCO₃ was much greater than the iron passivation by secondary mineral precipitates.

Based on the laboratory experiments, Jeen (2005) developed an empirical formula relating the decrease in iron reactivity to the accumulation of secondary minerals, and incorporated this formula into kinetic expression of an existing multi-component reactive transport model (MIN3P). The same code was used in this study to simulate the experimental data. The model reproduced the observations from the columns in which TCE co-exists with Cr(VI) and CaCO₃ quite well, which suggests this model has applicability to predict the long-term performance of an iron PRB when treating groundwater containing Cr(VI), TCE and CaCO₃, though there are some potential areas for improvements, including inconsistent volume fractions of secondary carbonate minerals and Fe(III)/Cr(III) products between experimental measurements and model simulation results, the reactive surface area concept, and inability to adapt changes in iron corrosion rates.

The long-term performance for a hypothetical scenario in using an iron PRB (40 cm thick) to treat groundwater where TCE (5 mg/L) co-exists with Cr(VI) (10 mg/L) in the presence of CaCO₃ (300 mg/L) was simulated. The simulation indicated that Cr(VI) was completely treated over a period of 30 years, however, TCE broke through before 20 years, and substantial porosity was lost due to the accumulation of carbonate precipitates. The prediction could be valuable in the design of PRBs or in

the development of effective maintenance procedures for PRBs treating groundwater co-contaminated with chromate and TCE.

Acknowledgements

The completion of this thesis has been assisted by many people. First, I would like to thank Dr. R. W. Gillham for providing me with the opportunity to conduct this research, and for his understanding and continuous support throughout my study. I would like to express my sincere thanks to Dr. Lai Gui for the guidance, the direction and the trust whenever sought, for help fill the numerous gaps in my knowledge, and for being both a great supervisor and a good friend to me. Many thanks to Dr. David Blowes for reading the manuscript and providing constructive criticism. Special thanks to Dr. S. K. Frape for reviewing the manuscript and for providing helpful comments.

Great thanks go to Dr. Marek Odziemkowski for providing me the assistance and advice, regarding the electrochemical and Raman surface analyses parts of the study. I am grateful to Dr. Sung-Wook Jeon for providing the helpful discussion and advice on the research, particularly answering lots of my questions regarding modeling part of this study.

I can never forget the invaluable technical support of Wayne Nobel in the laboratory. Thanks also to Harsha Jadeja and Randy Fagan for assistance in the laboratory. Many thanks to all the Gillham Group members, it is very enjoyable and such a pleasure to be one number of this group. Special Thanks to Li, June, Pattie, Eva, and Lorretta... , for the conversations about research and many others.

I would like Thank my family, my husband Yunke and son Weizhe, for their sharing both the hard and the good time with me, for their endless love and support for me.

Financial support for this research was provided by the NSERC/duPont/ETI Industrial Research Chair held by Dr. R. W. Gillham. Additional financial supports were provided by University of Waterloo Graduate Entrance Scholarships and University of Waterloo Graduate Student Bursary.

Table of Contents

Author's Declaration	ii
Abstract	iii
Acknowledgements	vi
Table of Contents	vii
List of Tables	x
List of Figures	xi
Chapter 1 Introduction.....	1
1.1 TCE and Cr(VI) as Groundwater Contaminants	1
1.2 Degradation of TCE and Cr(VI) by Granular Iron	2
1.2.1 Effects of Co-existing Oxidants on TCE Reduction.....	2
1.2.2 Reduction of Cr(VI) by Granular Iron.....	5
1.2.3 Secondary Mineral Precipitation	6
1.2.4 Modeling Studies.....	7
1.3 Research Objectives	8
Chapter 2 Methods	9
2.1 Column Experiments	9
2.1.1 Column Design and Packing	9
2.1.2 Solution Preparation and Column Operation.....	10
2.2 Chemical Analyses	11
2.2.1 Organic Analyses.....	11
2.2.2 Inorganic Analyses	13
2.3 In-situ Corrosion Potential Measurements	14
2.4 Raman Spectroscopic Measurements	14
2.4.1 Ex-situ Raman Analysis	14
2.4.2 Identification of Oxide Species and Secondary Minerals on Iron Surface.....	15
Chapter 3 Experimental Results and Discussion.....	20
3.1 Phases I and II	20
3.2 Column A: Cr(VI) as the Only Contaminant.....	22
3.2.1 Reaction Kinetics.....	22
3.2.2 Changes in Corrosion Potential, pH, H ₂ Formation Rate and Hydraulic Conductivity.....	22
3.2.3 Changes in Oxide Films on Iron Surface.....	23

3.3 Column B: Cr(VI) in the Presence of CaCO ₃	31
3.3.1 Reaction Kinetics.....	31
3.3.2 Alkalinity Profiles, pH, Changes of Corrosion Potentials, H ₂ Generation Rate and Hydraulic Conductivity	31
3.3.3 Changes in Oxide Films on Iron Surface.....	32
3.4 Column C: TCE in the Presence of CaCO ₃	39
3.4.1 Reaction Kinetics.....	39
3.4.2 Alkalinity Profiles, pH, Changes of Corrosion Potential, H ₂ Generation Rate and Hydraulic Conductivity	39
3.4.3 Changes in Oxide Films on Iron Surface.....	40
3.5 Column D: TCE Co-existing with Cr(VI).....	46
3.5.1 Reaction Kinetics.....	46
3.5.2 Changes of Corrosion Potential, pH, H ₂ Generation Rate and Hydraulic Conductivity.....	47
3.5.3 Changes in Oxide Films on Iron Surface.....	48
3.6 Column E: TCE Co-existing with Cr(VI) in the Presence of CaCO ₃	54
3.6.1 Reaction Kinetics.....	54
3.6.2 Alkalinity Profiles, pH, Changes of Corrosion Potential, H ₂ Generation Rate and Hydraulic Conductivity	55
3.6.3 Changes in Oxide Films on Iron Surface.....	56
3.7 Discussion for the Five Columns	62
3.7.1 Presence of Cr(VI).....	62
3.7.2 Presence of CaCO ₃	63
Chapter 4 Numerical Simulation.....	66
4.1 The Numerical Model MIN3P.....	66
4.1.1 General Description.....	66
4.1.2 Modification of Kinetic Expressions in MIN3P.....	66
4.2 Simulation of the Column Experiments	67
4.2.1 Input Parameters.....	67
4.2.2 Chemical Reactions.....	68
4.3 Simulation Results.....	69
4.4 Evaluation of the Model Simulation.....	71

4.5 Application of the Model: the Long-Term Performance of an Iron PRB When TCE Co-exists with Cr(VI) in the Presence of CaCO ₃	74
Chapter 5 Conclusions.....	88
References	90

List of Tables

Table 2.1 Column properties and solution compositions	17
Table 2.2 Column operation history	18
Table 3.1 Corrosion potentials, pH and the initial TCE degradation half-lives for all five columns measured in Phases I and II	21
Table 3.2 Raman spectroscopic analysis of surface composition on iron grains taken from Column A	25
Table 3.3 Raman spectroscopic analysis of surface composition on iron grains taken from Column B	34
Table 3.4 Raman spectroscopic analysis of surface composition on iron grains taken from Column C	41
Table 3.5 Raman spectroscopic analysis of surface composition on iron grains taken from Column D	50
Table 3.6 Raman spectroscopic analysis of surface composition on iron grains taken from Column E	57
Table 3.7 Summary on the experimental results for the five columns in Phase III.....	65
Table 4.1 Input parameters used in the simulations.	76
Table 4.2 Complexation reactions and equilibrium constants.....	77
Table 4.3 Reaction stoichiometries of reduction-corrosion reactions.	78
Table 4.4 Mineral dissolution-precipitation reactions and equilibrium constants.....	78
Table 4.5 Fitting parameters for each column.....	79

List of Figures

Figure 2.1 Schematic of the column setup	19
Figure 3.1 Cr(VI) reduction profiles obtained from column A	26
Figure 3.2 Corrosion potential and pH changes in column A	27
Figure 3.3 The measured rates of H ₂ production rate in columns A, B, C, D and E in Phase III.....	28
Figure 3.4 The measured hydraulic conductivities in columns A, B, C, D and E in Phase III.	29
Figure 3.5 Spectra of iron surfaces at ports 5 cm from the influent end (a1 and a2) and 15 cm from the influent end (b) in column A.	30
Figure 3.6 Cr(VI) profiles obtained from column B	35
Figure 3.7 Alkalinity profiles obtained from column B	36
Figure 3.8 Corrosion potential and pH changes in Column B.....	37
Figure 3.9 Spectra of iron surfaces at bottom of the column (a) and at port 15 cm from the influent end (b) in column B.....	38
Figure 3.10 TCE profiles before and after CaCO ₃ addition for column C.	42
Figure 3.11 Alkalinity profiles in column C.....	43
Figure 3.12 Corrosion potential and pH changes in Column C.....	44
Figure 3.13 Spectrum of iron surfaces in column C.....	45
Figure 3.14 TCE and Cr(VI) profiles obtained from column D.....	51
Figure 3.15 Changes of corrosion potential and pH in column D.....	52
Figure 3.16 Spectra of iron surfaces at ports 5 cm from the influent end (a) and 15 cm (b) from the influent end in column D.....	53
Figure 3.17 TCE and Cr(VI) profiles obtained from column E	58
Figure 3.18 Alkalinity profiles from Column E.	59
Figure 3.19 Changes of corrosion potentials and pH in column E.....	60
Figure 3.20 Spectra of iron surfaces at the bottom port (a) and the port 15 cm (b) from the influent end in column E.....	61
Figure 4.1 Laboratory and simulation profiles for column A: (a) Cr(VI), (b) pH, (c) Fe(OH) ₃ (am) volume fraction, (d) Cr(OH) ₃ (am) volume fraction, (e) porosity, and (f) reactive surface area. .	80
Figure 4.2 Laboratory and simulation profiles for column B: (a) Cr(VI), (b) pH, (c) Alkalinity, (d) aragonite volume fraction, (e) Fe ₂ (OH) ₂ CO ₃ volume fraction.	81
Figure 4.3 Simulated profiles for column B: (a) Fe(OH) ₃ (am) volume fraction, (b) Cr(OH) ₃ (am) volume fraction, (c) porosity, and (d) reactive surface area.	82

Figure 4.4 Laboratory and simulated profiles for column C: (a) TCE, (b) pH, and (c) alkalinity, (d) aragonite volume fraction, (e) $\text{Fe}_2(\text{OH})_2\text{CO}_3$ volume fraction (f) porosity, and (g) reactive surface area.....	83
Figure 4.5 Laboratory and simulated profiles for column D: (a) Cr(VI), (b) TCE, and (c) pH, (d) $\text{Fe}(\text{OH})_3(\text{am})$ volume fraction (e) $\text{Cr}(\text{OH})_3(\text{am})$ volume fraction, (f) porosity, and (g) reactive surface area.....	84
Figure 4.6 Laboratory and simulated profiles for column E: (a) Cr(VI), (b) TCE, (c) pH, and (d) alkalinity.....	85
Figure 4.7 Simulation profiles for column E: (a) $\text{Fe}(\text{OH})_3(\text{am})$ volume fraction (b) $\text{Cr}(\text{OH})_3(\text{am})$ volume fraction, (c) aragonite volume fraction, (d) $\text{Fe}_2(\text{OH})_2\text{CO}_3$ volume fraction, (e) porosity, and (f) reactive surface area.	86
Figure 4.8 A hypothetical scenario simulating long-term performance of an iron PRB of 40 cm thick to treat groundwater containing 10 mg/L Cr(VI), 5 mg/L TCE and 300 mg/L CaCO_3 over 30 years: (a) Cr(VI) profiles, (b) TCE profiles, (c) total carbonate volume fraction, and (d) porosity	87

Chapter 1 Introduction

Permeable reactive barriers (PRBs) containing granular iron have rapidly gained acceptance as an innovative and cost-effective groundwater cleanup technology and have been applied extensively for the in-situ remediation of groundwater plumes containing chlorinated organics as well as other inorganic containments (Gillham, 1999; Blowes et al., 2000; Yabusaki et al., 2001). Compared to the traditional “pump and treat” technology, the installation cost of an iron PRB is somewhat higher, while the operation and maintenance costs are very low. Therefore, the major advantage of this technology depends on its longevity. The effective working lifetime of a PRB is mainly controlled by two factors, the reactivity of the granular iron in the subsurface and the effective permeability.

Loss of iron reactivity has been associated with co-existing oxidants and precipitation of secondary minerals as a consequence of the local groundwater geochemical conditions (Farrell et al., 2000; Schlicker et al., 2000; Alowitz and Scherer, 2002; Ritter et al., 2003; Zhang and Gillham, 2003; Jeen et al., 2006; Lu, 2005; Okwi et al., 2005). Cr(VI) and nitrate are frequently detected as competing oxidants associated with chlorinated solvent plumes (Schlicker et al., 2000; Ritter et al., 2003; Blowes et al., 2000). For example, a large plume containing TCE and Cr(VI) was studied near Elizabeth City, North Carolina in 1991 (Blowes et al., 1999a, 1999b; Mayer et al., 2001).

In order to evaluate the long-term performance of iron PRBs, it is important to understand, quantify and predict iron reactivity and passivation. However, the remediation processes within a PRB are very dynamic and complex, where the various chemical reactions and transport processes occur simultaneously. Thus, studies incorporating reactive transport and geochemical reactions are necessary (Mayer et al., 2001; Yabusaki et al., 2001; Liang et al., 2003; Jeen et al., 2006).

The purpose of this research was to determine the effects of co-existing oxidants on the iron reactivity towards chlorinated solvents and the reduction of the oxidants themselves in the presence of dissolved calcium carbonate, using chromate as a representative oxidant, and to evaluate the applicability of a reactive transport model for simulating the performance of PRBs in such environments.

1.1 TCE and Cr(VI) as Groundwater Contaminants

TCE, a chlorinated aliphatic organic compound, has been widely used as an industrial solvent and dry cleaning fluid (Gotpagar et al., 1997). Because of its physical and chemical properties such as low sorption, high solubility relative to the maximum contaminant level (MCL), and low degradation

rate, TCE is highly mobile and persistent in the subsurface and forms large-scale plumes (Pankow and Cherry, 1996). Because of the rapid growth in industrial use since the Second World War, chlorinated solvents are the most common industrial contaminants found in groundwater (Mackay et al., 1986; Gillham and O'Hannesin, 1994; Orth and Gillham, 1996). TCE is toxic, may cause liver problems and is potentially carcinogenic. In the United States, the maximum contaminant level (MCL) for TCE has been set at 5 µg /L (U.S. EPA, 2006).

Since natural degradation in groundwater is generally slow for many chlorinated organic compounds, as compared to the abiotic reduction by granular iron (Gillham and O'Hannesin, 1994), the technology of using granular iron has gained considerable attention as an effective remediation method for many groundwater contamination problems (O'Hannesin and Gillham, 1998; Blowes et al., 1999a, 1999b; Blowes et al. 2000; EnviroMetal Technologies Inc., 2006).

Chromium is a common groundwater contaminant due to the discharge of effluents from electroplating, leather tanning, chemical manufacturing and cooling systems (Blowes et al., 1997; Pratt et al., 1997; Blowes et al., 2000; Blowes, 2002; Erdem et al., 2004) and is listed as one of the priority pollutants by the U.S. EPA, with an MCL of 10 µg /L (U.S. EPA, 2006).

Chromium is usually encountered in the environment in the oxidation states of Cr(III) and Cr(VI). The oxidized hexavalent state of Cr forms chromate (CrO_4^{2-}), bichromate (HCrO_4^-), or dichromate ($\text{Cr}_2\text{O}_7^{2-}$). Cr(VI) is toxic and carcinogenic and Cr(VI) containing minerals are very soluble. Due to the negative charge of the Cr(VI) ion, Cr(VI) adsorption on aquifer minerals is limited and therefore, Cr(VI) may be present at concentrations well above water quality guidelines and may move with the flowing groundwater in aquifers (Blowes, 2002). In contrast, the reduced state, Cr(III), forms insoluble precipitates under slightly acidic or neutral conditions (Blowes, 2002). Because of the different characteristics and toxicity between Cr(VI) and Cr(III), removal of Cr(VI) is generally through the reduction of Cr(VI) to Cr(III) to limit both the concentration and mobility.

1.2 Degradation of TCE and Cr(VI) by Granular Iron

1.2.1 Effects of Co-existing Oxidants on TCE Reduction

Because water and chlorinated aliphatic compounds generally have higher reduction potential than Fe^0 , Fe^0 will be oxidized in solution containing dissolved chlorinated solvents (Matheson and Tratnyek, 1994; O'Hannesin and Gillham, 1994). The study of Gillham and O'Hannesin (1994)

showed that reactions of chlorinated aliphatic compounds with iron in aqueous solution are many orders of magnitude faster than natural abiotic rates reported in the literature, and that the reactions proceed with oxidation-reduction processes.

Two parallel reactions occur in the iron –TCE solution systems:



and



The first reaction shows the corrosion of iron by water and the second reaction is similar to (1.1) in that it also shows corrosion of the iron, but in this case the organic compound (RX) serves as the oxidant, resulting in non-chlorinated hydrocarbon (RH) as the reaction product. The mechanisms proposed for TCE degradation are catalytic hydrogenation (Li and Farrell, 2002) and direct electron transfer (Arnold and Roberts, 2000).

Reactions (1.1) and (1.2) show the net effects of iron corrosion by water and chlorinated solvents, indicating the production of H₂ and RH; the release of Fe²⁺ to solution and an increase in pH. The reactions also imply a decrease in Eh to strongly reducing conditions.

The rise in pH leads to the precipitation of ferrous hydroxide:



In the absence of O₂, Fe(OH)₂ is metastable and transforms to Fe₃O₄ (magnetite) according to the following reaction, known as the Schikorr reaction (Odziemkowski et al., 1998):



Under neutral pH conditions, as an intermediate between Fe(OH)₂ and magnetite, mixed-valent Fe(II)/Fe(III) salts, known as green rusts may also form (Bonin et al., 2000).

The commercial grade granular iron used for in-situ construction of PRBs is generally produced from waste iron materials. As a consequence of having been passed through a rotary kiln, these materials are covered with a double layer of oxides: the inner layer consisting of magnetite (Fe_3O_4) and the outer layer consisting of higher valence iron oxides: namely hematite ($\alpha\text{-Fe}_2\text{O}_3$) and maghemite ($\gamma\text{-Fe}_2\text{O}_3$) (Ritter et al., 2003).

The electrical conductivity of the surface films can have a detrimental effect on maintaining the reactivity of granular iron materials (Schlicker et al., 2000). The difference between mixed valent Fe(II)/Fe(III) oxides, such as magnetite and green rust, and tri-valent iron oxides, such as hematite and maghemite, is that mixed valent oxides are electron conducting, while high valent oxides are passive films that are not conducting. The study by Ritter et al. (2002) showed that when placed in water, the outer passive oxide layer of the commercial iron is removed, or converted to a conducting magnetite film by autoreduction processes.

Previous studies on the effects of co-existing oxidants on TCE reduction have mainly focused on nitrate (Farrell et al., 2000; Schlicker et al., 2000; Ritter et al., 2003; Lu, 2005). A long-term column study showed that the TCE effective half-life in the column receiving 5 mM $\text{Ca}(\text{NO}_3)_2$ increased from approximately 25hr after 10 days to approximately 58.3hr after 667 days (Farrell et al., 2000). The study of Schlicker et al. (2000) indicated that in the presence of nitrate or Cr(VI), TCE dechlorination was significantly slowed as a consequence of nitrate or Cr(VI) degradation by iron. The decline in iron reactivity towards TCE reduction was proposed to be caused either by competition for a limited number of electrons between the oxidant (nitrate or Cr(VI)) and TCE, or by the formation of passive oxide films on the iron surface caused by the presence of the oxidant. However, measurements of potential changes and microscopic identification of the iron surface before and after column operation were not conducted in these studies.

Using a typical commercial grade iron, Connelly iron, Ritter et al. (2003) conducted a column experiment to study the effect of nitrate on TCE degradation. Results showed that the reduction of TCE at a concentration of 1.5 mg/L was inhibited in the presence of 100 mg/L of nitrate. Raman spectroscopy measurements indicated that nitrate interfered with the initial removal of the outer oxide layer on the iron. The pH and potential in the presence of nitrate caused the pre-existing passive layer of $\gamma\text{-Fe}_2\text{O}_3$ (maghemite) and $\alpha\text{-FeOOH}$ (goethite) to remain on the iron surface, and therefore, the reduction of TCE was largely inhibited.

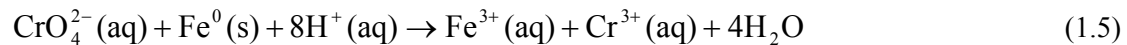
The iron used in the study of Ritter et al. (2003) was not pre-autoreduced by contact with water, so it is not clear whether the reduced TCE degradation rate was caused by the formation of

trivalent iron oxide or by the pre-existing oxides. In addition, the significantly higher concentration of nitrate than TCE (the molar ratio of nitrate to TCE was 9:1) could result in a competitive advantage for nitrate, reducing the TCE degradation rate. Therefore, Lu (2005) used pre-autoreduced Connolly iron and multi concentration ratios of nitrate and TCE (molar ratios from 1:1 to 20:1) to examine the causes of declining TCE degradation rate in the presence of nitrate. It was found that given the same TCE concentration, higher nitrate concentration leads to a more positive shift in the corrosion potential. Raman microscopy measurements showed an increased amount of the high valency iron oxides as nitrate concentration increased. At the same time, both TCE and nitrate degradation rates decreased. It was concluded that the oxidizing effect of nitrate controlled the corrosion environment, and the change in corrosion potential led to thermodynamic conditions favorable for the formation and stability of higher valency iron oxides (Fe_2O_3 , $\text{Fe}(\text{OH})_3$ and $\alpha\text{-FeOOH}$) at the iron surface. These passive oxides act as a physical barrier and greatly interfere with charge transfer processes, and thus both TCE and nitrate degradation rates declined. Lu (2005) also found that the change in the iron surface condition and the loss of iron reactivity due to nitrate is a reversible process.

1.2.2 Reduction of Cr(VI) by Granular Iron

Treatment of Cr(VI) can be performed by iron-bearing reductants (Blowes et al., 1997; Erdem et al., 2004). Using four types of iron-bearing solids (i.e., iron filings, iron chips, pyrite, and siderite), Blowes et al. (1997) found fine grained iron filings to be the most effective material to reduce Cr(VI), and the reduction rate was sufficiently rapid for use in groundwater remediation systems.

The removal mechanism for Cr(VI) by Fe^0 is through the reduction of Cr(VI) to Cr(III), coupled with the oxidation of Fe^0 to Fe(III), and the subsequent precipitation of sparingly soluble $\text{Cr}(\text{OH})_3$, mixed Fe(III)-Cr(III)hydroxide or mixed Fe(III)-Cr(III) (oxy)hydroxide phases occurring through the reactions below (Powell, et al., 1995; Blowes et al., 1997; Pratt et al., 1997; Blowes et al., 2000; Astrup et al., 2000):

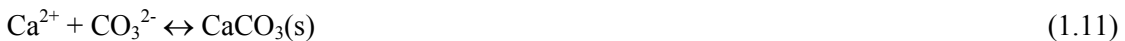


The precipitated species have been confirmed by solid-phase analytical techniques such as XPS and Raman spectroscopy (Powell, et al., 1995; Blowes et al., 1997; Pratt et al., 1997; Blowes et al., 2000; Astrup et al., 2000), and the study of Astrup et al. (2000) indicated that the reactions were not reversible.

Though Cr(VI) is one of the most common inorganic groundwater contaminants at hazardous waste sites, research has been largely limited to the treatment of Cr(VI) itself, with little attention to the effects of Cr(VI) as a co-existing oxidant on TCE reduction by granular iron. However, as a co-existing contaminant, a significant difference between the effects of Cr(VI) and nitrate should be expected, because nitrate may cause precipitates of iron to form without precipitates of nitrate itself. Whereas, in the case of Cr(VI), not only the precipitates of iron will form, but the precipitates of chromium will also form.

1.2.3 Secondary Mineral Precipitation

The formation of secondary minerals within an iron barrier is undesirable; however, both laboratory tests and field studies have shown evidence of mineral precipitation (Gillham, 1999; Blowes et al., 2000; Mayer et al., 2001; Jeen et al., 2006). Most groundwater contains carbonate in various concentrations. An increase in pH as the net effect of iron corrosion will cause a shift in the carbonate-bicarbonate equilibrium, and thus result in the formation of carbonate mineral precipitates (Mackenzie et al., 1999):



There are many factors such as pH, ion type and concentration, iron corrosion rate, and residence time in the system, that can influence the type and extent of precipitation. Depending on local geochemical conditions, carbonate-containing minerals, such as iron hydroxy carbonate ($\text{Fe}_2(\text{OH})_2\text{CO}_3$) (Jeen, 2005) and carbonate green rust ($[\text{Fe}_4\text{Fe}_2(\text{OH})_{12}][\text{CO}_3 \cdot 2\text{H}_2\text{O}]$) can also form (Bonin et al., 2000).

The accumulation of precipitates can have a significant influence on the long-term performance of granular iron PRBs. The accumulation of precipitates can either form a film, coating the granular iron grains or as unattached fine precipitates, thus decreasing porosity and hydraulic

conductivity and in turn restricting groundwater flow. The precipitate coatings on the granular iron surface can also act as physical barriers, blocking access of contaminants to the iron surface, and thus decrease the reactivity of the iron (Zhang and Gillham, 2005). The reasons for decreasing iron reactivity could be due to a reduced number of reactive sites or reduced reactive surface area, or declining rate of electron transfer across progressively thicker precipitate layers, or a combination of the two. Even though the exact mechanism has not been determined, the loss of iron reactivity is a significant concern regarding long-term performance of iron PRBs. Therefore, a quantitative model capable of predicting the relationship between the precipitates with the change of iron reactivity and effectiveness of PRBs is very important for the evaluation of the long-term performance of iron PRBs (O'Hannesin and Gillham, 1998; Gillham, 1999; Mayer et al., 2001; Liang et al., 2003; Jeen, 2005).

1.2.4 Modeling Studies

Within reactive barriers, both geochemical reactions and transport occur interactively and simultaneously. However, earlier modeling studies have focused primarily on chemical equilibrium, and transport modeling coupled with geochemical reactions did not proceed until recently (Mayer et al., 2001; Yabusaki et al., 2001; Liang et al., 2003; Jeen et al., 2006). Of the recent studies, Jeen et al. (2006) introduced the reactivity loss of iron and the accumulation of secondary minerals into an existing multi-component reactive transport model MIN3P by Mayer (1999). The model MIN3P is a general-purpose reactive transport model that simulates the interactions of mass transport and geochemical reactions in variably-saturated media (Mayer, 1999).

Based on column experiments using TCE or Cr(VI) as target contaminants and various concentrations of calcium carbonate, the effects of secondary minerals on the permeability and reactivity of iron were evaluated and a conceptual model was established (Jeen, 2005). The precipitates formed initially at the influent ends of the column, reducing the reactivity of the iron in this region. As a consequence of the reduced reactivity, mineral formation migrated further into the column to precipitate in a region where the reactivity remained high. Thus precipitation occurred as a moving front through the column. This process continued until a certain level of mineral accumulation was reached and mineral precipitation spread progressively further into the column.

By representing the declining reactivity as a decrease in reactive surface area, the reactivity change was incorporated into kinetic expressions of an existing multi-component reactive transport model (MIN3P). The simulation results reproduced the observations from the column experiments successfully, supporting the predictive capability of the model. However, the range of application of

the model needs to be tested. In this study, predicting iron passivation by different types of secondary minerals in the presence of a competing oxidant, such as chromate, was conducted. For the purpose of this study, the term iron passivation includes passivation caused by non-conducting passive oxide films, as well as the precipitation of secondary minerals on the iron surface.

1.3 Research Objectives

The primary objective of this study was to determine the effect of Cr(VI) and dissolved calcium carbonate on changes of the iron reactivity towards TCE and Cr(VI) reduction and to provide mechanistic explanations for the observed effects.

The second objective was to evaluate whether the model developed by Jeen (2005) can be extended to the more complicated system in which Cr(VI) and CaCO₃ co-exist with TCE.

The objectives were pursued by conducting column experiments using pre-treated iron material. The potential shifts and the surface films were examined by continuous corrosion potential measurement and measurement of composition of the surface films. Different combinations of TCE, chromate and dissolved calcium carbonate were used to examine the effects of chromate and dissolved calcium carbonate on TCE and chromate degradation kinetics. The experimental results were used to verify the applicability of the model developed by Jeen (2005).

Chapter 2 Methods

2.1 Column Experiments

In order to assess the effect of Cr(VI) and dissolved calcium carbonate on changes of the iron reactivity towards TCE and Cr(VI) reduction, five columns were assembled to simulate groundwater flow through iron PRBs. In addition to studying the contaminant reduction kinetics through analysis of organic and inorganic constituents, pH, in-situ open circuit potential and ex-situ Raman surface analyses were conducted. Columns were operated for about 8 months and all experiments were conducted in the same laboratory at ambient temperature ($24 \pm 2^\circ\text{C}$).

2.1.1 Column Design and Packing

Fig. 2.1 shows a typical column assembly used in this study. Five PlexiglasTM columns with an internal diameter of 3.81 cm and a length of 20 cm were used. There were 5 sampling ports located at 2.5, 5, 10, 15 and 17.5 cm from the influent end. A nylon Swagelok[®] fitting (0.16 cm O.D. tube \times 0.16 cm NPT male connector) was tapped into each sampling port on the column wall and a stainless steel syringe needle (16 D11/2) was held by each fitting. The needle was packed with glass wool to prevent clogging by fine particles. All tips of the five needles were aligned along the central axis of the column. Two additional ports, containing Swagelok[®] reducing fittings, were located on the wall of each column at a 90° angle to the row of sampling ports: Port I, 3 cm from the inlet (near the influent end) and Port E, 17 cm from the inlet (near the effluent end). These ports were used to hold the reference electrodes for in-situ measurements of corrosion potential. A pure iron rod (7 cm long and 2 mm O.D.) was fitted to a Swagelok[®] reducing unit to serve as the electrical connector on the opposite side from the reference electrode of Port I.

All columns were packed dry with as-received commercial-grade granular iron obtained from Connelly-GPM, Inc. (Chicago, Illinois). The surface area of the iron, determined by the BET method (Brunauer et al., 1938), was $1.23 \text{ m}^2/\text{g}$. In order to obtain a homogeneous packing of the iron, about a 2 cm lift of iron was added each time and each lift was tamped with an acrylic rod gently, and the surface was roughened before adding the next lift. To hold back fine iron particles and to promote an even distribution of water over the cross-sectional area of the column, 100 and 10 mesh Nytex[®] screens were placed at each end of the column. After packing with iron, the columns were purged with CO_2 gas for about 2 hours to remove oxygen from the pore space followed by deoxygenated

Millipore water. The initial porosity was determined by knowing the volume of each column and the total mass of iron added, and measuring the column weight after saturation of the column with water (assuming a density of water of 1.0 g/cm³). The column dimensions, iron surface, pore volume (PV), porosity, iron dry bulk density and source solutions for each column are listed in Table 2.1.

2.1.2 Solution Preparation and Column Operation

The experiments were divided into three phases (Table 2.2). In phase I, Millipore water was introduced into all five columns for approximately 45 days (~ 60 pore volumes) to achieve auto-reduction of the pre-existing passive films on the iron surface. The corrosion potentials in the columns were monitored continuously. Once the corrosion potential reached a quasi-steady state, the influent was switched to a 10 mg/L TCE solution (Phase II). After about 50 pore volumes of 10 mg/L TCE was pumped through each of the five columns, the initial TCE degradation rate and iron reactivity, which were used as references to compare the changes of TCE degradation rate and passivation of the iron, were determined. In phase III, different combinations of TCE, chromate and CaCO₃ were put in the five columns to determine the influences of chromate and CaCO₃ on iron reactivity towards TCE reduction.

Each column received a different solution, as shown in Table 2.1. To prepare the feed solutions containing no dissolved CaCO₃ (Columns A and C), oxygen-free N₂ gas was used to purge a 22 L glass carboy containing 18 L of Millipore water for about 2 hours. As a result, the dissolved O₂ concentrations were reduced to below 0.2 mg/L as measured by a ChEMets Kit, K-7501 (applicable between 0-1 mg/L). Then, a concentrated stock solution of TCE (371,285 mg/L in methanol) and/or 10,000 mg/L Cr(VI) stock solution (prepared by dissolving K₂Cr₂O₇ (s) in Millipore water) were spiked to the deoxygenated feed solutions to achieve nominal concentrations of 5 mg/L of TCE and 10 mg/L of Cr. The CaCO₃ solutions (columns B, D and E) were prepared by first adding a pre-calculated amount of CaCO₃ powder to the Millipore water in the carboy, purging with CO₂ gas to dissolve the solid CaCO₃, and then purging with oxygen-free N₂ gas to remove oxygen and to adjust the pH value to 6.5±0.2. Finally, the desired feed solution was made by spiking concentrated Cr(VI) and/or TCE stock solutions. On average, the feed solutions were replenished every month.

In order to avoid oxygen contamination, stainless steel tubing was used between the bottle of feed solution and the column, with the exception of short lengths (15 cm) of Ismatec 2-stop Viton® tubing (Cole-Parmer) that passed through the pump. An aluminum foil balloon filled with oxygen-free N₂ gas was used for a further prevention against oxygen intrusion. For source solutions without

TCE (Column A and B), the balloon was connected to the source bottle directly to maintain the N₂ gas head space of the source bottle. For source solutions containing TCE (Column C, D and E), the balloon was connected to a “guard bottle” containing deoxygenated Millipore water and 5 mg/L TCE. The N₂ gas leaving the balloon equilibrated with the solution in the “guard bottle” prior to entering the headspace in the feed bottle (Fig. 2.1), thus helping to maintain the TCE concentration in the feed bottle.

The solutions were pumped into the columns from the bottom using an Ismatec multi-channel peristaltic pump (Model 78001-12). The resident times of the five columns ranged between 5 and 6 hr, as a consequence of differences in porosity (Table 2.1). The effluent volume was recorded periodically, and the mass of water collected in a given period of time was used to calculate the average flow rate during that period. Generally, the flow rate from the effluent end was in the range of 0.10 ~ 0.12 mL/min in Phases I and II, and 0.35 ~ 0.38 mL/min in Phase III. The volume from the effluent end was used to keep track of the cumulative pore volumes passed through the column.

Teflon® tubing connected to “T” valves near the inlet and outlet of the column were used as manometers (Fig. 2.1) to periodically monitor the hydraulic head difference across the column, which was in turn used to calculate the hydraulic conductivity according to the Darcy equation. The gases evolved from the effluent were trapped using a sealed glass tube before entering the waste bottle (Fig. 2.1). The volume difference in the sealed glass tube over a given time interval was then used to calculate the gas production rate. The gas production rates collected in the early stage of phase III were used to calculate the initial iron corrosion rate as required by the mathematical model (see Chapter IV for details).

2.2 Chemical Analyses

Samples were periodically collected from all sampling ports, including the influent and the effluent ends, using a glass syringe. Sampling started from the effluent end and proceeded to the influent end. Different sizes of glass syringe (5, 10, or 20 mL) were used based on the required sample volumes. Prior to sample collection, several drops were discarded to remove stagnant water from the port. Between samples, the syringe was rinsed three times with methanol and Millipore water, respectively.

2.2.1 Organic Analyses

TCE

In order to analyze TCE, 2 mL of sample was added to 2 mL of pentane containing 500 µg/L of 1,2-dibromoethane as an internal standard in a 5 mL glass screw cap vial with TeflonTM-faced septum. The internal standard was used to verify consistent injection volumes on the gas chromatograph (GC). The sample vial was then placed on a rotary shaker for 15 minutes at 300 rpm, to allow equilibration between the water and the pentane phases. The pentane phase was then removed and transferred to a 2 mL glass crimp-top GC vial, and then put on a Hewlett Packard 5890 Series II GC equipped with a ⁶³Ni electron capture detector (ECD). Using a HP 7673 liquid auto-sampler, a 1 µL sample was injected onto a DB-624 capillary column. The detector temperature was 300°C, injector temperature was 200°C, and the column temperature ramp was 50°C to 150°C at a rate of 15°C/min and then held for 1 minute. The carrier gas was pre-purified helium with a total flow rate of 25 mL/min and the make-up gas was 5% methane/95% argon. The calibration range was from 10 to 3500 µg/L. Samples with concentrations above the calibration range were diluted by using a smaller volume of aqueous sample. The method detection limit (MDL) was 1.0 µg/L.

Chlorinated Degradation Products

Analyses for the intermediate degradation products (DCE isomers and VC) were performed using a headspace analysis method. A 4 mL aqueous sample was transferred to a 10 mL glass vial sealed with a TeflonTM-faced butyl-rubber septum and an aluminum cap. The sample vial was placed on a rotary shaker for 15 minutes to allow equilibration between the aqueous phase and gas phase. For analysis, the sample vial was placed on a Hewlett Packard 7694 headspace sampler. A 1 mL sample was injected onto a Hewlett Packard 5890 Series II GC equipped with a Hnu photo ionization detector (PID). The GC was fitted with a Hnu NSW-PLOT capillary column (15m × 0.53mm I.D.), and the lamp potential was 10.2eV. The GC oven had an initial temperature of 50°C, with a temperature program of 20°C/min reaching a final temperature of 200°C and held for 6 minutes. The detector temperature was 150°C and injector temperature was 100°C. The carrier gas was ultra pure helium with a flow rate of 20 mL/min. The MDLs were 2.4 µg/L for trans-DCE, 1.3 µg/L for cis-DCE, and 1.3 µg/L for VC.

Hydrocarbon gases

For hydrocarbon gases, analyses were conducted using a HP 5790 A GC equipped with a flame ionization detector (FID) and a Megabore GS-Q capillary column. A 2.5 mL sample was placed in a 5 mL glass screw-cap vial, sealed with a TeflonTM-faced septum, thus creating a solution to

headspace ratio of 1:1. Samples were placed on a rotary shaker at 300 rpm for 15 min to allow equilibration between the aqueous phase and gas phase. A liquid of 250 μL sample was injected. The GC oven had an initial temperature of 60°C, which was held for 3 minutes; the temperature was then increased at a rate of 15°C/min, reaching a final temperature of 120°C and held for 10 minutes. The detector temperature was 280°C and the injector temperature was 120 °C. The carrier gas was ultra pure nitrogen with a flow rate of 20 mL/min. The gases analyzed included ethene and ethane. For acetylene analysis, an isothermal method was used. The GC oven temperature was 40°C. The detector and the injector temperature were both set at 200°C. The MDLs were 0.5 $\mu\text{g/L}$ for ethene, 0.4 $\mu\text{g/L}$ for ethane, and 3 $\mu\text{g/L}$ for acetylene.

2.2.2 Inorganic Analyses

pH

The pH of the same sample was measured using a combination glass-Ag/AgCl reference electrode and a Markson™ Model 90 digital pH/mV/Temperature meter. Prior to each set of measurements, the electrode response was calibrated using pH buffers. A two-point linear calibration was conducted using a pH 7.0 buffer and either a pH 4.0 or a pH 10.0 buffer, depending on the expected range of sample pH values. Between samples, the electrode was rinsed thoroughly with de-ionized water and wiped to remove excess water from the glass bulb.

Alkalinity

Alkalinity was determined using a standard laboratory analysis method (Standard Methods, 1985). A 2 mL sample was transferred to a 5 mL beaker, and 2 to 3 drops of bromocresal green indicator was added. The sample was then titrated with standardized sulphuric acid approximately 0.0016 N to the pH=4.5 endpoint when a greenish yellow color was reached. A magnetic stir bar was stirring inside the beaker while titrating. The amount of acid added to the solution was then back calculated to total alkalinity and expressed in terms of mg/L CaCO_3 .

Cr (VI)

The concentration of hexavalent chromium was determined using a colorimetric method (Standard Methods, 1985). 1,5-diphenylcarbohydrazide was used as a coloring reagent and a Beckman DU 530 UV/VIS spectrophotometer was used to measure the color intensity at a

wavelength of 540 nm. The calibration range was from 0.05 to 1.5 mg/L. The MDL was 0.05 mg/L. Samples with concentrations above the calibration range were diluted with Millipore water.

2.3 In-situ Corrosion Potential Measurements

Corrosion potential (also referred to as open-circuit potential, OCP) is the potential naturally adopted by an isolated metal when the total rate of oxidation exactly equals the total rate of reduction. It represents a property of a metal rather than an aqueous phase (Odizemskowski et al., 1998).

Similar to the method described in Odizemskowski et al. (1998), in-situ potential measurements were conducted continuously during column operation. The potential measurements were implemented through two reference electrodes and a working electrode combined with the electrical connector (a pure iron rod) (Fig. 2.1). Outside the column the reference electrodes and the electrical connector were connected through a high input impedance (10^{14} ohms) preamplifier to prevent current flowing between the electrodes. The impedance unit was connected to a UPC601-U Universal PC Sensor Interface Card, which transmitted data to a computer. Each reference electrode consisted of a glass compartment in which a $\text{Ag}/\text{AgCl}/\text{Cl}^-_{\text{sat}}$ reference electrode was attached to the column by a #7 Teflon® screw and O-ring, and the tip of the compartment contacted with iron particles in the column. One end of the iron electrical connector was in the center of the column and was in contact with the iron particles in the column. The iron particles actually functioned as the working electrode. The measured potential values thus represented average values for the iron particles in the immediate vicinity of the tip of the reference electrode compartment. The measured potential was converted to the standard hydrogen reference electrode (SHE) value. The drift of each reference electrode was estimated and the data was corrected accordingly over the operation period. Normally the drift range was about 0.2~ 0.3 mV per day.

2.4 Raman Spectroscopic Measurements

2.4.1 Ex-situ Raman Analysis

At the end of the column operation, each column was disconnected and transferred to a glovebox containing 100% nitrogen atmosphere. The nylon Swagelok® fitting or the cap was removed to allow access to the iron inside of the column. For each column, in order to study the formation of the oxide films and/or secondary mineral precipitates, samples were taken from both the upper and lower part of the column based on the Cr(VI) or alkalinity profiles. Iron samples were

taken from Port E for all five columns, from the influent end for columns B, C and E, and from Port I for columns A and D. The iron grains were immediately transferred to a specially constructed Raman cell which contained a 5.4 mL glass hypovial that was partially filled with the solutions coming from the same port as the iron particles, and then a Teflon®-faced butyl rubber septum and a cap were added and tightened, displacing excess solution.

The sealed cell was taken for Raman Spectroscopy analysis. Raman spectra were obtained with a Renishaw 1000 Raman microscope system. A 41 mW laser beam was used, which resulted in approximately 9 mW at the observation stage and even less on the sample surface. Such low intensity is unlikely to alter the surface film. The microscope objective lens had a magnification of 50. The resulting laser focus had a diameter of ca. 5 μm on a rough surface and a depth of field of 3 μm .

Generally, two areas were picked randomly for each sample under the microscope, and 5 spots within the range of 55 μm for each area was analyzed. Thus, normally 10 spots were studied for each sample.

2.4.2 Identification of Oxide Species and Secondary Minerals on Iron Surface

Raman identifications in this study were based on available literature data. Hematite ($\alpha\text{-Fe}_2\text{O}_3$) was identified by a group of bands with peaks located at ca. 225, 245, 295, 415, 500, 615, and 1320 cm^{-1} (Oblonsky and Devine, 1995, and refs. therein), in which the peak at 225 cm^{-1} corresponds to high intensity A_{1g} mode, and the peaks at 295 cm^{-1} and 415 cm^{-1} correspond to E_g mode. Some of these bands overlap with the bands of other species, but the band at 225 cm^{-1} is unique to hematite and thus was used for identification in this study.

The Raman band around 665 cm^{-1} to 670 cm^{-1} was attributed to the high intensity of A_{1g} mode of magnetite (Fe_3O_4) with other weak bands at ca. 298 cm^{-1} , 320 cm^{-1} , 420 cm^{-1} and 550 cm^{-1} (Gui and Devine, 1991; Oblonsky and Devine, 1995, and refs. therein).

Goethite ($\alpha\text{-FeOOH}$) is identified by a group of bands with peaks located at ca. 245, 299, 390, 420, 470, and 560 cm^{-1} (Oblonsky and Devine, 1995, and refs. therein), in which the peaks at 299 cm^{-1} , 390 cm^{-1} , 470 cm^{-1} and 560 cm^{-1} corresponded to high intensity mode.

According to Bonin et al. (2000), the bands at ca. 433 cm^{-1} and 509 cm^{-1} were assigned to $\text{Fe}^{2+}\text{-OH}$ and $\text{Fe}^{3+}\text{-OH}$ stretching modes of green rust. Chromate (CrO_4^{2-}) was identified by a group of bands with peaks located at ca. 348, 363, 848 and 884 cm^{-1} (Frost et al. 2005, and refs. therein).

Chromite ($\text{Fe}_n\text{Cr}_m\text{O}_4$) is an oxide mineral with a spinel structure containing of divalent iron and trivalent iron and chromium. Chromite is identified at the peaks of 550, 620, 670~686 cm^{-1} and 700 cm^{-1} (Boucherit et al., 1992; Thieme and Scharnweber, 1993, and refs. therein).

The Raman spectrum of Cr_2O_3 was characterized as a group of peaks at 303 cm^{-1} and 551 cm^{-1} of strong A_{1g} mode, and 351, 397, 530 and 609 cm^{-1} of weaker E_g mode (Oblonsky and Devine, 1995, and refs. therein). α - CrOOH was attributed in the ca. 535-665 cm^{-1} range (Maslar et al., 2001).

According to Herman et al. (1987), the Raman spectra of calcite might be identified at 1087 cm^{-1} as the strongest $A_{1g, \text{int}}$ mode (V_1 , symmetric stretch), and bands at 154, 283, 714, 1430 and 1750 cm^{-1} were also attributed to calcite. The observed Raman shifts in line positions for aragonite and ankerite were 150, 205, 704, 1085 cm^{-1} and 285, 723, 1091, 1435, 1745 cm^{-1} , respectively.

Normally, due to instrument resolution and the change of material property (e.g. stress and purity), there was a slight shift of the band position (2 ~ 5 cm^{-1}) among the results of literature (Odziemkowski et al., 1998; Odziemkowski and Simpraga, 2004).

Table 2.1 Column properties and solution compositions

Column	A	B	C	D	E
Source composition	10 mg/L Cr	10 mg/L Cr + 300 mg/L CaCO ₃	5 mg/L TCE + 300 mg/L CaCO ₃	5 mg/L TCE + 10 mg/L Cr	5 mg/L TCE + 10 mg/L Cr + 300 mg/L CaCO ₃
Surface area (m ² /g)	1.23				
Column length (cm)	20				
I. D. (cm)	3.81				
Sampling port (cm)	0, 2.5, 5, 10, 15, 17.5, 20 cm from the influent end				
Mass of iron (g)	689.1	718	685.7	675.7	694.2
PV (cm ³)	141	116.7	136	129.5	138.7
Porosity	0.62	0.51	0.60	0.57	0.61
Bulk density (g/cm ³)	3.02	3.15	3.01	2.96	3.04

Table 2.2 Column operation history

<p>Phase I Auto-reduction of pre-existing passive films</p>	<p>Input Millipore water for about 60 pore volumes to all five columns</p>
<p>Phase II Initial iron reactivity measurement</p>	<p>Input TCE (10 mg/L) for about 50 pore volumes to all five columns</p>
<p>Phase III Influence of TCE, Cr(VI) and CaCO₃ on iron reactivity by adding different combinations of 5 mg/L TCE, 10 mg/L Cr, and 300 mg/L CaCO₃</p>	<p>A Cr(VI)</p>
	<p>B Cr(VI) + CaCO₃</p>
	<p>C TCE + CaCO₃</p>
	<p>D TCE + Cr(VI)</p>
	<p>E TCE + Cr(VI) + CaCO₃</p>

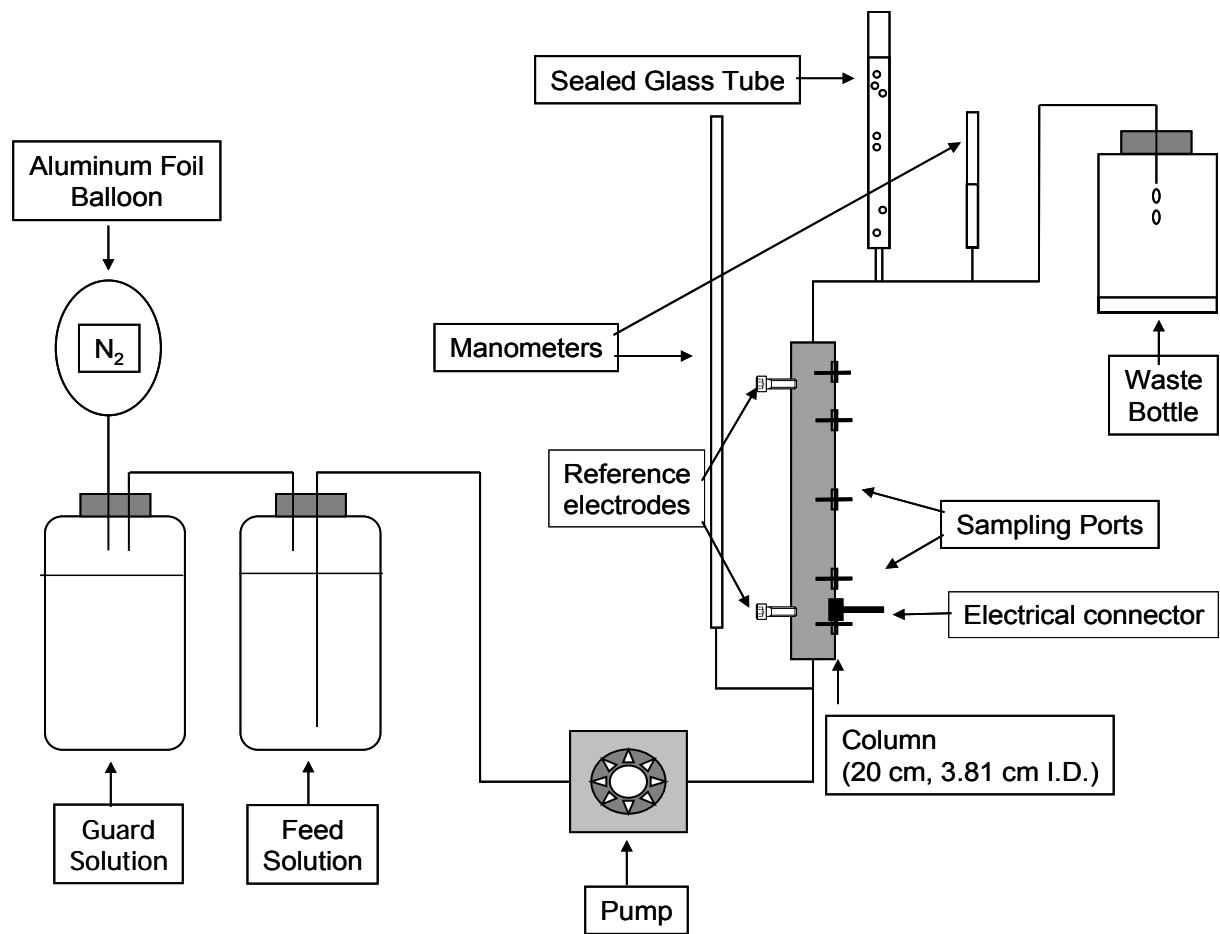


Figure 2.1 Schematic of the column setup

Chapter 3 Experimental Results and Discussion

3.1 Phases I and II

During Phase I and Phase II, all five columns were operated in the same manner and thus similar results were obtained (Table 3.1). In Phase I, after running Millipore water for 45 days (52 ~ 60 PV), the corrosion potentials in all five columns reached a quasi-steady state, ranging between -470 and -500 mV at Port I and -520 and -540 mV at Port E. The pH along the columns increased from 6.7 in the influent to 8.6 ~9.4 and 9.6 ~10.2 at Port I and Port E respectively, as a consequence of iron corrosion. After switching to 10 mg/L TCE in Phase II, slight positive shifts in corrosion potentials (20 ~ 40 mV) were observed at both Port I and Port E. This observation was consistent with the results of Lu (2005). TCE degradation profiles exhibited first-order kinetics, with initial half-lives between 2.4 and 3.5 hr at steady state after 42 to 46 PV of TCE addition. Also, with the addition of TCE, the pH in all columns decreased from over 9 to 6.6 ~ 7.8 and 7~ 8 at Port I and Port E, respectively, which is also consistent with the results of Lu (2005). Reduction of TCE released Cl⁻, a strong acid anion, which may have contributed to the decline in pH. Analysis of degradation products gave good carbon mass balances, ranging 80% ~ 110%. Ethene and ethane were the main products, and less than 1% of cis-DCE and VC was detected, which suggests that TCE degraded completely.

Following Millipore water and TCE solution, each column received a different influent solution consisting of various combinations of Cr(VI), TCE and CaCO₃ (Table 2.2). The following sections will describe and discuss the result for each column.

Table 3.1 Corrosion potentials, pH and the initial TCE degradation half-lives for all five columns measured in Phases I and II

Column	Phase I					Phase II					
	PV	pH		Corrosion potential (mV)		PV	pH		Corrosion potential (mV)		TCE degradation half life (hr)
		Port I	Port E	Port I	Port E		Port I	Port E	Port I	Port E	
A	52	9.3	9.6	-490	-530	42	6.6	7.2	-460	-490	3.5
B	60	9	9.9	-500	-540	44	6.8	7.5	-470	-500	2.5
C	56	9.4	10.2	-490	-530	45	6.6	7	-470	-500	2.4
D	53	8.6	9.8	-480	-520	46	6.6	7.8	-470	-500	3.1
E	52	9.2	9.4	-470	-540	45	7.8	8	-460	-490	3.3

3.2 Column A: Cr(VI) as the Only Contaminant

3.2.1 Reaction Kinetics

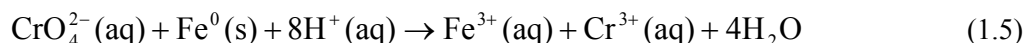
During Phase III, column A received 10 mg/L Cr(VI). Fig. 3.1 shows that at early time (78 PV), Cr(VI) was reduced rapidly by granular iron with 96% removal in 50 min of residence time (at the sampling port 2.5 cm from the influent end). The Cr(VI) profiles migrated further into the column over time, suggesting progressive passivation of the iron. At the end of the experiment (508 PV), there was 45% Cr(VI) removal in 95 min of residence time (at the sampling port 5 cm from the influent end); and the concentration was below MDL (0.05 mg/L) at a residence time of 200 min (at the sampling port 10 cm from the influent end).

Due to the rapid Cr(VI) reduction rate (Fig. 3.1), 90% Cr(VI) reduction was chosen for comparison purposes. The time required for 90% reduction of source Cr(VI) increased from 49 min at 78 PV to over 170 min after more than 500 PV of solution had passed through the column.

3.2.2 Changes in Corrosion Potential, pH, H₂ Formation Rate and Hydraulic Conductivity

The corrosion potentials measured at Port I and Port E in column A are shown in Fig. 3.2 together with the pH values measured close to these two ports. During Phase III, there was a 50 mV initial drop in corrosion potential at Port E (from -490 mV to -540 mV) within the first 20 pore volumes of Cr(VI) addition, and the potential remained relatively stable thereafter. It appears that there was a similar drop in corrosion potential at Port I, from -450 mV to -530 mV; however, unlike Port E, this was followed by a steady increase with the continuing addition of Cr(VI), reaching -270 mV at ca. 400 PV.

The initial drop in potential was observed by Ritter (2000) and Lu (2005) after adding nitrate to the columns. They explained that this phenomenon might be due to the initial corrosion reaction of nitrate with iron, and the introduction of Na⁺ (the counter ion of nitrate), which resulted in an increase in solution pH. An increase in pH results in a decrease in potential based on the Nernst equation. A similar explanation may apply in this study in that K⁺ was the counter ion of Cr(VI). In addition, the reduction of Cr(VI) to Cr(III) by reaction with granular iron (equation 1.5) consumes protons,



which could further contributed to an increase in pH.

As shown in Fig. 3.2, the pH at both ports remained high in Phase III, at values between 9.5 and 10. Compared to the consistently high pH values at Port E, there was a slight gradual decline in pH at Port I, which is likely a consequence of the accumulation of Fe(III)/Cr(III) species and gradual passivation of the iron near the influent end.

Based on the studies of Lu (2005) and Ritter et al. (2003), the addition of nitrate to iron caused an increase in pH and a positive shift in potential by forming non-conducting tri-valent iron oxide species, such as hematite and goethite, on the iron surface. The high valent iron oxides gradually created a film acting as a barrier to further iron corrosion. By analogy, the steady increase in corrosion potential at Port I may be a consequence of the formation of tri-valent iron oxide species at the same time as Cr(VI) was reduced to Cr(III), resulting in the formation of iron oxide films on the iron surface, as well as Cr(III) species. This film gradually passivated the iron material, resulting in the declining rate of Cr(VI) removal (Fig. 3.1). However, due to the rapid reaction rate, detectable Cr(VI) did not reach the port 10 cm from the influent end, and thus the corrosion potential at Port E was not affected and remained at -540 mV.

Fig. 3.3 and Fig. 3.4 show the rates of H₂ production and hydraulic conductivity of the five columns in Phase III. Generally, the rate of hydrogen gas generation in column A was very low, ranging from 0 to 0.003 mL/min. No apparent change in hydraulic conductivity (ranging from 2.6×10^{-4} to 4.6×10^{-4} m/s) was observed. Though solid phases were undoubtedly formed under the condition of this experiment, a higher concentration of Cr(VI) or conducting the experiment for a longer period of time might have resulted in a measurable decline in hydraulic conductivity.

3.2.3 Changes in Oxide Films on Iron Surface

To examine changes on the iron surface, Raman spectroscopic measurements were conducted after 510 PV of Cr(VI) had passed through column A. Based on the Cr(VI) reduction profiles, iron particles were sampled at sampling ports 5cm and 15cm from the influent end. Ten spots were examined for each sample. Fig. 3.5 a₁, a₂ (5 cm from the influent end) and b (15 cm from the influent end) are typical Raman spectra from the two sampling ports.

In spectrum “a₁”, hematite (α -Fe₂O₃) was identified by the peaks at 225, 243, 291, 412, 497 and 613 cm⁻¹. Peaks at 549 and 670 cm⁻¹ were attributed to magnetite (Fe₃O₄).

Some of the characteristic bands of magnetite overlap with the bands of other species, such as goethite (α -FeOOH), Cr₂O₃ and α -CrOOH. Thus, in spectrum “a₂”, it is difficult to discern the specific species near the weak and broad bands at 295 ~ 319, 418 ~ 475 and 539 ~ 553 cm⁻¹. Thus it is

possible that this sample contained Cr^{3+} oxides or hydroxides in addition to Fe^{3+} and $\text{Fe}^{2+}/\text{Fe}^{3+}$ oxides. The Raman band around $665\sim 670\text{ cm}^{-1}$ was attributed to the high intensity of A_{1g} mode of magnetite and the band around $670\sim 686\text{ cm}^{-1}$ was attributed to $\text{Fe}_n\text{Cr}_m\text{O}_4$ spinel (see detail in Section 2.4.2). The two bands are so close that sometimes it is difficult to differentiate the two species. Thus it was expected that the peak at 671 cm^{-1} in spectrum a_2 , contained both magnetite and $\text{Fe}_n\text{Cr}_m\text{O}_4$ spinel.

In spectrum “b”, in addition to the presence of magnetite (667 cm^{-1}), green rust was detected at peaks of 424 and 496 cm^{-1} . In this study, Cr(VI) was not detected at the port 10 cm from the influent end by the end of Phase III, and thus the Raman spectrum “b” would be similar to the studies of Ritter et al. (2002) and Lu (2005), which reported the presence of green rust on iron surfaces when the influent was Millipore water.

Carbon bands ($1323\text{-}1333$, $1583\text{-}1587$, $1613\text{-}1617\text{ cm}^{-1}$), originating from the commercial granular iron, were present in all three spectra of Fig.3.5, and they were also found in all samples examined.

Table 3.2 gives a summary of the species detected in the ten Raman spectra at Port I and Port E of column A. The passivating oxides ($\alpha\text{-Fe}_2\text{O}_3$ and $\alpha\text{-FeOOH}$) and Cr(III) products ($\text{Fe}_n\text{Cr}_m\text{O}_4$ spinel, Cr_2O_3 or CrOOH) were detected primarily at Port I rather than Port E. The detection of hematite ($\alpha\text{-Fe}_2\text{O}_3$) and goethite ($\alpha\text{-FeOOH}$) at Port I is consistent with the study of Pratt et al. (1997), reporting that coatings comprising goethite and hematite with Cr(III) species were developed on the iron surface when Cr(VI) solutions passed through the iron column. The passivating oxides near Port I are consistent with the increasing corrosion potential at port I (Fig. 3.2) and passivation of the iron as indicated by the declining rate of Cr(VI) removal (Fig. 3.1).

Table 3.2 Raman spectroscopic analysis of surface composition on iron grains taken from Column A

Column A (10 mg/L Cr(VI))							
sample information	α -Fe ₂ O ₃	α -FeOOH	Fe ₃ O ₄	Fe _n Cr _m O ₄ spinel	Cr ³⁺ (Cr ₂ O ₃ or CrOOH)	Green rust	carbon graphite carbides
Port I (10 spots studied)	4	5	10	5	2	0	10
Port E (10 spots studied)	2	0	10	0	0	5	10

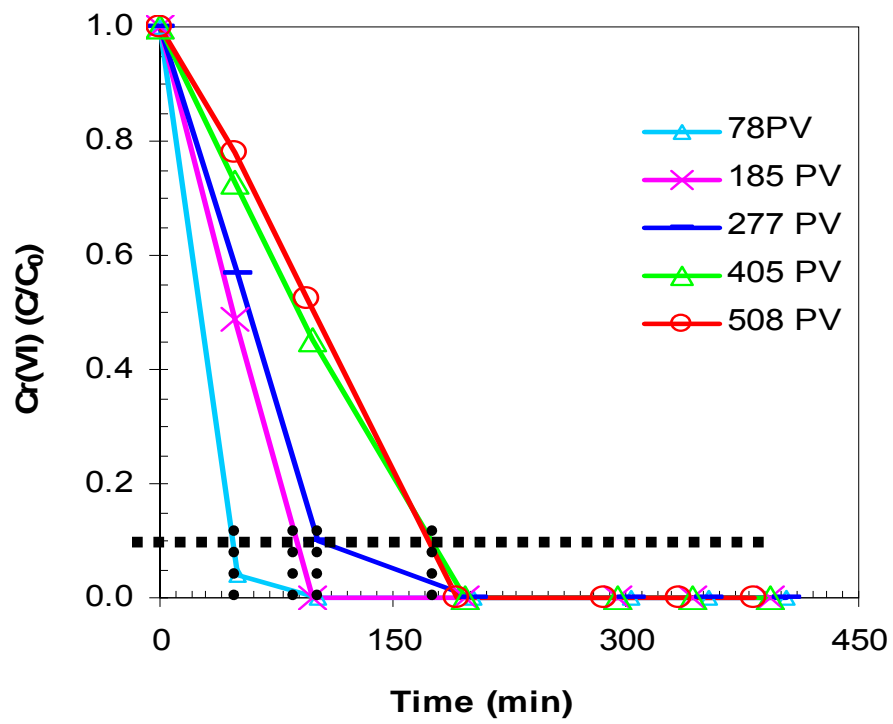


Figure 3.1 Cr(VI) reduction profiles obtained from column A

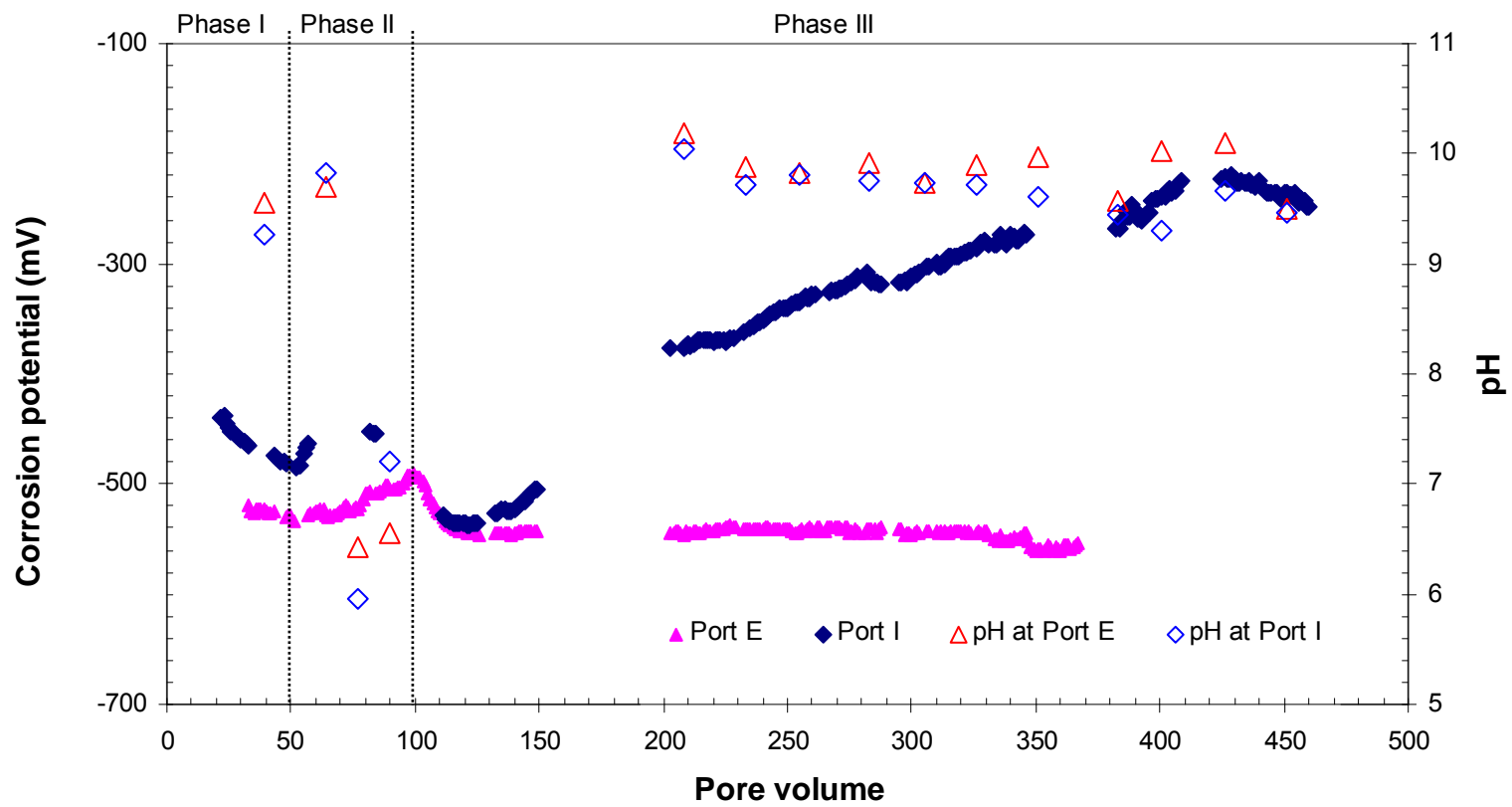


Figure 3.2 Corrosion potential and pH changes in column A

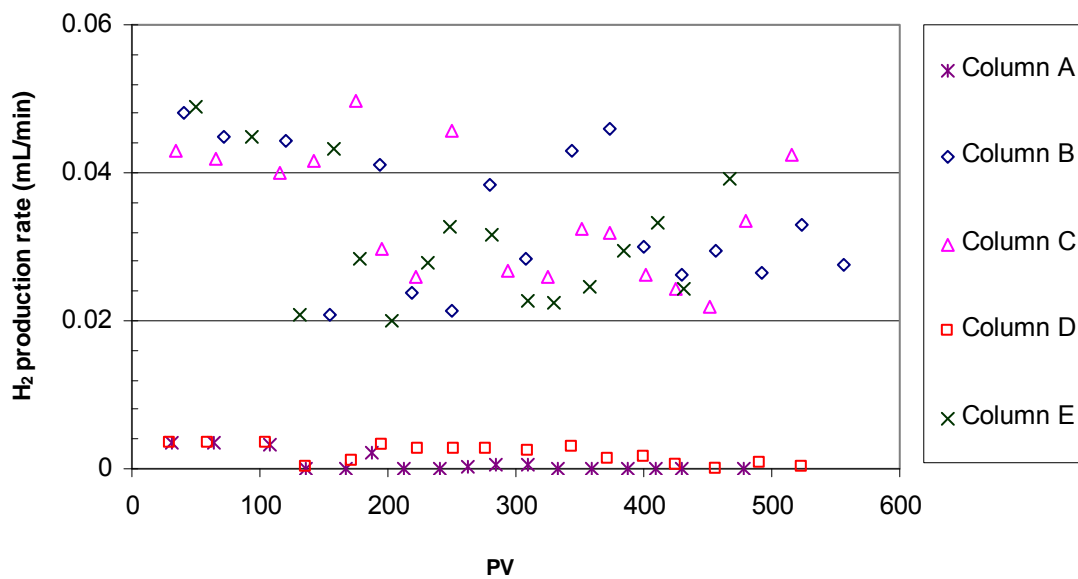


Figure 3.3 The measured rates of H₂ production rate in columns A, B, C, D and E in Phase III

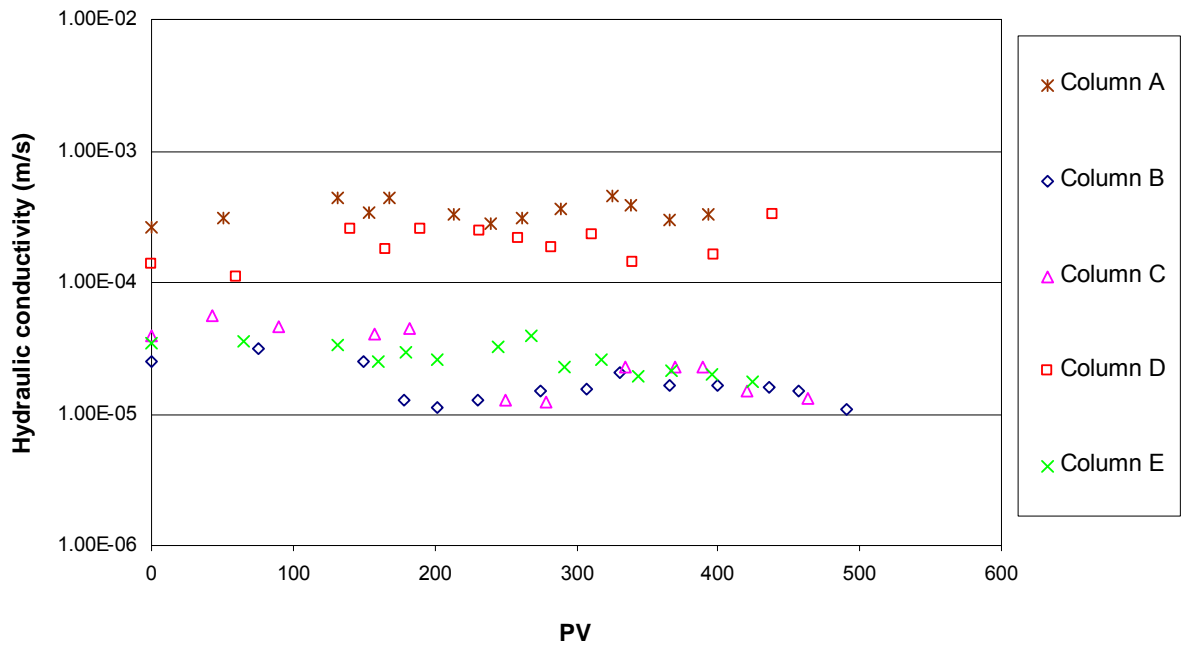


Figure 3.4 The measured hydraulic conductivities in columns A, B, C, D and E in Phase III.

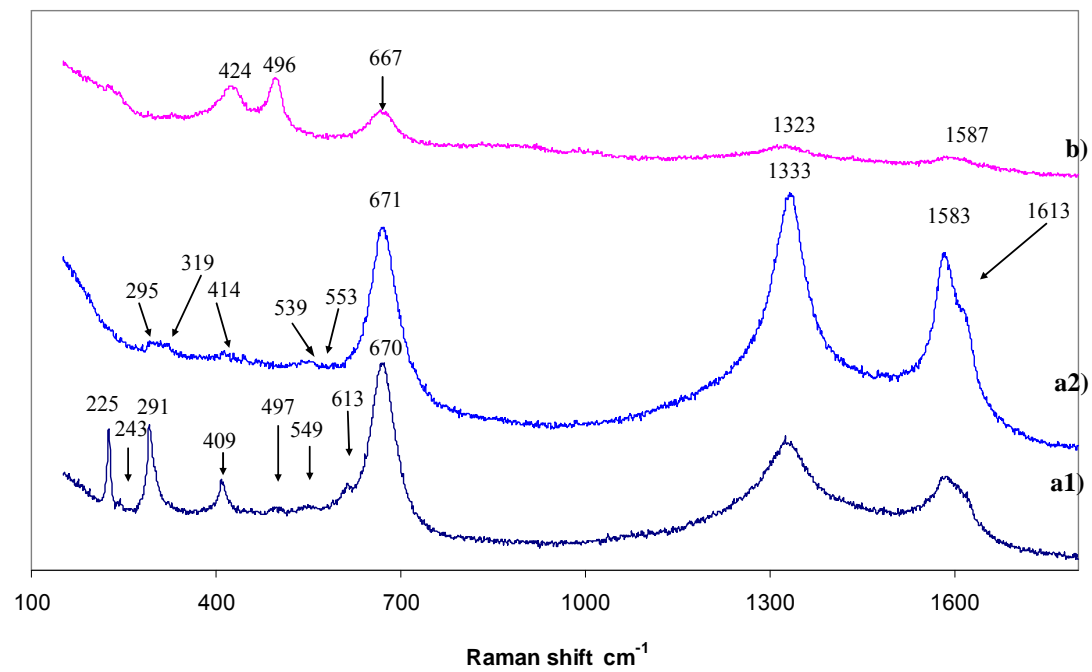


Figure 3.5 Spectra of iron surfaces at ports 5 cm from the influent end (a1 and a2) and 15 cm from the influent end (b) in column A.

3.3 Column B: Cr(VI) in the Presence of CaCO₃

3.3.1 Reaction Kinetics

Column B received 10 mg/L Cr(VI) + 300 mg/L CaCO₃ during Phase III. Fig. 3.6 shows that the Cr(VI) concentrations decreased very rapidly along the column. At a residence time of ca. 40 min (at the sampling port 2.5 cm from the influent end), Cr(VI) was not detected until 355 PV of Cr(VI) solution had passed through the column. Subsequent analyses showed that the Cr(VI) profiles migrated over time, indicating the gradual passivation of the iron surfaces. After 499 PV and 658 PV, about 40% and 23% of the influent Cr(VI) were reduced, respectively, at the same residence time (at the same port). No Cr(VI) was detected beyond the port 5 cm from the influent end (residence time of ca. 80 min).

Similar to the Cr(VI) profiles in column A, the kinetics of Cr(VI) reduction was not first-order. The time needed for reducing 90% of the source Cr(VI) increased from 40 min at 355 PV to around 80 min when over 600 PV of solution had passed through the column. Compared with column A, the presence of CaCO₃ in column B enhanced Cr(VI) reduction, e.g., at the end of the experiment, Cr(VI) was fully removed at 80 min of residence time in column B, whereas Cr(VI) was fully removed at 170 min of residence time in column A.

3.3.2 Alkalinity Profiles, pH, Changes of Corrosion Potentials, H₂ Generation Rate and Hydraulic Conductivity

Fig. 3.7 shows alkalinity profiles for column B. At early time, the removal of alkalinity occurred mainly in the portion close to the influent end and almost all source alkalinity was removed through the column. As more solution passed through the column, the decline in alkalinity occurred further into the column and the rate of loss declined.

The pH and corrosion potentials measured at Port I and Port E are shown in Fig. 3.8. In phase III, the pH remained in the range from 7 to 7.6 at Port I and decreased from above 9 at earlier time to 7.8 at later time at Port E. The presence of carbonate in the source solution buffered the pH in the system. Thus, unlike column A, the pH near the influent end (Port I) did not increase significantly from the low value in Phase II (6.8 in Table 3.1) due to Cr(VI) reduction. On the other hand, the rise in pH from the reduction of Cr(VI) by granular iron shifted the carbonate-bicarbonate equilibrium, resulting in the precipitation of carbonate minerals. Initially, the alkalinity was consumed substantially near the influent end, but did not affect the upper portion of the column significantly. Thus, the pH near Port E remained high (above 9). As carbonate minerals continued to precipitate and

accumulate, the iron material became passivated. Subsequently, the precipitation front migrated towards to the effluent end. Therefore, the pH values at Port E decreased and approached the values at Port I at later times. This result was consistent with the study of Jeon (2005).

Fig. 3.8 shows that after introducing a solution containing 10 mg/L Cr(VI) + 300 mg/L CaCO₃, the corrosion potential declined by almost 40 mV at Port E (from about -500 mV to -540 mV) within the first 20 pore volumes, remained at -540mV for the next 20 PV, then increased to -510 mV within the following 15 PV. Over the next period of more than 500 PV of continuing addition of Cr(VI) and CaCO₃ solution, the potential increased only slightly from -510 to -490mV. The corrosion potential at Port I followed a similar pattern. There was a 30mV initial drop (from around -460mV to -490mV) within the first 40 pore volumes of Cr(VI) + CaCO₃ addition, and then increased by 20mV during the next several pore volumes. After this, there was a 70 mV steady increase (from -470 to -400 mV) over the period of more than 500 PV.

The variations in corrosion potentials during the first 50 PV at both Port I and Port E may be due to the buffering effect of CaCO₃, which enhanced iron corrosion by lowering pH. Thus, the reduction of Cr(VI) was faster than in column A. The reduction of Cr(VI) caused iron passivating oxides to form in the lower portion of the column, increasing the corrosion potential at Port I (see detailed description in section 3.2.2). The increase in corrosion potential at Port I was offset by the buffering effect of CaCO₃, and eventually the increase of corrosion potential was only 70mV at Port I over the period of Phase III, much smaller than in column A (+180mV shift). Due to the complete reduction of Cr(VI) before the solution reached the port 5 cm from the influent end (Fig. 3.6), the slight +20 mV shift in corrosion potential at Port E may have been caused by the steady decrease in pH in Phase III.

The H₂ generation rate in column B (Fig. 3.3) ranged from 0.02 to 0.04 mL/min, one order of magnitude higher than in column A. This confirmed the enhancing effect of CaCO₃ on iron corrosion. There was a slight decrease in hydraulic conductivity, with values ranging from 3.1×10^{-5} to 1.1×10^{-5} m/s (Fig. 3.4).

3.3.3 Changes in Oxide Films on Iron Surface

Raman spectroscopic measurements were conducted when 550 PV of Cr(VI) and CaCO₃ had passed through column B. Fig. 3.9 a and b are typical examples of Raman spectra for the surface of iron particles taken from the bottom of the column (near Port I) and 15 cm from influent end (near Port E).

Besides carbon bands, magnetite was detected in most of the spectra from both Port I and Port E (The detail band assignments are similar to those described for column A in section 3.2.3). Peaks at 250, 299 and 396 cm^{-1} in spectrum “a” indicate the presence of goethite ($\alpha\text{-FeOOH}$). Because the band around 550 cm^{-1} is common for goethite and $\text{Fe}_n\text{Cr}_m\text{O}_4$ spinel, the band at 554 cm^{-1} would likely be either goethite or $\text{Fe}_n\text{Cr}_m\text{O}_4$ spinel or a mixture of the two. Aragonite (CaCO_3) was identified at 154 and 1086 cm^{-1} in both spectra “a” and “b”, and was also identified at 203 cm^{-1} in spectrum “a”. The peak at 1070 cm^{-1} in spectrum “b” was attributed to free CO_3^{2-} .

Table 3.3 summarizes the species detected by Raman spectroscopy at Port I and Port E. Secondary carbonate minerals (aragonite and calcite), conducting oxides (magnetite and $\text{Fe}_n\text{Cr}_m\text{O}_4$ spinel), and free CO_3^{2-} were detected from both Port I and Port E. The precipitation of aragonite may have caused the slight decrease in hydraulic conductivity. The passivating iron oxide, goethite, was detected more frequently in spectra from Port I than from Port E. The detection of iron oxides is consistent with migration of the Cr(VI) profiles (Fig. 3.6).

Table 3.3 Raman spectroscopic analysis of surface composition on iron grains taken from Column B

Column B(10 mg/L Cr(VI) + 300 mg/L CaCO ₃)							
sample information	Aragonite and calcite	α -FeOOH	α -Fe ₂ O ₃	Fe ₃ O ₄	Fe _n Cr _m O ₄ spinel	Free CO ₃ ²⁻	carbon graphite carbides
Port I (10 spots studied)	6	6	2	7	4	8	10
Port E (10 spots studied)	6	2	0	8	1	10	10

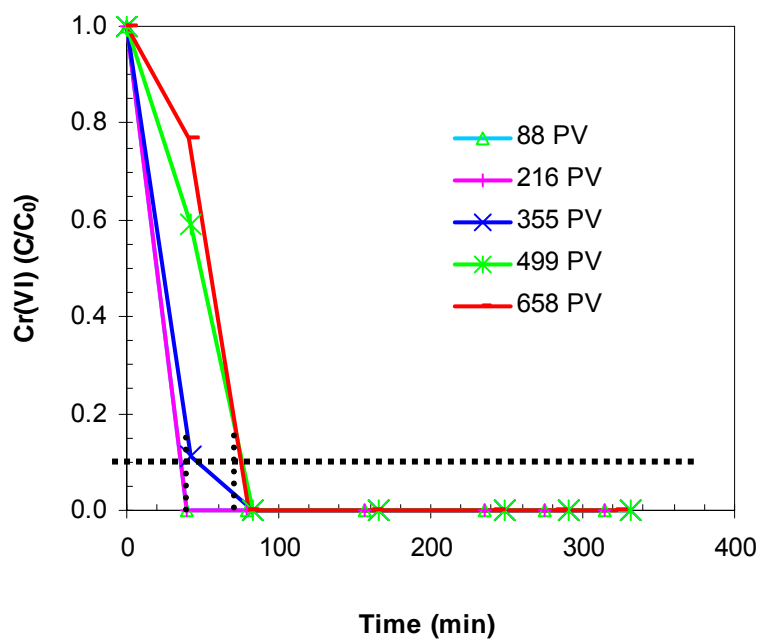


Figure 3.6 Cr(VI) profiles obtained from column B

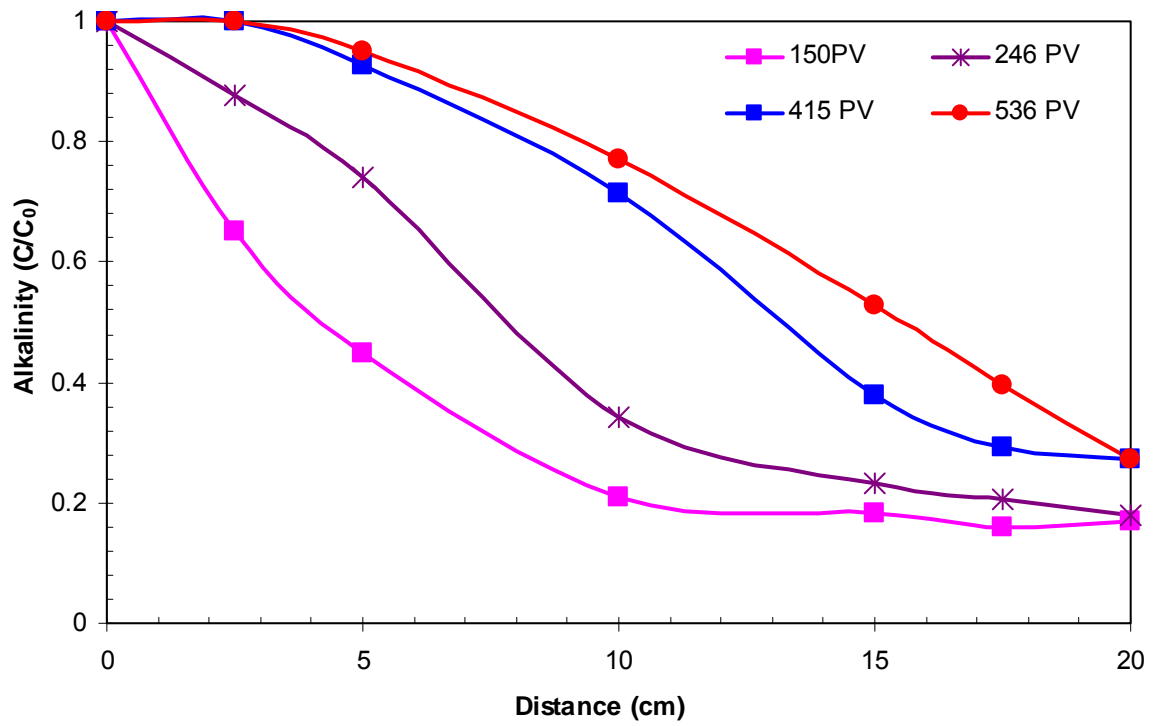


Figure 3.7 Alkalinity profiles obtained from column B

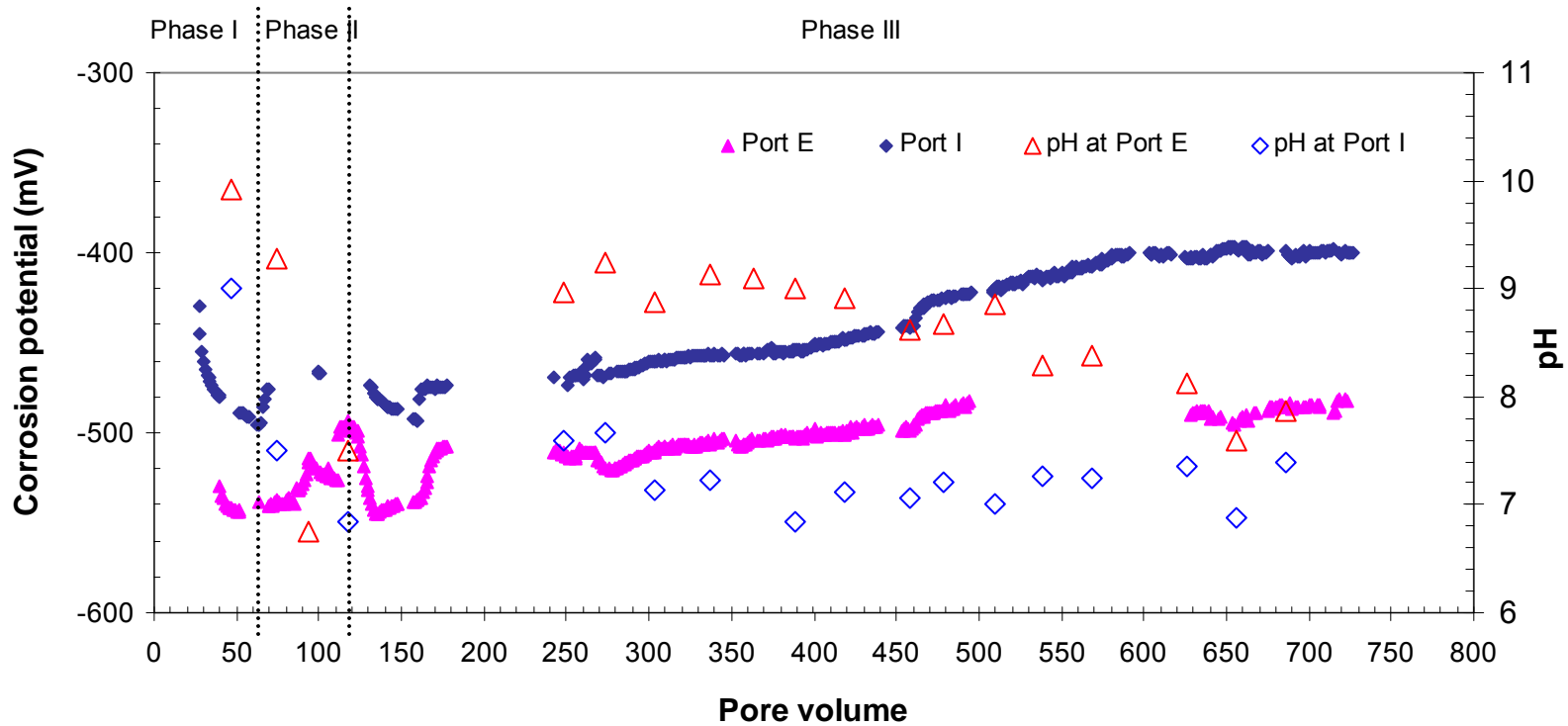


Figure 3.8 Corrosion potential and pH changes in Column B.

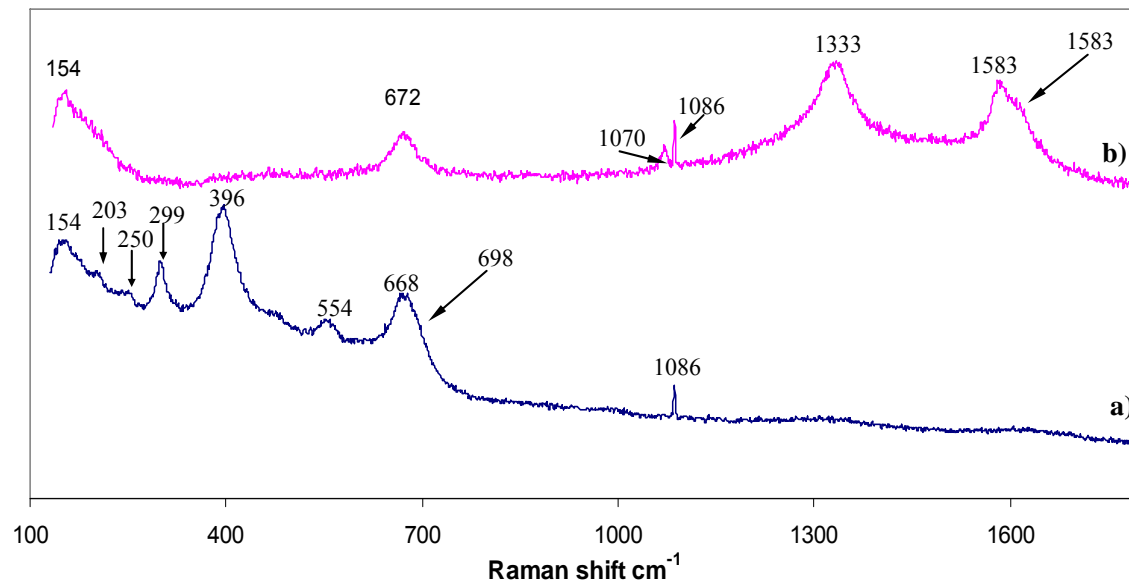


Figure 3.9 Spectra of iron surfaces at bottom of the column (a) and at port 15 cm from the influent end (b) in column B.

3.4 Column C: TCE in the Presence of CaCO₃

3.4.1 Reaction Kinetics

Column C received 10 mg/L TCE during Phase II and 5 mg/L TCE + 300 mg/L CaCO₃ during Phase III. Fig. 3.10 shows one TCE profile in Phase II (45 PV, dashed line), and the migration of TCE profiles in Phase III (solid lines). The flow rate during Phase II was 0.12 mL/min and during Phase III was 0.35 mL/min. Fig. 3.10 shows that the addition of CaCO₃ enhanced TCE degradation significantly. However, migration of the TCE profiles with continuous addition of CaCO₃ in Phase III indicates the gradual passivation of the iron materials, and TCE was not fully degraded (90% removed) after 576 PV passed through the column.

TCE degradation followed pseudo-first-order kinetics in Phases II and III. Due to the enhancement of CaCO₃, TCE degradation half-life decreased from 2.4 hr right before switching to Phase III to 30 min at the beginning of Phase III. Thereafter, the half-life gradually increased and reached 80 min at 576 PV due to the passivation of iron, likely by secondary carbonate precipitates.

3.4.2 Alkalinity Profiles, pH, Changes of Corrosion Potential, H₂ Generation Rate and Hydraulic Conductivity

Fig. 3.11 shows the alkalinity profiles for column C. The migration of the profiles was similar to that observed for column B (Fig. 3.7).

The pH and corrosion potentials measured at Port E and Port I are shown in Fig. 3.12. In Phase III, the pH at Port I remained low (6.6 ~7.2), and the pH at Port E decreased from 8.8 at the earlier time to 7.2 at the end of the experiment. This pH trend is similar to that of column B. The buffering effect of carbonate resulted in stable and low pH values at Port I. The shift of the carbonate-bicarbonate equilibrium due to the pH increase with iron corrosion resulted in the accumulation and migration of carbonate minerals from the influent end to the effluent end of the column, which in turn caused a gradual decrease in pH at Port E. Even though the pH trends are similar, the initial pH values at Port I in column C (below 9) were lower than those in column B (above 9). Cr(VI) reduction by granular iron (column B) results in a higher pH whereas TCE degradation by granular iron (column C) results in lower pH. This result is consistent with previous studies (Mayer et al., 2001; Jeen, 2005).

The early stage corrosion potential measurements in Phase III were disrupted due to power failure. However, the period for which data are available shows no obvious changes in corrosion potential at both Port I and Port E (Fig. 3.12). The potentials at ports E and I ranged from -510 to -480 mV and -460 to -440mV, respectively. Based on the studies of Ritter (2000) and Lu (2005), when

TCE was introduced to a granular iron column, only magnetite and/or green rust and very small amounts of iron passivating oxides were detected on the iron surfaces. Thus, the degradation of TCE by granular iron does not cause the positive shift in corrosion potential and the passivation of the iron material. However, migration of the TCE profiles in Phase III (Fig. 3.10) indicates that the iron material in the column was passivated. Therefore, it appears that the iron passivation is caused by the precipitation of the secondary carbonate minerals, and the minerals do not cause large changes in corrosion potential.

The H₂ generation rate in column C (Fig. 3.3) ranged from 0.02 to 0.05 mL/min, similar in magnitude to that of column B. There was a slight decrease in hydraulic conductivity with values ranging from 5.6×10^{-5} to 1.2×10^{-5} m/s (Fig. 3.4).

3.4.3 Changes in Oxide Films on Iron Surface

Raman spectroscopic measurements were conducted after 590 PV of CaCO₃ and TCE solution had passed through column C. The species detected on iron surfaces near both Port I (bottom of the column) and Port E (15 cm from influent end) were similar and thus only one example spectrum from Port I is displayed in Fig. 3.13.

Besides carbon bands (1333, 1583, 1617cm⁻¹), aragonite was detected at bands 152, 205 and 1084 cm⁻¹. Magnetite was found at bands 305, 537 and 667cm⁻¹. Free CO₃²⁻ was found at peaks 1068 cm⁻¹.

Table 3.4 gives a summary of the species detected by Raman spectroscopy at Port I and Port E. Abundant aragonite and free CO₃²⁻ were detected from both Port I and Port E. However, compared with column B, much less passivating iron oxides, such as hematite and goethite, were detected on samples from Port I than in column B. Raman spectroscopy results confirm that the passivation of the iron materials towards degradation of TCE in Phase III (Fig. 3.10) was caused by the formation and accumulation of secondary carbonate minerals (aragonite), even though it did not cause measurable changes in corrosion potential.

Table 3.4 Raman spectroscopic analysis of surface composition on iron grains taken from Column C

Column C (300 mg/L CaCO ₃ + 5 mg/L TCE)					
sample information	aragonite and calcite	α-FeOOH	Fe ₃ O ₄	Free CO ₃ ²⁻	carbon graphite carbides
Port I (10 spots studied)	8	1	8	10	10
Port E (10 spots studied)	9	0	6	10	10

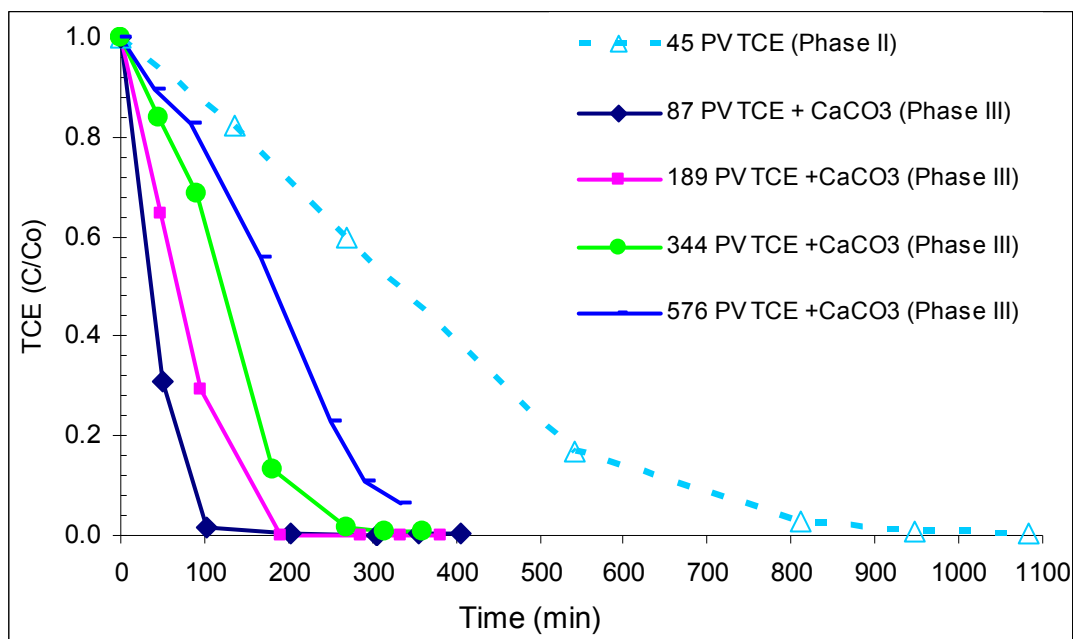


Figure 3.10 TCE profiles before and after CaCO₃ addition for column C.

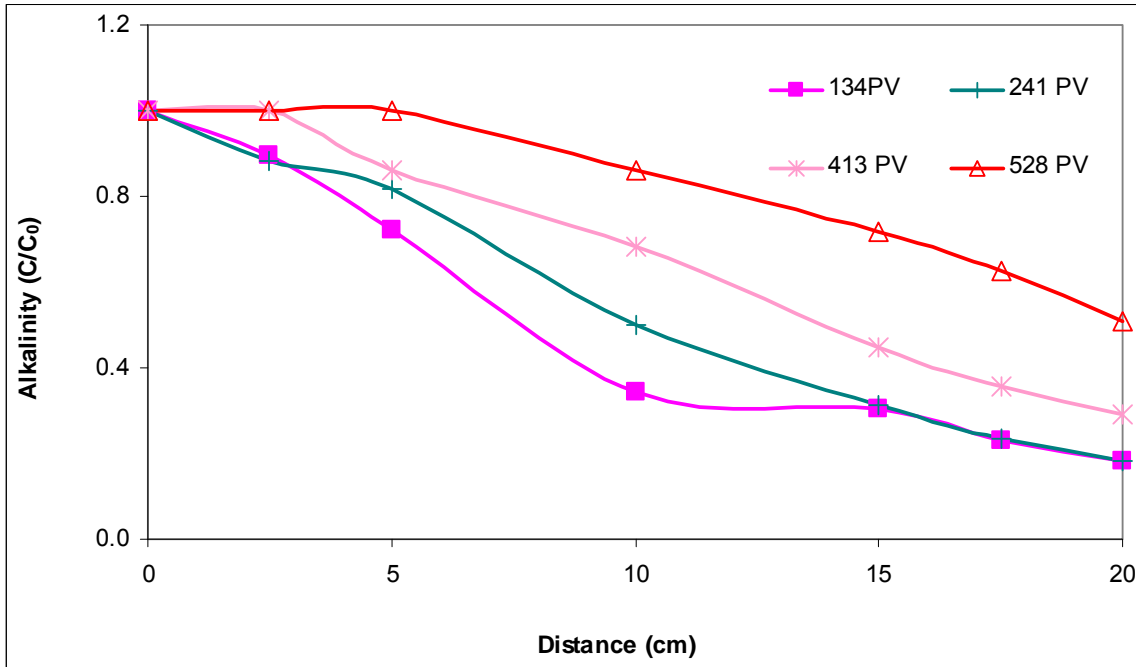


Figure 3.11 Alkalinity profiles in column C

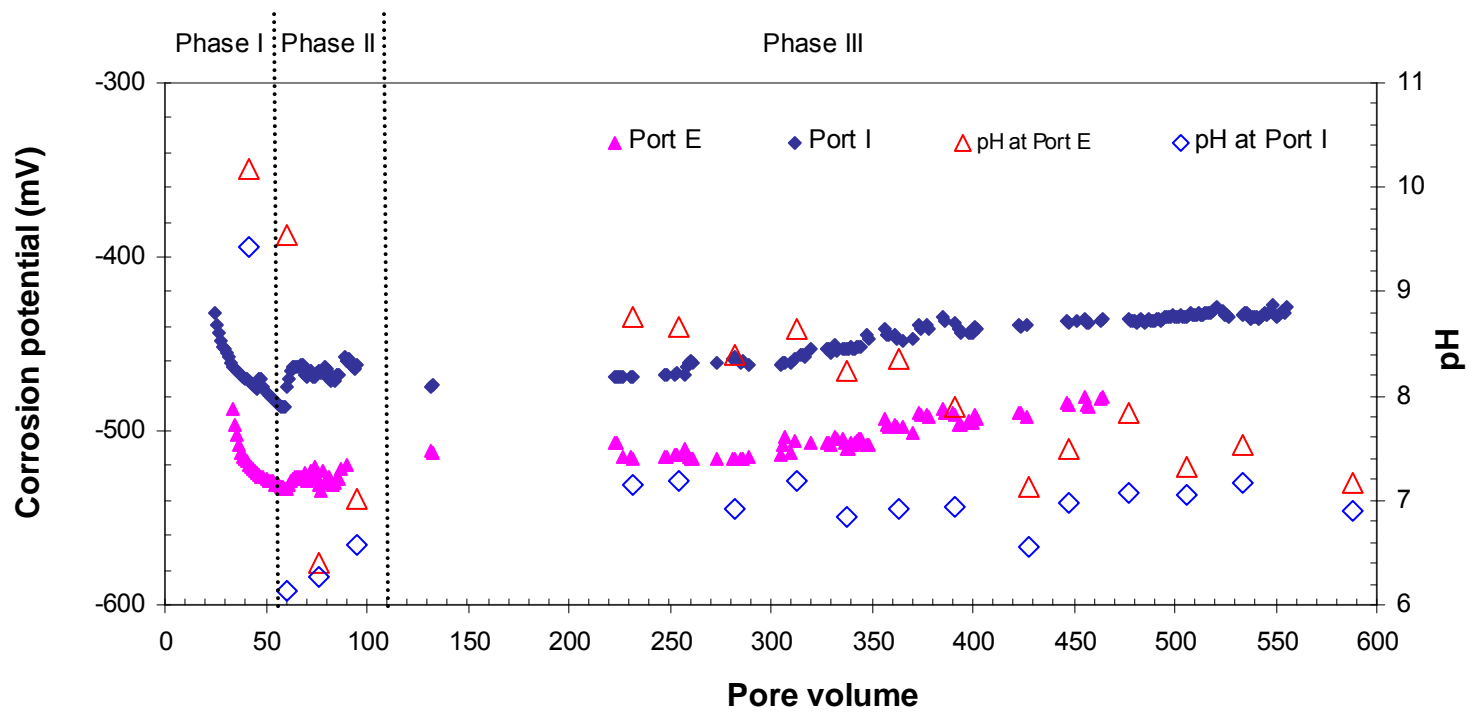


Figure 3.12 Corrosion potential and pH changes in Column C

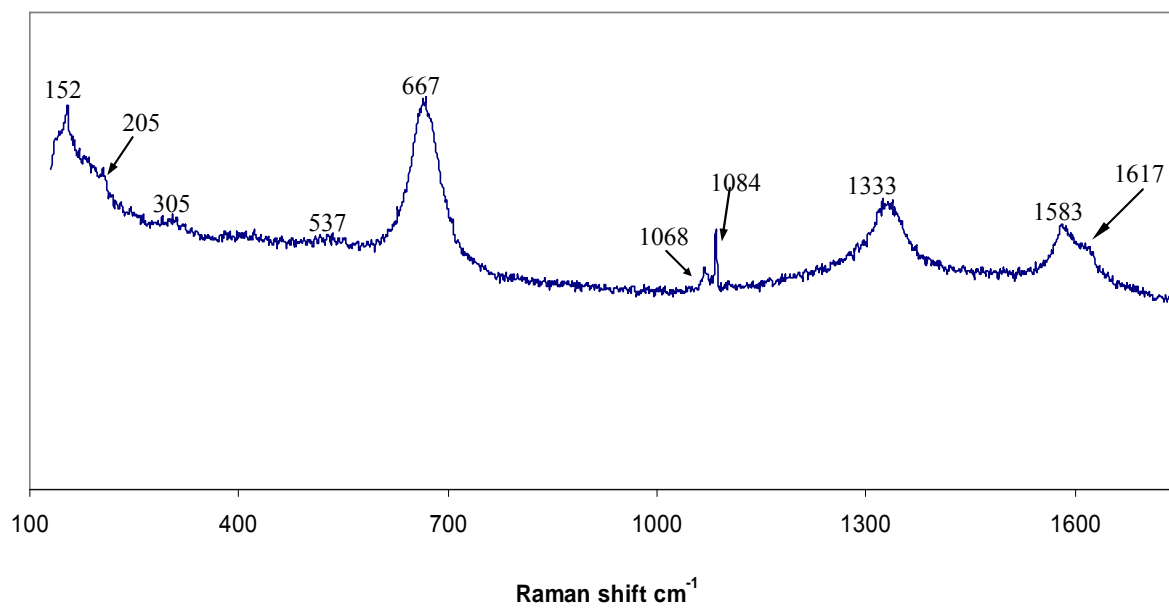


Figure 3.13 Spectrum of iron surfaces in column C

3.5 Column D: TCE Co-existing with Cr(VI)

3.5.1 Reaction Kinetics

Column D received 10 mg/L TCE during Phase II, and 5 mg/L TCE + 10 mg/L Cr(VI) during Phase III. Fig. 3.14 shows one TCE profile taken immediately before switching from Phase II to Phase III (short dashed line), four TCE (solid lines) and Cr(VI) (long dashed lines) profiles at similar pore volumes during Phase III. The flow rate was 0.12 mL/min in Phase II and 0.35 mL/min in Phase III. Both TCE and Cr(VI) profiles migrated in Phase III, indicating passivation of the iron surface. However, the reactivity losses of iron towards TCE and Cr(VI) reduction are different.

The TCE profile in Phase II followed pseudo-first order kinetics, with a half-life of 3.1 hours. In Phase III, the earliest TCE profile (50 PV) is similar to that in Phase II (Fig. 3.14). However, with the continuous addition of TCE + Cr(VI) solution, the TCE profiles deviated from pseudo-first-order kinetics. The migration of the TCE profiles can be divided into two segments. The first segment is from the influent end to 5 cm along the column (up to a residence time of 100 min) (Fig. 3.14), in which the TCE degradation rate decreased very rapidly until, eventually, at 538 PV, there was no degradation. The second segment is beyond 5 cm from the influent end to the effluent end, in which the TCE degradation profile could still be represented by a pseudo-first-order kinetic model. After 538 PV, approximately 35% of the TCE was degraded by the effluent end.

Cr(VI) was reduced rapidly even though the profiles migrated over the period of Phase III. At 74 PV, Cr(VI) was reduced very rapidly and was fully removed at 50 min of residence time. Over time, the Cr(VI) profiles migrated. At the end of the experiment (569 PV), 75% of source Cr(VI) was removed at 100 min of residence time and no Cr(VI) was detected at 200 min of residence time. Generally, Cr(VI) profiles in column D are similar to those in column A (Fig. 3.1), which received solution containing Cr(VI) only.

The TCE and Cr(VI) profiles in Fig. 3.14 indicate that when TCE and Cr(VI) co-exist, Cr(VI) reduction by granular iron is more competitive than TCE degradation. In Segment 1, TCE degradation was fully inhibited up to a residence time of 100 min (at the port 5 cm from the influent end) after ca. 300 PV, while over 50% of Cr(VI) was reduced at the same location at the last sampling event (569 PV, day 148). In Segment 2, no Cr(VI) was detected after 190 min of residence time (at the 4th sampling port, 10cm from the influent end) at 569 PV, while only 15% of TCE was removed at the same location with similar pore volumes.

3.5.2 Changes of Corrosion Potential, pH, H₂ Generation Rate and Hydraulic Conductivity

The corrosion potentials measured at Port I and Port E are shown in Fig. 3.15 together with the pH values measured close to those ports. During Phase III, there was a 40mV initial corrosion potential drop at Port E (from around -500mV to -540mV) within the first 30 pore volumes, and the potential remained stable at -540mV with the continuous addition of solution. For Port I, there was a 60mV (from -470mV to -530mV) corrosion potential drop within the first 40 PV; however, this initial potential drop was temporary. Though there are data gaps, it is clear that the corrosion potential started to increase at ca. 40 PV, and rose rapidly to -290mV at ca. 200 PV. After this, there was a slight increase of 50mV over the next 300 PV addition of Cr(VI) + TCE.

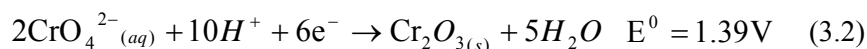
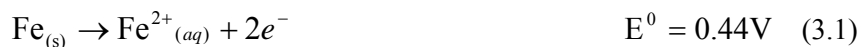
Similar to column A, the reduction of Cr(VI) to Cr(III) by granular iron and the counter cation K^+ in the solution resulted in the increase in pH in the column. In this column, though the degradation of TCE contributed to the decrease in pH, it was minimal compared to the increase in pH due to Cr(VI) reduction. Therefore, the pH at Port I and Port E are very high, with values ranging from 9.5 to 10.1 (Fig. 3.15), which caused the initial drop in corrosion potential at Port I and Port E.

After the initial drop, the increase at Port I and constantly low values at Port E indicate that passive oxides formed and accumulated in the lower portion of the column, and the migration front did not reach Port E by the end of the experiment. The passive oxides in the lower portion of the column gradually passivated the iron surface, resulting in migration of the TCE and Cr(VI) profiles (Fig. 3.14).

It is interesting to note that there is a match between the increase in corrosion potential at Port I (Fig. 3.15) and migration of the TCE profiles in Segment 1 (Fig. 3.14). From 40 PV to ca. 200 PV, a positive shift of 180 mV in corrosion potential was observed at Port I, and at the same time, the TCE degradation rate decreased rapidly. The slight +50 mV shift in corrosion potential from ca. 200 PV to 540PV corresponds to the continuing but slower decrease in TCE degradation from 216 PV to 538 PV (Fig. 3.14).

The chemical reactions in the column containing both TCE and Cr(VI) include iron corrosion (3.1), Cr(VI) reduction (3.2) and TCE degradation. Two mechanisms have been proposed for TCE degradation: direct electron transfer (Arnold and Roberts, 2000) and catalytic hydrogenation (Li and Farrell, 2002). Based on research of Arnold and Roberts (2000), β -elimination accounted for 97% of TCE degradation. In this experiment, less than 1% of cis-DCE was detected as the intermediate

product of TCE degradation and the degradation rate of cis-DCE was slower than TCE. Therefore, TCE degrades more likely through the β -elimination reaction (3.3).



Comparing the three reactions above, the differences in the reduction potentials for the coupled half reactions of (3.1) and (3.3) is much smaller than that of the coupled reactions of (3.1) and (3.2). Thus, thermodynamically, Cr(VI) reduction is much more competitive than TCE degradation by granular iron. The commercial iron (Connelly) used in this study is covered with oxides. The iron with defects and cracks in the surface could be more reductive, while the other areas with less pits and cracks may be less reductive conditions. In this experiment, the measured corrosion potential was an average value for the area proximal to the reference electrode, ranging from 0.46 to 0.50 mV. In this case, the driving force for TCE degradation by corroding iron is on the margin, much smaller than that of Cr(VI) reduction to corrode iron, as clearly demonstrated in the results from Segment 1 (Fig. 3.14).

The H_2 generation rate in column D in Fig. 3.3 ranged from 0.0003 to 0.005 mL/min, over one order of magnitude lower than in columns B and C, but similar to column A. However, there is no obvious trend in the hydraulic conductivity in column D with values ranging from 1.1×10^{-4} to 3.3×10^{-4} m/s (Fig. 3.4).

3.5.3 Changes in Oxide Films on Iron Surface

Raman spectroscopic measurements were conducted when 540 PV of Cr(VI) + TCE had passed through column D. Fig. 3.16 a (5 cm from influent end) and b (15 cm from influent end) are examples of typical Raman spectra for the iron surface from these two sampling ports.

In spectrum “a”, bands at 223, 241, 291, 406, 488, 609 cm^{-1} were attributed to hematite. Cr_2O_3 was detected at bands 377, 541 cm^{-1} , and was not detected in spectrum “b” from Port E.

In spectrum “b”, green rust was detected at bands 433 and 479 cm^{-1} , and $[\text{FeCl}_2(\text{H}_2\text{O})_4]^+$ complex was detected at bands 232 and 330 cm^{-1} . CrO_4^{2-} was detected at band 368 cm^{-1} . The reason was not clear why CrO_4^{2-} was detected in a few spots on grains from Port E but no detection from

Port I (Table 3.5). The common species found from Port I and Port E were carbon graphite (1327, 1582, 1601~1614 cm^{-1}) and magnetite (670 cm^{-1}).

Table 3.5 summarizes all the species detected by Raman spectroscopy and shows that more passivating iron oxides, hematite and goethite, and Cr(III) products were detected at Port I than at Port E, which supports the positive shift in corrosion potential at Port I (Fig. 3.15) and migration of the TCE and Cr(VI) profiles (Fig. 3.14).

Table 3.5 Raman spectroscopic analysis of surface composition on iron grains taken from Column D

Column D (10 mg/L Cr(VI)+5 mg/L TCE)									
sample information	α - Fe ₂ O ₃	α - FeOOH	Fe ₃ O ₄	Fe _n Cr _m O ₄ spinel	Cr ³⁺ (Cr ₂ O ₃ or CrOOH)	[FeCl ₂ (H ₂ O) ₄] ⁺	Green rust	CrO ₄ ²⁻	carbon graphite carbides
Port I (10 spots studied)	6	2	9	4	3	0	0	0	10
Port E (10 spots studied)	1	0	10	1	0	6	9	3	10

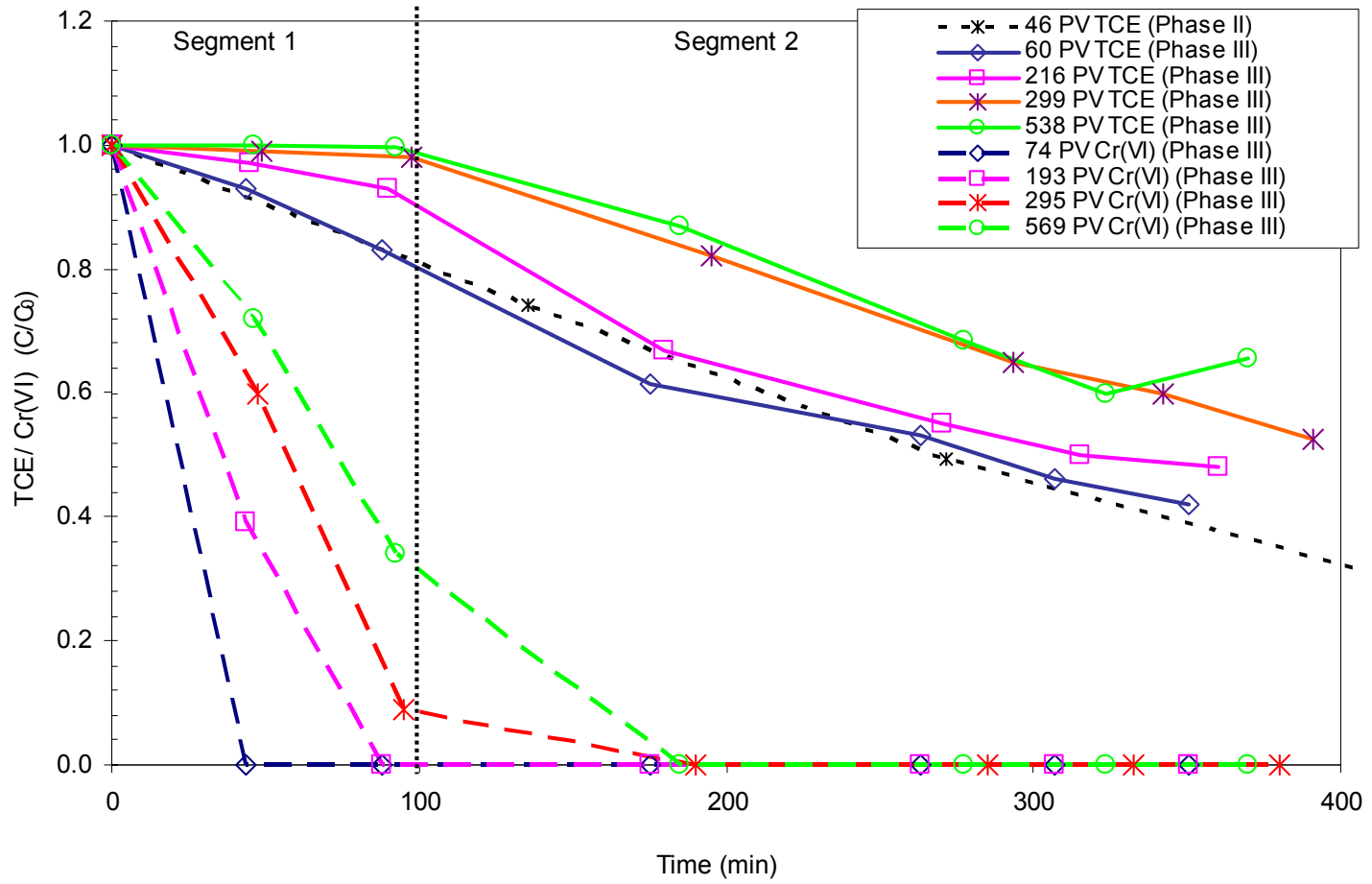


Figure 3.14 TCE and Cr(VI) profiles obtained from column D

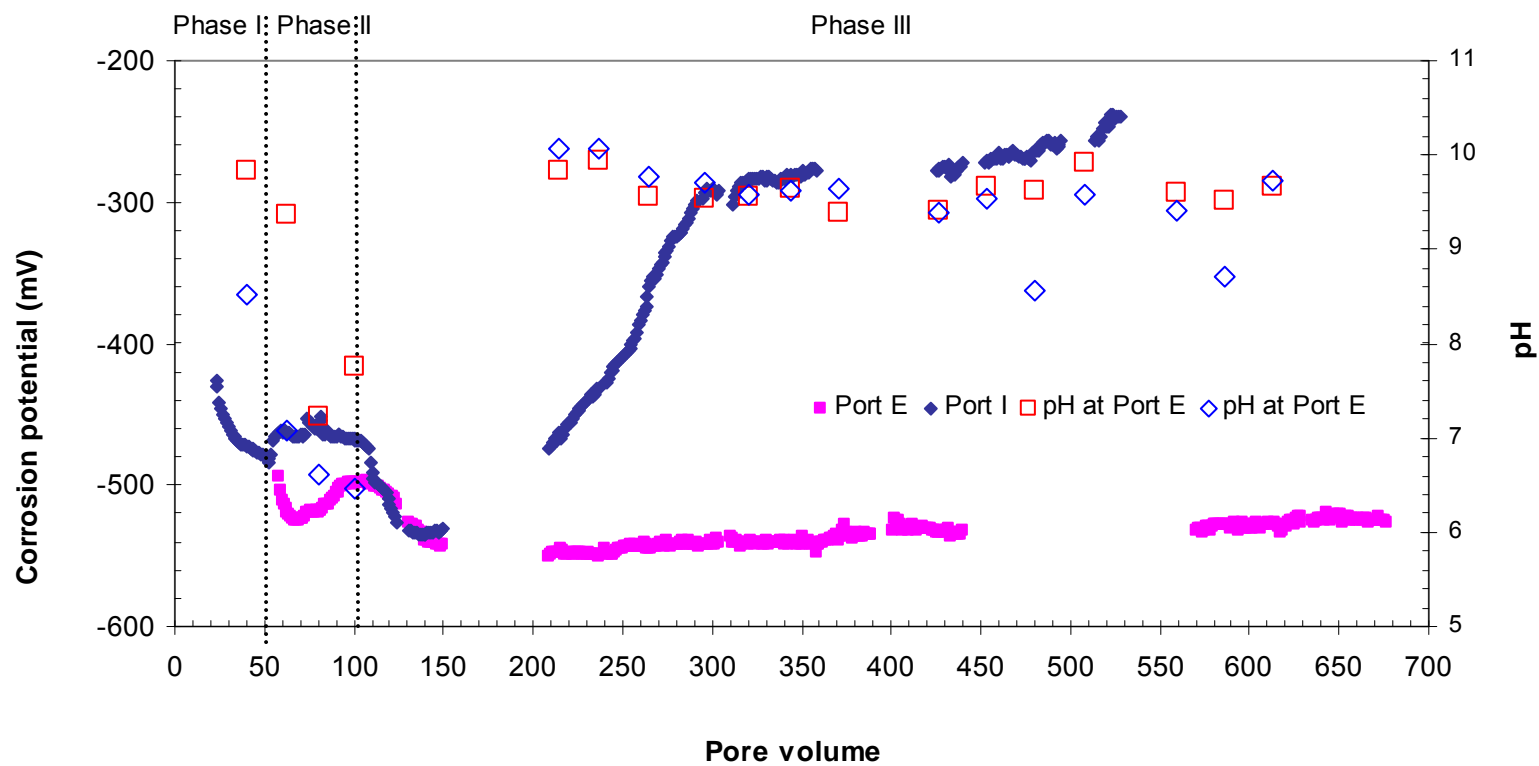


Figure 3.15 Changes of corrosion potential and pH in column D.

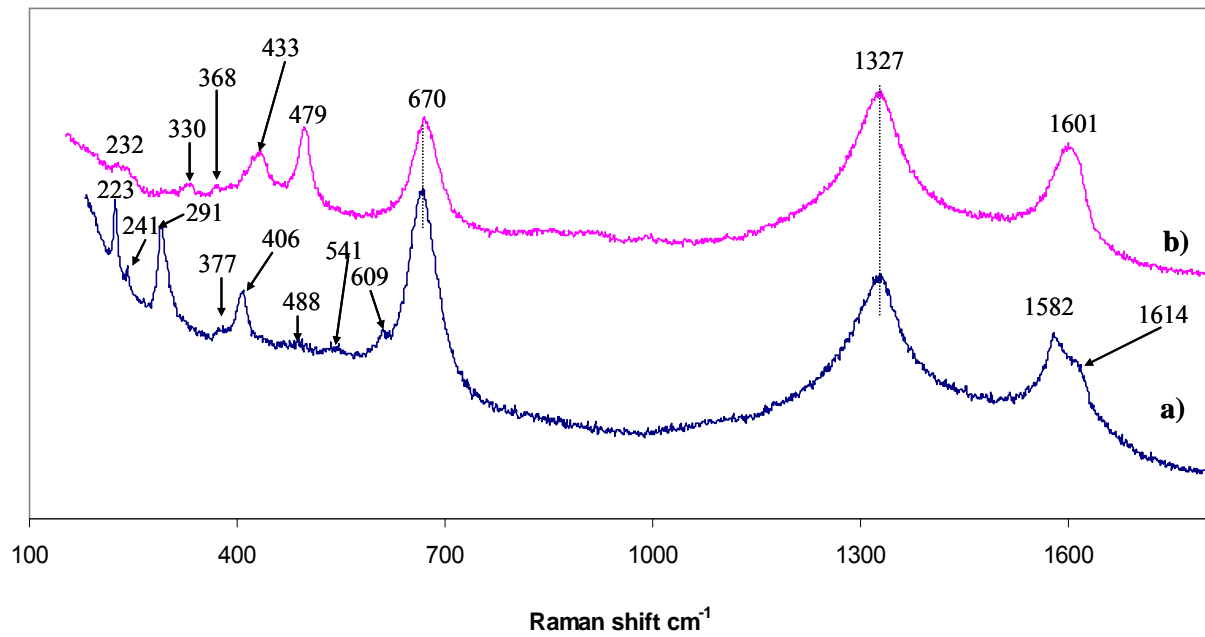


Figure 3.16 Spectra of iron surfaces at ports 5 cm from the influent end (a) and 15 cm (b) from the influent end in column D

3.6 Column E: TCE Co-existing with Cr(VI) in the Presence of CaCO₃

3.6.1 Reaction Kinetics

Column E received 5 mg/L TCE + 10 mg/L Cr(VI) + 300 mg/L CaCO₃ during Phase III. Fig 3.17 shows one TCE profile in Phase II (short dashed line), four TCE (solid lines) and Cr(VI) (long dashed lines) profiles at similar pore volumes during Phase III. In this column, the shifts in both TCE and Cr(VI) profiles in Phase III are similar to those observed in column D; however, the extent of migration is less than in column D, because of the presence of CaCO₃.

In Phase III, similar to that observed in column D (Fig. 3.14), the TCE profiles deviated from the pseudo-first-order kinetics with the continuous addition of solution, and the migration of TCE profiles can be divided into two segments at ca. 100 min (5 cm from the influent end). In segment 1, the TCE degradation rate decreased very rapidly and was close to zero at 502 PV. However, there is a transition zone between ca. 50 min to ca. 100 min in segment 1. In this transition zone, iron was not fully inactive toward TCE degradation at the end of the experiment (8% of TCE degraded at 517 PV) (Fig. 3.17), whereas in column D, the iron lost its reactivity totally at the same location and the same time (Fig. 3.14). Using data points obtained from segment 2, the half-lives of TCE degradation were between 30 ~ 50 min. The TCE degradation rate beyond the region with Fe(III)/Cr(III) formation in column E is similar to that in column C (half-lives between 30 ~ 80 min).. Therefore, Cr(VI) appears to have had little or no effect on TCE degradation in segment 2.

Similar to column D, Cr(VI) reduction is more rapid than TCE degradation in both segments 1 and 2 (Fig. 3.17). After 500 PV, TCE degradation was fully inhibited after 50 min of residence time (at the 2nd sampling port, 2.5 cm from the influent end) and 30 % Cr(VI) was removed at the same location, only 10 % of TCE was degraded after 100 min of residence time (at the 3rd sampling port, 5 cm from the influent end) and no Cr(VI) was detected at the same location (Fig. 3.17).

The addition of CaCO₃ enhanced both TCE and Cr(VI) reduction. The half-life of TCE degradation decreased from more than 3 hr at the end of Phase II to 30 min at 71 PV in Phase III (Fig. 3.17), which is similar to that observed in column C. The Cr(VI) reduction rate in column E is similar to that in column B and is faster than that in column D. At the end of the experiment, no Cr(VI) was detected after 100 min of residence time (5 cm from the influent end) in columns B and E (Fig. 3.6 and Fig. 3.17), whereas 35 % Cr(VI) was detected at the same location in column D (Fig. 3.14). The similar Cr(VI) reduction rate in both columns B and E suggests that TCE did not affect Cr(VI) reduction significantly, and Cr(VI) reduction is more favourable than TCE degradation.

3.6.2 Alkalinity Profiles, pH, Changes of Corrosion Potential, H₂ Generation Rate and Hydraulic Conductivity

Fig. 3.18 shows alkalinity profiles for column E. The migration of alkalinity was similar to that of columns B and C as discussed in detail in section 3.3.2.

The pH and corrosion potentials measured at Port E and Port I are shown in Fig 3.19. The changes in pH at both Port I and E followed similar trends as in columns B and C during Phase III, i.e., the pH at Port I remained low (6.7 ~7.6), while the pH at Port E decreased from 9 at the earlier time to 7.4 by the end of the experiment. Again, the trend in pH is caused by the buffering effect of carbonate. The reduction of Cr(VI) and TCE, as well as iron corrosion caused the shift of the carbonate-bicarbonate equilibrium, and the accumulation and migration of carbonate minerals towards the effluent end of the column.

At the beginning of Phase III, there was a 20 mV initial corrosion potential drop at Port E (from -490mV to -510mV) within the first 5 pore volumes of solution. The corrosion potential increased over the next 15 pore volumes to -490 mV and stabilized at this value with the continuing addition of solution, up to approximately 200 PV. From ca. 200 PV to ca. 450 PV, the corrosion potential at Port E increased 50 mV (from -490 mV to -440 mV). Even though there is a data gap thereafter, the corrosion potential appears to stabilize at -440 with the continuous addition of solution. Due to the limited measurements at Port I during early times in Phase III, the initial fluctuation in corrosion potential at Port I was not observed, but undoubtedly occurred due to the presence of CaCO₃. The potential at Port I remained at -460 mV up to ca. 250 PV, and gradually increased thereafter to -360 mV at 500 PV, and then stabilized at -360 mV until end of the experiment.

The +50 mV shift in corrosion potential at Port E at later time may relate to the decrease in pH (from 8.7 to 7.5) at the similar pore volumes (Fig. 3.19). A similar phenomenon was observed at Port E of both columns B and C with a smaller scale (+20 mV shift in column B, and +30 mV shift in Column C). Due to the stable pH at Port I in Phase III, the +100 mV shift in corrosion potential should be caused by the formation and accumulation of passive iron oxides and Cr(III) products from Cr(VI) reduction by iron, which resulted in migration of the TCE and Cr(VI) profiles (Fig. 3.17). Similar to the discussion for column B, the relatively low positive value (+100 mV compared to +180 mV and +220 mV in columns A and D) was caused by the offsetting effect of CaCO₃.

As described for column D (section 3.5.2), the much stronger oxidation ability of Cr(VI) than that of TCE towards iron corrosion can be used to explain the more competitive reduction of Cr(VI) than TCE degradation in column E.

The H₂ generation rate in column E in Fig. 3.3 ranged from 0.02 to 0.05, which is similar in magnitude to those of columns B and C. The hydraulic conductivity in column E decreased slightly, with values ranging from 3.9×10^{-5} to 1.8×10^{-5} m/s (Fig. 3.4).

3.6.3 Changes in Oxide Films on Iron Surface

Raman spectroscopic measurements were conducted when 520 PV of Cr(VI) + TCE + CaCO₃ had passed through column E. Fig. 3.19 a (taken from the bottom of the column, near Port I) and b (15 cm from influent end, near Port E) are examples of Raman spectra of the iron surface from these two sampling ports.

Besides carbon bands (1327, 1580~1585, 1612~1620 cm⁻¹), both Free CO₃²⁻ (at band 1068 cm⁻¹) and aragonite (at bands 152, 203 and 1086 cm⁻¹ in spectrum “a”, at bands 153, 207, 704 and 1086 cm⁻¹ in spectrum “b”), were detected on spectra from Ports I and E.

Fe_nCr_mO₄ spinel (673 cm⁻¹) was detected in spectrum “a”, and magnetite (670 cm⁻¹) was detected in spectrum “b”. Goethite (at 299 and 394 cm⁻¹) was detected at spectrum “a” but was not found in spectrum “b”.

Table 3.6 summarizes species detected from the bottom of the column and the port 15 cm from the influent end. Goethite was detected more frequently near Port I than near Port E and abundant amount of aragonite was detected from both Port I and Port E. Raman spectroscopic results together with the corrosion potential measurements indicate that in Segment 1, iron surface was passivated by passive iron oxide and carbonate mineral precipitates, resulting in the migrations of both TCE and Cr(VI) profiles; in Segment 2, the migration in TCE profiles was caused by iron passivation from the precipitation of the secondary carbonate minerals.

Table 3.6 Raman spectroscopic analysis of surface composition on iron grains taken from Column E

Column E (10 mg/L Cr(VI) + 300 mg/L CaCO ₃ + 5 mg/L TCE)						
sample information	Aragonite	α-FeOOH	Fe ₃ O ₄	Fe _n Cr _m O ₄ spinel	Free CO ₃ ²⁻	carbon graphite carbides
Port I (10 spots studied)	6	8	8	3	1	10
Port E (10 spots studied)	8	2	6	0	6	10

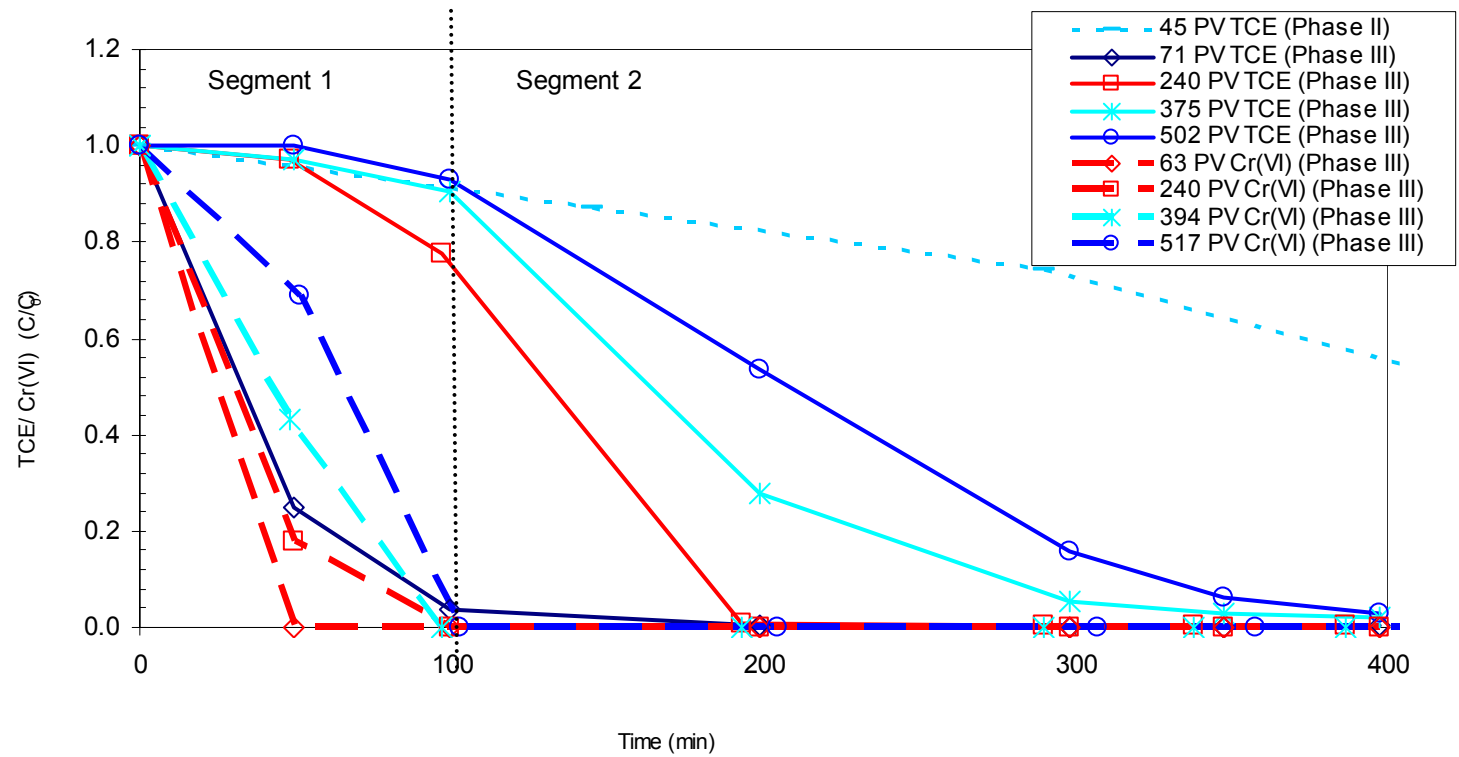


Figure 3.17 TCE and Cr(VI) profiles obtained from column E

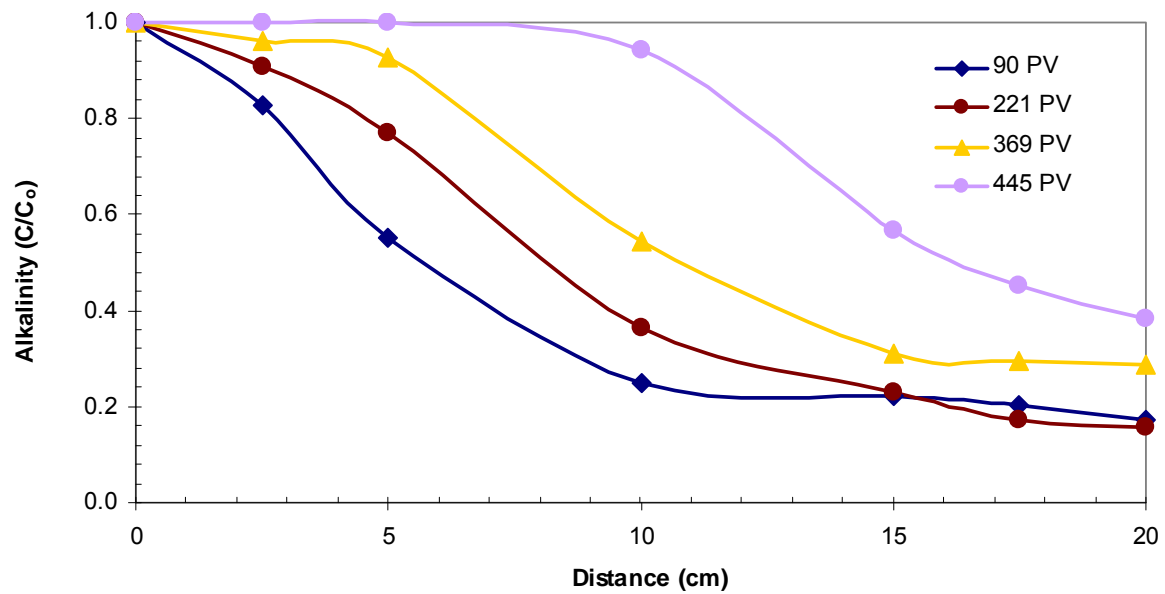


Figure 3.18 Alkalinity profiles from Column E.

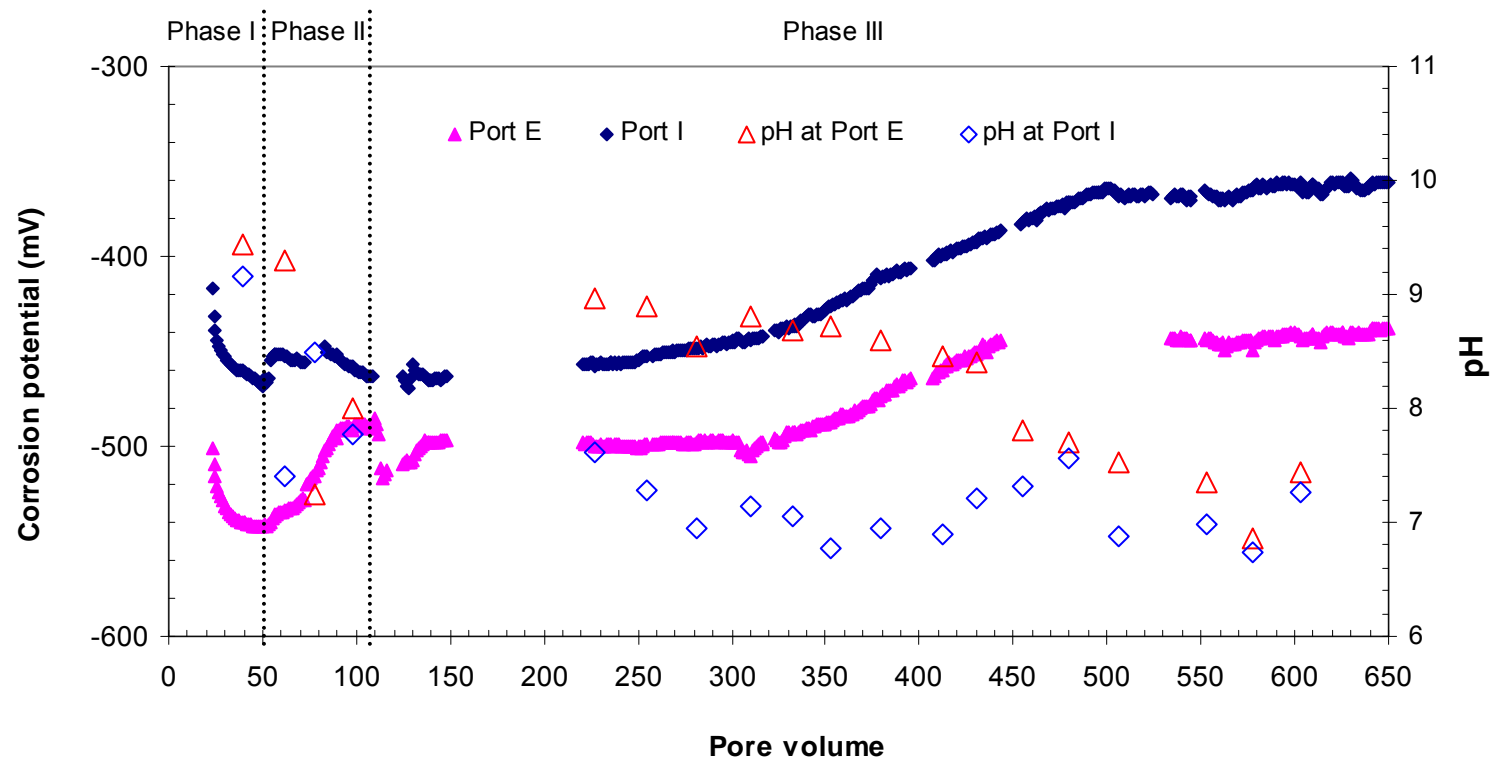


Figure 3.19 Changes of corrosion potentials and pH in column E

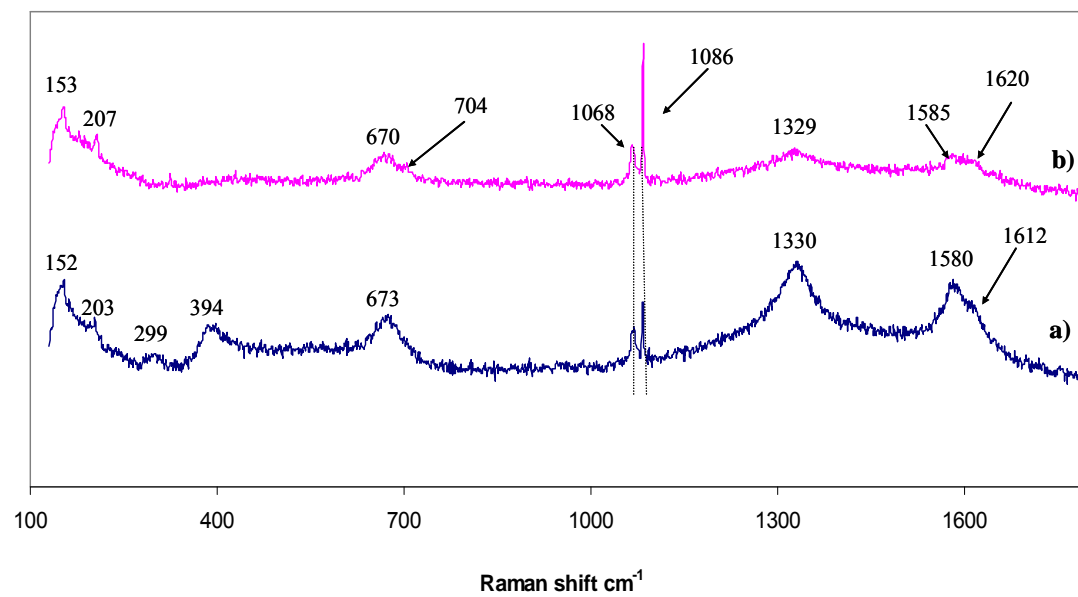


Figure 3.20 Spectra of iron surfaces at the bottom port (a) and the port 15 cm (b) from the influent end in column E

3.7 Discussion for the Five Columns

Table 3.7 summarizes the experimental results obtained from all five columns, including the reaction kinetics of TCE and Cr(VI) reduction, the shifts in corrosion potential measured at Port I, iron passivating oxides and secondary carbonate precipitates measured from Raman spectroscopy, the rate of measured hydrogen production, the trend in hydraulic conductivity, the migration in alkalinity profiles and measured pH values. By comparing the experimental results for the five columns, the effects of Cr(VI) and dissolved CaCO₃ on the iron reactivity towards TCE and Cr(VI) reduction are discussed below.

3.7.1 Presence of Cr(VI)

Similar results were measured for each of the four columns containing Cr(VI) in the influent (columns A, B, D and E). The progressive migration of Cr(VI) and TCE profiles were observed with the continuous addition of solutions over the period of Phase III; however, Cr(VI) was fully removed before reaching the port 10 cm from the influent end (Figs. 3.1, 3.6, 3.14 and 3.17). In the meantime, corrosion potential at Port I progressively increased with a large shift in columns without CaCO₃ (columns A and D) (Figs. 3.2 and 3.15) and a medium shift in the columns receiving CaCO₃ (columns B and E) (Figs. 3.8 and 3.19). The pH at Port I and Port E in the two columns without CaCO₃ (column A and D) increased sharply from 6.6 ~ 7.8 by the end of Phase II to over 10 at early time in Phase III, and remained high (9.5 ~ 10) until the end of the experiment (Figs. 3.2 and 3.15). Raman measurements towards the end of the experiment showed abundant non-conducting high valent passivating iron oxides, such as hematite and goethite, at Port I, but seldom at Port E (Figs. 3.5, 3.9, 3.16 and 3.20). Cr³⁺ species, such as Fe_nCr_mO₄, Cr₂O₃ and CrOOH, were also detected occasionally at Port I. The similar results observed for the columns containing Cr(VI) indicate that granular iron reduces Cr(VI) to insoluble Cr(III) products, as iron is oxidized to high valent iron oxides. The formation and accumulation of Fe(III) and Cr(III) oxides on the iron surface passivated the iron material gradually and resulted in the progressive migration of Cr(VI) as well as TCE degradation profiles.

When TCE and Cr(VI) exist as co-contaminants, the Cr(VI) reduction is much more rapide than TCE degradation (Figs. 3.14 and 3.17). The two segments in the migration profiles of TCE are identified: the first segment at the lower portion of the column, where the iron was still active towards Cr(VI) reduction but inactive towards TCE degradation, and the second segment where Cr(VI) was

fully removed and the TCE degradation continued to follow pseudo-first-order kinetics. It is expected that the first segment of TCE profiles would extend gradually with the migration of Cr(VI) profiles over time.

3.7.2 Presence of CaCO₃

The presence of CaCO₃ enhanced TCE degradation and Cr(VI) reduction. For columns receiving CaCO₃ (columns C and E), the half-lives of TCE degradation decreased significantly from 2.4 ~ 3 hr at the end of Phase II to 30 min at the first sampling event in Phase III (Figs. 3.10 and 3.17), whereas in the absence of CaCO₃ (column D), the half-life of TCE degradation remained unchanged during the transition between Phase II to early time in Phase III (Fig. 3.14). For columns without CaCO₃ (columns A and D), Cr(VI) profiles migrated up to 10 cm along the columns (Figs. 3.1 and 3.14), while for columns containing CaCO₃ (columns B and E), Cr(VI) profiles migrated up to 5 cm along the columns (Figs. 3.6 and 3.17). There was a transition zone in segment 1 for column E receiving CaCO₃, while there was no such zone at the same location and same time for column D without CaCO₃.

The enhancing effect of CaCO₃ may be a consequence of the changes in pH and alkalinity profiles of the three columns containing CaCO₃ (columns B, C and E). With the addition of CaCO₃ in Phase III, pH at Port I remained low while pH at Port E was high at the beginning and decreased and approached the values at Port I at the end of the experiment; alkalinity profiles migrated from close to the influent end at early time towards the effluent end at late time. Together, the measured pH and alkalinity results indicate that, initially, the addition of CaCO₃ buffered the high pH caused by Cr(VI) reduction and iron corrosion, and thus, the reduction reactions were enhanced significantly. The one order of magnitude higher hydrogen production rate observed in the three columns containing CaCO₃ (columns B, C and E) than in the columns without CaCO₃ (columns A and D) is the evidence of the enhanced corrosion rate. In the meantime, the low pH offsets the increase in corrosion potential from the formation of Fe(III)/Cr(III) products, and the final positive shifts in corrosion potential in columns B (Cr(VI) + CaCO₃, +70 mV) and E (Cr(VI) + TCE + CaCO₃, +100 mV) are smaller than those in column A (Cr(VI), +180 mV) and D (Cr(VI) + TCE, +220 mV).

On the other hand, the high pH due to Cr(VI) reduction and iron corrosion shifted the carbonate-bicarbonate equilibrium and resulted in the precipitation of secondary carbonate minerals, as evidenced by Raman analysis, on iron surfaces from the three columns receiving CaCO₃ (columns B, C and E). The precipitation and accumulation of the secondary minerals on the iron surface

decreased iron reactivity gradually, as indicated from the progressive migration of TCE profiles in column C and of second segment TCE profiles in column E. For Cr(VI) profiles, it is very difficult to identify the cause of iron passivation by Fe(III)/Cr(III) oxides, or by the precipitation of the secondary carbonate minerals, or by both. The detection of aragonite from Raman spectroscopy for columns B, C and E, and the absence of iron oxides, together with the slight shift (+20 mV) in corrosion potential at Port I in column C indicates that carbonate mineral does not cause increase in corrosion potential.

The enhancement of iron reactivity by 300 mg/L CaCO₃ is significant. Even through TCE profiles migrated in Phase III, TCE was remediated efficiently at the effluent in columns C and E (over 90%) compared to that in column D (less 50%) by the end of the experiment. Over the period of Phase III, there was a slight decrease in hydraulic conductivity observed from the three columns containing CaCO₃. However, the decrease is so small that there was no measurable effect on the flow rate of the three columns.

Table 3.7 Summary on the experimental results for the five columns in Phase III.

Column Information	Kinetics		Corrosion potential shift (Port I)	Raman Analyses		Hydrogen production rate	Hydraulic conductivity	Migration in alkalinity profiles	pH	
	TCE	Cr(VI)		Passive oxides	Secondary carbonate precipitates				Port I	Port E
Col. A (Cr(VI))		Migration up to 10 cm	+180 mV	Yes	No	Low	Stable	No	H	H
Col. B (Cr(VI) + CaCO ₃)		Migration up to 5 cm	+ 70 mV	Yes	Yes	High	↓	Yes	L	↓
Col. C (TCE + CaCO ₃)	pseudo-first -order Half-lives: 30 min → 2 hr		+20 mV	No	Yes	High	↓	Yes	L	↓
Col. D (TCE + Cr(VI))	Seg. 1, passivated, no transition zone Seg. 2, pseudo-first -order	Migration up to 10 cm	+220 mV	Yes	No	Low	Stable	No	H	H
Col E. (TCE + Cr(VI) + CaCO ₃)	Seg. 1, passivated, transition zone Seg. 2, pseudo-first -order	Migration up to 5 cm	+ 100 mV	Yes	Yes	High	↓	Yes	L	↓

Chapter 4 Numerical Simulation

4.1 The Numerical Model MIN3P

4.1.1 General Description

The numerical model MIN3P (Mayer et al., 2002) was developed to simulate multi-component reactive transport in variably-saturated porous media in one, two or three spatial dimensions. The model formulation is based on the global implicit solution approach, which enforces a global mass balance between solid, surface, dissolved and gaseous species and thus facilitates the investigation of the interactions of reaction and transport processes between different phases. Geochemical reactions considered include hydrolysis, complexation, oxidation-reduction, ion exchange, mineral dissolution-precipitation and gas exchange. The general kinetic formulation for intra-aqueous and dissolution-precipitation reactions in MIN3P is scaled by the reactive surface area, which defines the mineral surface that is actively participating in reactions. More details about the model can be found in Mayer et al. (2002).

4.1.2 Modification of Kinetic Expressions in MIN3P

A previous modeling study using MIN3P predicted predominant precipitation of secondary minerals in the first 10 cm of an iron PRB installed at Elizabeth City, NC, over a time period of 240 days (Mayer et al., 2001). The simulation used a two-thirds power relationship for updating reactive surface area, and did not consider the decreasing reactivity of iron due to precipitation of secondary minerals, subsequently observed in this and other studies (Zhang and Gillham, 2005; Jeen et al, 2006). Based on the laboratory experiments, Jeen (2005) developed an empirical formula relating the decrease in iron reactivity to the accumulation of secondary minerals:

$$S(x, t) = S_0 \exp \left[- \sum_i \alpha_i \varphi_i(x, t) \right] \quad (4.1)$$

where $S(x, t)$ is the reactive surface area of iron at a specific location along the flow path and time ($\text{m}^2 \text{ iron L}^{-1} \text{ bulk}$), S_0 is the initial reactive surface area of iron ($\text{m}^2 \text{ iron L}^{-1} \text{ bulk}$), α_i is the proportionality constant for mineral phase i , and $\varphi_i(x, t)$ is the volume fraction of the mineral phase i

at a specific location and time. The proportionality constant for a particular mineral phase represents the extent to which that mineral phase contributes to the loss in reactivity of iron.

The study of Jeen (2005) used Equation 4.1 to replace the two-thirds power-relationship in MIN3P to account for the reactivity loss of iron due to secondary mineral precipitation, and this reactivity loss was incorporated into the kinetic expressions of MIN3P. The modified model reproduced the column experimental results for the treatment of TCE or Cr(VI) as single contaminant in the presence of dissolved CaCO_3 .

The current study used similar experimental design as that of Jeen (2005). In addition to treating TCE and Cr(VI) as single contaminant, the competition between these two as co-contaminants were also studied (Chapter III). The objective of the study presented in this chapter was to test whether the experimental results from Chapter III can be represented by the modified MIN3P model, and thus to evaluate the applicability of the model to the more complicated system where Cr(VI) co-exists with TCE and CaCO_3 .

4.2 Simulation of the Column Experiments

4.2.1 Input Parameters

One-dimensional discretization was used to represent the columns. The spatial discretization interval was 0.005 m for the 0.2 m-long column, giving a total of 41 grid points. The initial porosity was calculated as described in Section 2.1.1 (Table 2.1) and the average hydraulic conductivity values at early time in Phase III for each column (Fig. 3.4) were used as the initial hydraulic conductivity in the model. The flow system was modelled as a fully-saturated system with a second type boundary (specified flux) at the influent end and first type boundary (specified head) at the effluent end. The average flow rate used in the column experiments was used for the specified flux through the column.

A diffusion coefficient of $1.5 \times 10^{-9} \text{ m}^2/\text{s}$ and longitudinal dispersivity of $9.9 \times 10^{-4} \text{ m}$ (Jeen, 2005) were used for the transport parameters. The measured aqueous concentrations and pH of the source water for each column were used for the influent chemical compositions. The detailed input parameters for each column are summarized in Table 4.1.

4.2.2 Chemical Reactions

For the columns receiving Cr(VI) (Columns A, B, D and E), the Raman spectroscopic analyses indicated that abundant iron oxides, including hematite, goethite and magnetite, formed on the iron surfaces. Some Cr³⁺ products, such as Fe_nCr_mO₄ spinel, Cr₂O₃, and CrOOH were detected occasionally; however, the peaks were either weak, or mingled with peaks of other species. According to the literature (Blowes et al., 1997; Pratt et al., 1997; Blowes et al., 2000), the potential products from Cr(VI) reduction by iron are Fe(III)-Cr(III) (oxy)hydroxides, goethite and hematite. In the simulations of Jeen (2005), for simplicity, Fe(OH)₃ and Cr(OH)₃ were used as representative products of Cr(VI) reduction (reaction 4.2), and only Fe(OH)₃ was considered to contribute to the reactivity loss of iron. In this study, the same approach was used.



For the columns receiving dissolved CaCO₃ (columns B, C and E), aragonite was detected by Raman spectroscopy as the only secondary carbonate mineral. However, besides aragonite, Fe₂(OH)₂CO₃ was detected by XRD in similar geochemical settings in the study of Jeen (2005). Based on the Ca²⁺ measurements, Jeen (2005) indicated that only half of the decline in alkalinity was attributable to aragonite, and Fe₂(OH)₂CO₃ was used to balance the remaining decline in alkalinity. Therefore, in this study, both CaCO₃ and Fe₂(OH)₂CO₃ were considered as the dominant secondary carbonate precipitates.

Aqueous components included were Ca²⁺, Cl⁻, CO₃²⁻, CrO₄²⁻, Cr(OH)²⁺, Fe²⁺, Fe³⁺, H⁺, H₂(aq), TCE, cis-DCE, VC, ethene, and H₂O. A total of 26 aqueous complexes were included and Table 4.2 lists the corresponding complexation reactions and equilibrium constants. The most important chemical reactions in the columns include TCE degradation, Cr(VI) reduction, iron corrosion, and secondary mineral precipitation. The kinetic expressions for each reaction used in the simulation are shown in equations 4.3 through 4.6. Tables 4.3 and 4.4 list the reaction stoichiometries of reduction–corrosion reactions, and secondary mineral formation reactions with corresponding equilibrium constants, respectively.

$$\frac{d[\text{TCE}]}{dt} = -k_{\text{SA-TCE-Fe}^0} \cdot S [\text{TCE}] \quad (4.3)$$

$$\frac{d[\text{Cr(VI)}]}{dt} = -k_{\text{SA-Cr-Fe}^0} \cdot S[\text{Cr(VI)}]^{0.5} [\text{H}^+]^{0.5} \quad (4.4)$$

$$R_{\text{H}_2\text{O-Fe}^0} = -\max \left\{ \left[k_{\text{SA-H}_2\text{O-Fe}^0} \cdot S \left(1 - \frac{\text{IAP}_{\text{H}_2\text{O-Fe}^0}}{K_{\text{H}_2\text{O-Fe}^0}} \right) \right], 0 \right\} \quad (4.5)$$

$$R_i^m = \max \left\{ \left[k_{\text{eff},i} \left[1 - \left(\frac{\text{IAP}_i^m}{K_i^m} \right)^{-1} \right] \right], 0 \right\} \quad (4.6)$$

$k_{\text{SA-TCE-Fe}^0}$ is the rate constant for TCE reduction normalized to iron surface area ($\text{mol m}^{-2} \text{ iron s}^{-1}$), S is the reactive surface area concentration of iron ($\text{m}^2 \text{ iron L}^{-1} \text{ bulk}$), $k_{\text{SA-Cr-Fe}^0}$ is the rate constant of Cr normalized to iron surface area ($\text{L H}_2\text{O m}^{-2} \text{ iron s}^{-1}$), $k_{\text{SA-H}_2\text{O-Fe}^0}$ is the rate constant of iron corrosion normalized to iron surface area ($\text{mol m}^{-2} \text{ iron s}^{-1}$), $k_{\text{eff},i}$ is an effective rate constant for the precipitation of mineral phase i ($\text{mol L}^{-1} \text{ H}_2\text{O s}^{-1}$), IAP is the ion activity product, and K is the equilibrium constant.

The detailed information on obtaining the rate constants of TCE and Cr, iron corrosion rate, the effective rate constants of CaCO_3 (s) and $\text{Fe}_2(\text{OH})_2\text{CO}_3$, and the proportionality constant (α_i of equation 4.1) for each mineral phase is given in Jeen (2005). Table 4.5 lists the fitting parameters for each column used in the simulations as well as those used in the study of Jeen (2005) for comparison. Generally, the fitting parameters from this study are similar to those of Jeen (2005).

4.3 Simulation Results

In the simulations, the constraints for fitting parameters are laboratory measurements of Cr(VI) and/or TCE concentration, pH and alkalinity at different times. Because there are many model parameters operating together, in order to reduce the possibility of non-uniqueness in the set of model parameters, the initial rate constants for TCE and Cr, and iron corrosion were obtained from the experiments in Chapter 3. The effective rate constants for CaCO_3 (s), $\text{Fe}_2(\text{OH})_2\text{CO}_3$, $\text{Fe}(\text{OH})_2$, $\text{Fe}(\text{OH})_3$ and $\text{Cr}(\text{OH})_3$, and the proportionality constants (α_i in equation 4.1) for each mineral phase are the same as those used in the study of Jeen (2005). To acquire the best fits, all the experimental

parameters were adjusted slightly, and all the other parameters were kept close to those of Jeen (2005) (Table 4.5).

The simulation results of the experiments for each column are shown in Fig. 4.1 through Fig. 4.7. Due to the similar flow rate over the period of Phase III, the migration of the chemical profiles at different times are expressed as distance along the column instead of residence time in the column as used in Chapter 3. For columns without CaCO_3 (columns A and D), the simulated Cr(VI), TCE and pH profiles together with experimental data at similar times, the reaction products of Fe(III)/Cr(III), the porosity and the reactive surface area changes with time are shown in each diagram (Fig. 4.1 and Fig. 4.5). For columns with CaCO_3 (columns B, C and E), in addition to the data as in columns A and D, alkalinity and carbonate mineral profiles at different times are also shown (Figs. 4.2 and 4.3, 4.4, Figs. 4.6 and 4.7).

Not unexpectedly, the simulations did not precisely match the laboratory data; however, the simulated profiles for each column generally represent the trends and shapes of the measured profiles very well.

The simulated Cr(VI) profiles for columns A and D, which received no CaCO_3 , match the experimental data very well, indicating migration distance of up to 8 cm from the inlet ends by Day 142 and 140, respectively (Fig. 4.1 (a) and Fig. 4.5 (a)). Cr(VI) profiles in columns B and E, which received 300 mg/L CaCO_3 , are similar, and migrated up to 5 cm from the inlet ends by Day 155 and 146, respectively (Fig. 4.2 (a) and Fig. 4.6 (a)). The presence of dissolved CaCO_3 initially enhanced Cr(VI) reduction, which is consistent with the experimental results of this study, as well as the study of Jeen (2005). The extent to which the Cr profiles migrated was primarily controlled by the precipitation of $\text{Fe}(\text{OH})_3(\text{am})$ (Fig. 4.1 (c), Fig. 4.3 (a), Fig. 4.5 (d) and Fig. 4.7 (a)) and its proportionality constant; 900 for columns A and D, 700 for columns B and E (Table 4.5).

Simulated TCE profiles in columns D and E are similar to the measured data (Fig. 4.5 (b) and Fig. 4.6 (b)). In these two columns, Cr(VI) reduction resulted in the formation of Cr(III)-Fe(III) (oxy)hydroxides, resulting in substantial passivation of the iron material. The rate of TCE degradation was substantially reduced in the highly passivated region. Beyond this region, the degradation was governed by TCE degradation kinetics itself, and was affected both by the enhanced degradation due to HCO_3^- and by passivation due to precipitation of carbonate minerals (CaCO_3 and $\text{Fe}_2(\text{OH})_2\text{CO}_3$). Column C, which received no Cr(VI), showed greater spreading of the TCE profiles over the length of the column, primarily due to precipitation of carbonate minerals (Fig. 4.4 (a)).

Only the pH measured close to Port I and Port E were discussed in Chapter 3; however, the pH values were measured at all the sampling ports, and are shown in Fig. 4.1 through Fig. 4.6 together with the simulated profiles. As indicated, the measured and simulated profiles are similar. The measured and simulated pH profiles in columns A and D are similar (Fig. 4.1 (b) and Fig. 4.5 (c)) because of the dominant effect of the presence of Cr(VI) and precipitation of $\text{Fe}(\text{OH})_3$ and $\text{Cr}(\text{OH})_3$. A sharp increase in pH was advancing further into the column as $\text{Fe}(\text{OH})_3$ was formed on the iron surfaces; however, at the same time, the profiles were becoming progressively less sharp due to the reactivity loss of iron resulting from the formation of $\text{Fe}(\text{OH})_3$. The simulated pH trends in columns B, C and E are similar (Fig. 4.2 (b), Fig. 4.4 (b) and Fig. 4.6 (c)). The increases in pH values were more gradual than those of columns A and D due to carbonate precipitation and high pH buffering capacity of the solution. Similarly, because of carbonate precipitation and its pH control, the trends in the alkalinity profiles in these three columns are similar (Fig. 4.2(c), Fig. 4.4 (c), and Fig. 4.6 (d)).

Because of the low concentrations of Cr(VI) (10 mg/L) for columns A and D, the resulting volume fractions for $\text{Fe}(\text{OH})_3$ and $\text{Cr}(\text{OH})_3$ were quite low (up to 0.035). Thus, the porosity loss due to these minerals was not significant (Fig. 4.1 (e) and Fig. 4.6 (f)); however, the decrease in reactive surface area expressed by equation 4.1, was substantial in the region of $\text{Fe}(\text{OH})_3$ accumulation (Fig. 4.1 (f) and Fig. 4.5 (g)). Because of the high concentrations of CaCO_3 (300 mg/L) for columns B, C and E, the resulting volume fractions of aragonite and $\text{Fe}_2(\text{OH})_2\text{CO}_3$ were high (up to 0.2). Thus, the porosity losses due to these minerals were significant (Fig. 4.3 (c), Fig. 4.4 (f) and Fig. 4.6 (e)). The reactive surface area in columns B and E (Fig. 4.3 (d) and Fig. 4.7 (f)) showed substantial decreases near the influent end and a more subdued decrease beyond that region along the column, which was due to the combined contribution of $\text{Fe}(\text{OH})_3$ and carbonate minerals to the loss in reactivity. On the other hand, the decrease in reactive surface area in column C (Fig. 4.4 (g)) was relatively moderate throughout the column because only the accumulation of carbonate minerals contributed to the loss in reactivity.

4.4 Evaluation of the Model Simulation

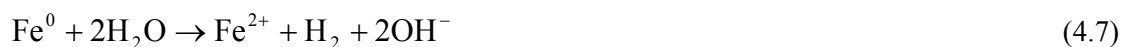
The simulated profiles represent the experimental data, including the migration of TCE and/or Cr(VI), changes in pH and alkalinity relatively well, demonstrating the ability of the model to represent the geochemical evolution within the column. However, there are several issues, including the assumptions and input data of the model, that are subject to some discussion.

Secondary Carbonate Minerals

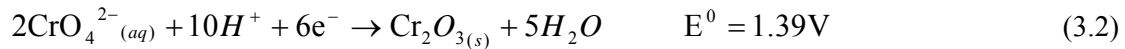
For the columns receiving CaCO_3 , aragonite and $\text{Fe}_2(\text{OH})_2\text{CO}_3$ were the two species selected to represent the secondary carbonate minerals in the model. The sequential removal of alkalinity corresponds to the formation of the two species. The fitted effective rate constants and the proportionality constants for aragonite and $\text{Fe}_2(\text{OH})_2\text{CO}_3$ for the three columns in this study are comparable to those determined in the study of Jeen (2005) (Table 4.5). In Jeen (2005), the proportionality constant for $\text{Fe}_2(\text{OH})_2\text{CO}_3$ is very small, ranging between 2 ~ 5, while in this study it is 0 for all three columns. This means that even though $\text{Fe}_2(\text{OH})_2\text{CO}_3$ formed and accumulated, its contribution to the iron passivation is very small. In other words, even though $\text{Fe}_2(\text{OH})_2\text{CO}_3$ contributes to the changes in column porosity, it is electron conducting and has no effect on the rate of electrons passing through these deposits on the iron surface. In the three columns, the porosity decreased, which is consistent with the slight decrease in measured hydraulic conductivity values (Chapter 3). $\text{Fe}_2(\text{OH})_2\text{CO}_3$ is a relatively newly recognized iron carbonate species in iron PRB settings (Kohn et al., 2005), and thus, its properties are not well known. The simulation results in this study show that the volume fraction of $\text{Fe}_2(\text{OH})_2\text{CO}_3$ was twice that of aragonite at later time at 15 cm along the three columns receiving CaCO_3 . This appears to be inconsistent with the Raman measurements, which only detected CaCO_3 but not $\text{Fe}_2(\text{OH})_2\text{CO}_3$ at Port E. However, the concentrations of Ca^{2+} and Fe^{2+} were not measured in this study, the same assumption as Jeen (2005) was used in this study. Therefore, further research is needed to determine whether this is due to limitations of the Raman analyses on secondary minerals or due to the limitation of the model assumptions.

Fe(III)/Cr(III) products

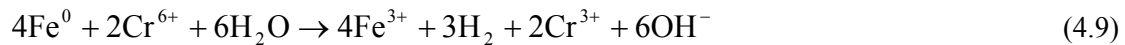
For simplicity, the model uses reaction 4.2 to represent Cr(VI) reduction by granular iron and $\text{Fe}(\text{OH})_3$ and $\text{Cr}(\text{OH})_3$ represent Fe(III)/Cr(III) products. Thus, for columns containing Cr(VI), the simulation results have similar volume fractions of $\text{Fe}(\text{OH})_3$ and $\text{Cr}(\text{OH})_3$. However, from the result of the Raman spectroscopic analysis for the columns containing Cr(VI), much more three valent iron oxides than Cr(III) products were detected (Chapter 3). The Raman measurements are consistent with the experimental conditions, i.e. only small amounts of Cr(VI) were supplied compared to the abundance of granular iron in the column. In addition to reaction with Cr(VI), iron also reacted with H_2O and/or TCE, forming Fe^{2+} , by the reaction 4.7:



Furthermore, comparing the half reduction potentials of oxidation of ferrous iron (reaction 4.8) and Cr(VI) reduction (reaction 3.2), the redox reaction between Cr(VI) and Fe^{2+} is thermodynamically favorable:



Previous research indicates that Cr(VI) was reduced by mineral phases containing significant amounts of ferrous iron, such as magnetite, biotite and iron sulfides (Blowes, et al., Erdem et al, 2004). Therefore, Fe^{2+} was involved in Cr(VI) reduction, then an overall Cr(VI) reduction by Fe^0 and Fe^{2+} can be expressed as:



Reaction 4.9 indicates that the molar ratio of Fe(III) products to Cr(III) products is 2:1. This suggests that reaction 4.2 may not be an accurate representation for Cr(VI) reduction by granular iron in the model.

Reactive Surface Area

As discussed in Chapter 3, there are two mechanisms causing the decrease in the iron reactivity, the positive shift in corrosion potential caused by passive Fe(III)/Cr(III) oxides, and the decreased iron reactive surface area due to the secondary carbonate precipitates. In the simulation, “reactive surface area” was used to express the reactivity of iron and thus provides a quantitative basis for representing decreased reactivity of iron. “Reactive surface area” was mainly determined by the formation and migration of carbonate minerals and/or Fe(III)Cr(III) products and their proportionality constants. For example, the up to 4 orders of magnitude decrease in reactive surface area in columns containing Cr(VI) is determined by the high proportionality constant (700 ~ 900) of $Fe(OH)_3(am)$. In the model, the empirical formula 4.1 representing the decrease in iron reactivity with the accumulation of secondary minerals was developed based on carbonate mineral results, and the precipitation of carbonate minerals decreases iron surface area and in turn decreases the iron reactivity. However, the passivation of iron by passive oxides causes an increase in corrosion

potential, so the “reactive surface area” concept may not be suitable physical representation of the passivation process. Thus, as currently formulated, the relationship between precipitates and loss of the iron reactivity is largely empirical. Further work would be required to derive a mathematically-based relationship.

Representing the Rate Changes of Iron Reactions

In the experiment, the addition of CaCO_3 (Phase III) enhanced TCE degradation rate relative to Phase II. However, the model can only have one fixed initial rate for corrosion, TCE degradation or Cr(VI) reduction, and iron passivation starts from the initial rates. In the groundwater, CaCO_3 concentration may change with time, which means that its enhancement to an iron PRB changes with time. Thus, this potential limitation requires further investigation.

4.5 Application of the Model: the Long-Term Performance of an Iron PRB When TCE Co-exists with Cr(VI) in the Presence of CaCO_3

Though there are potential limitations in the model, it provided reasonable representation of the geochemical evolution of the columns receiving TCE and Cr(VI) as co-contaminants, and thus was used to predict the long-term performance of an iron PRB in a hypothetical field scenario where TCE co-exists with Cr(VI) in the presence of CaCO_3 .

The performance of a 40 cm-thick iron PRB with a groundwater composition of 300 mg/L CaCO_3 and velocity of 10 cm/day was simulated as an example (Fig. 4.8). The groundwater concentrations for TCE and Cr(VI) were 5 and 10 mg/L, respectively. The physical and mineralogical parameters used for the simulation, along with the fitting parameters, were taken from column E (see Table 4.1 and Table 4.5).

As discussed in section 4.3, the reactivity of the iron treating Cr(VI) was affected primarily by the accumulation of $\text{Fe}(\text{OH})_3$ rather than by carbonate precipitation. Therefore, Cr(VI) profiles migrated continuously and advanced up to 39 cm from the influent after 30 years of operation (Fig. 4.8 (a)). However, Cr(VI) was still completely treated within the barrier after 30 years. On the other hand, the treatment for TCE was affected by $\text{Fe}(\text{III})/\text{Cr}(\text{III})$ and secondary carbonate precipitates. Thus, TCE profiles migrated much faster than Cr(VI) profiles and only 80% of the influent TCE was treated after 20 years and 10% after 30 years (Fig. 4.8 (b)). In Fig. 4.8 (c), the total carbonate volume fraction, as a sum of the volume fractions of aragonite and $\text{Fe}_2(\text{OH})_2\text{CO}_3$ accumulated over time and reached 0.45 after 30 years. The loss in porosity increased with the precipitation of carbonate minerals, and the porosity was 35 % of the initial value after 30 years (Fig 4.8 (d)).

In summary, in this example, Cr(VI) was completely treated over a period of 30 years, but TCE breakthrough occurred before 20 years. Substantial porosity was lost due to the accumulation of carbonate precipitates. It should be noted that the simulation results were based on the simplified laboratory results. The composition of groundwater is generally more complicated, including a range of dissolved constituents; nevertheless, the findings of this hypothetical simulation provide insights concerning potential problems and design options. Due to the adverse effects of Cr(VI) and carbonate on TCE degradation kinetics, a thicker wall or a higher porosity material are options that could be considered. Further more, having the knowledge that the iron PRB has the potential to fail after about 20 years provides useful information for conducting more relative cost analyses.

Table 4.1 Input parameters used in the simulations.

Parameter	Column				
	A	B	C	D	E
Porosity	0.62	0.51	0.57	0.60	0.61
Fe ⁰ volume Fraction	0.38	0.49	0.43	0.40	0.39
Hydraulic conductivity (m/s)	3.25×10^{-4}	1.64×10^{-5}	2.40×10^{-4}	4.45×10^{-5}	2.63×10^{-6}
Diffusion coefficient (m ² /s)	1.5×10^{-9}				
Longitudinal dispersivity (m)	9.9×10^{-4}				
Running time (Day)	142	155	140	141	146
Flow rate (m/s)	5.12×10^{-6}	5.10×10^{-6}	5.35×10^{-6}	5.38×10^{-6}	5.06×10^{-6}
pH	6.8	7.0	6.7	6.7	7
Ca ²⁺ (mol/L)		3.0×10^{-3}	3.0×10^{-3}		3.0×10^{-3}
CO ₃ Total (mol/L)		7.5×10^{-3}	7.5×10^{-3}		7.5×10^{-3}
TCE (mol/L)			3.8×10^{-5}	3.8×10^{-5}	3.8×10^{-5}
Cr(VI) (mol/L)	1.92×10^{-4}	1.92×10^{-4}		1.92×10^{-4}	1.92×10^{-4}

Table 4.2 Complexation reactions and equilibrium constants.

Reaction	Log K
(1) $\text{OH}^- \Leftrightarrow \text{H}_2\text{O} - \text{H}^+$	-13.9980
(2) $\text{CaOH}^+ \Leftrightarrow \text{Ca}^{2+} + \text{H}_2\text{O} - \text{H}^+$	-12.7800
(3) $\text{CaHCO}_3^+ \Leftrightarrow \text{Ca}^{2+} + \text{CO}_3^{2-} + \text{H}^+$	11.4400
(4) $\text{CaCO}_3(\text{aq}) \Leftrightarrow \text{Ca}^{2+} + \text{CO}_3^{2-}$	3.2200
(5) $\text{FeOH}^+ \Leftrightarrow \text{Fe}^{2+} + \text{H}_2\text{O} - \text{H}^+$	-9.5000
(6) $\text{Fe}(\text{OH})_2(\text{aq}) \Leftrightarrow \text{Fe}^{2+} + 2\text{H}_2\text{O} - 2\text{H}^+$	-20.5700
(7) $\text{Fe}(\text{OH})_3^- \Leftrightarrow \text{Fe}^{2+} + 3\text{H}_2\text{O} - 3\text{H}^+$	-31.0000
(8) $\text{FeHCO}_3^+ \Leftrightarrow \text{Fe}^{2+} + \text{CO}_3^{2-} + \text{H}^+$	12.3300
(9) $\text{FeCO}_3(\text{aq}) \Leftrightarrow \text{Fe}^{2+} + \text{CO}_3^{2-}$	4.3800
(10) $\text{FeCl}^+ \Leftrightarrow \text{Fe}^{2+} + \text{Cl}^-$	0.1400
(11) $\text{FeOH}^{2+} \Leftrightarrow \text{Fe}^{3+} + \text{H}_2\text{O} - \text{H}^+$	-2.1900
(12) $\text{Fe}(\text{OH})_2^+ \Leftrightarrow \text{Fe}^{3+} + 2\text{H}_2\text{O} - 2\text{H}^+$	-5.6700
(13) $\text{FeOH}_3(\text{aq}) \Leftrightarrow \text{Fe}^{3+} + 3\text{H}_2\text{O} - 3\text{H}^+$	-12.5600
(14) $\text{Fe}(\text{OH})_4^- \Leftrightarrow \text{Fe}^{3+} + 4\text{H}_2\text{O} - 4\text{H}^+$	-21.6000
(15) $\text{Fe}_2(\text{OH})_2^{4+} \Leftrightarrow 2\text{Fe}^{3+} + 2\text{H}_2\text{O} - 2\text{H}^+$	-2.9500
(16) $\text{Fe}_3(\text{OH})_4^{5+} \Leftrightarrow 3\text{Fe}^{3+} + 4\text{H}_2\text{O} - 4\text{H}^+$	-6.3000
(17) $\text{HCO}_3^- \Leftrightarrow \text{H}^+ + \text{CO}_3^{2-}$	10.3300
(18) $\text{H}_2\text{CO}_3(\text{aq}) \Leftrightarrow 2\text{H}^+ + \text{CO}_3^{2-}$	16.6810
(19) $\text{Cr}^{3+} \Leftrightarrow \text{Cr}(\text{OH})_2^+ + 2\text{H}^+ - 2\text{H}_2\text{O}$	9.6200
(20) $\text{Cr}(\text{OH})^{2+} \Leftrightarrow \text{Cr}(\text{OH})_2^+ + \text{H}^+ - \text{H}_2\text{O}$	5.6200
(21) $\text{Cr}(\text{OH})_3(\text{aq}) \Leftrightarrow \text{Cr}(\text{OH})_2^+ - \text{H}^+ + \text{H}_2\text{O}$	-7.1300
(22) $\text{Cr}(\text{OH})_4^- \Leftrightarrow \text{Cr}(\text{OH})_2^+ - 2\text{H}^+ + 2\text{H}_2\text{O}$	-18.1500
(23) $\text{CrO}_2^- \Leftrightarrow \text{Cr}(\text{OH})_2^+ - 2\text{H}^+$	-17.7456
(24) $\text{HCrO}_4^- \Leftrightarrow \text{CrO}_4^{2-} + \text{H}^+$	6.5089
(25) $\text{H}_2\text{CrO}_4(\text{aq}) \Leftrightarrow \text{CrO}_4^{2-} + 2\text{H}^+$	5.6513
(26) $\text{Cr}_2\text{O}_7^{2-} \Leftrightarrow 2\text{CrO}_4^{2-} + 2\text{H}^+ - \text{H}_2\text{O}$	14.5571

Table 4.3 Reaction stoichiometries of reduction-corrosion reactions.

TCE degradation	$\text{Fe}^0(\text{s}) + 0.3521 \text{C}_2\text{HCl}_3 + \text{H}^+ \rightarrow$ $\text{Fe}^{2+} + 0.0281 \text{C}_2\text{H}_2\text{Cl}_2 + 0.3239 \text{C}_2\text{H}_4 + \text{Cl}^-$
Cr(VI) reduction	$\text{Fe}^0(\text{s}) + \text{CrO}_4^{2-} + 6 \text{H}^+ \rightarrow \text{Fe}^{3+} + \text{Cr}(\text{OH})_2^+ + 2\text{H}_2\text{O}$
Iron corrosion	$\text{Fe}^0(\text{s}) + 2\text{H}_2\text{O} \rightarrow \text{Fe}^{2+} + \text{H}_2(\text{aq}) + 2\text{OH}^-$

Table 4.4 Mineral dissolution-precipitation reactions and equilibrium constants.

	Reaction	log K
$\text{CaCO}_3(\text{s})(\text{aragonite})$	$\Leftrightarrow \text{Ca}^{2+} + \text{CO}_3^{2-}$	8.360
$\text{Fe}_2(\text{OH})_2\text{CO}_3(\text{s})$	$\Leftrightarrow 2\text{Fe}^{2+} + \text{CO}_3^{2-} + 2\text{H}_2\text{O} - 2\text{H}^+$	0.075
$\text{Fe}(\text{OH})_2(\text{am})$	$\Leftrightarrow \text{Fe}^{2+} + 2\text{H}_2\text{O} - 2\text{H}^+$	-13.905
$\text{Fe}(\text{OH})_3(\text{am})$	$\Leftrightarrow \text{Fe}^{3+} + 3\text{H}_2\text{O} - 3\text{H}^+$	-4.891
$\text{Cr}(\text{OH})_3(\text{am})$	$\Leftrightarrow \text{Cr}(\text{OH})_2^+ + \text{H}_2\text{O} - \text{H}^+$	0.750

Table 4.5 Fitting parameters for each column.

Parameter		Column					Parameter ranges from Jeen (2005)
		A	B	C	D	E	
$\log k_{SA-H_2O-Fe^0}$ (mol m ⁻² iron s ⁻¹)		-10.4	-9.5	-9.6	-10.2	-9.6	-10.4 ~ -9.5
$\log k_{SA-Cr-Fe^0}$ (L H ₂ O m ⁻² iron s ⁻¹)		-3.1	-3.3	NA	-3.1	-3.2	-3.6 ~ -3.4
$\log k_{SA-TCE-Fe^0}$ (L H ₂ O m ⁻² iron s ⁻¹)		NA	NA	-6.1	-7.5	-6.3	-7.1 ~ -6.8
$\log k_{eff}$ (mol L ⁻¹ H ₂ O s ⁻¹)	CaCO ₃ (s) (aragonite)	NA	-7.0	-7.0	NA		-7.4 ~ -6.7
	Fe ₂ (OH) ₂ CO ₃ (s)	NA	-8.9	-8.9	NA		-10.9 ~ -8.4
	Fe(OH) ₂ (am)	-8.7	-8.7	-8.7	-8.7		-8.7
	Fe(OH) ₃ (am)	-8.7	-8.7	-8.7	-8.7		-8.7
	Cr(OH) ₃ (am)	-9.7	-9.7	-9.7	-9.7		-9.7
a_1 (proportionality constant for CaCO ₃ (s))		NA	25	75	NA	45	45 ~ 85
a_2 (proportionality constant for Fe ₂ (OH) ₂ CO ₃ (s))		NA	0	0	NA	0	2 ~ 5
b_1 (proportionality constant for Fe(OH) ₃ (am))		900	700	NA	900	700	700~900

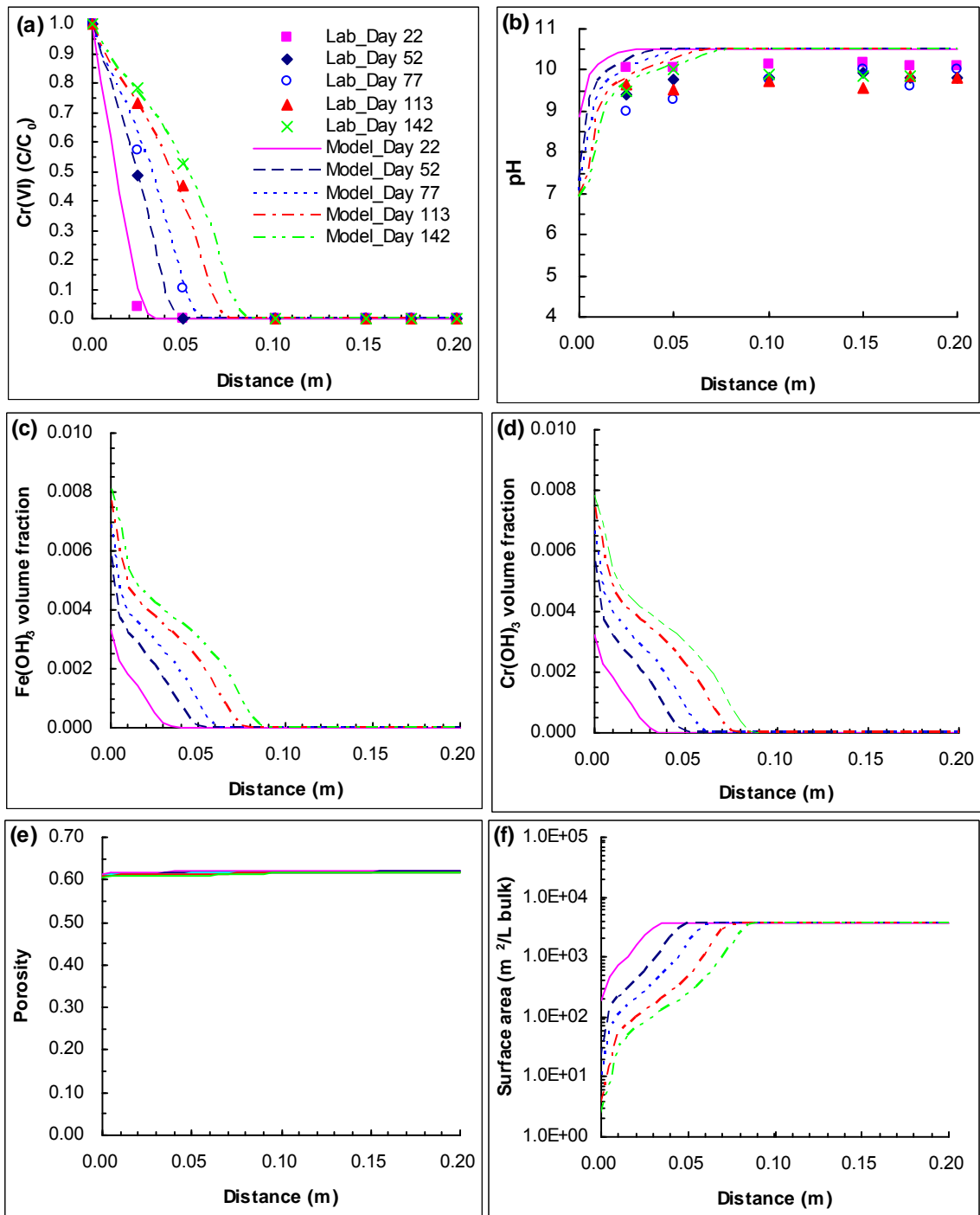


Figure 4.1 Laboratory and simulation profiles for column A: (a) Cr(VI), (b) pH, (c) Fe(OH)₃(am) volume fraction, (d) Cr(OH)₃(am) volume fraction, (e) porosity, and (f) reactive surface area.

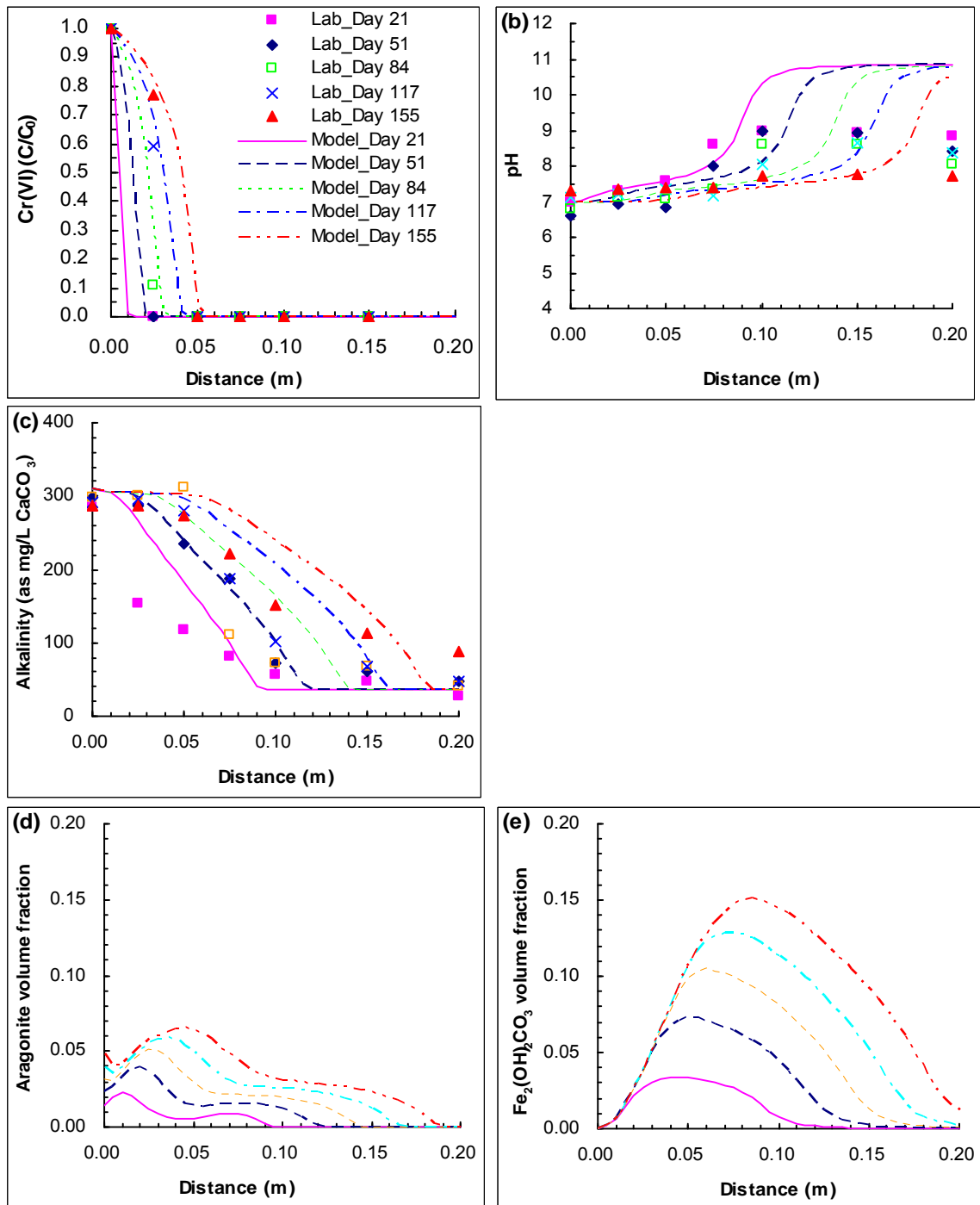


Figure 4.2 Laboratory and simulation profiles for column B: (a) Cr(VI), (b) pH, (c) Alkalinity, (d) aragonite volume fraction, (e) Fe₂(OH)₂CO₃ volume fraction.

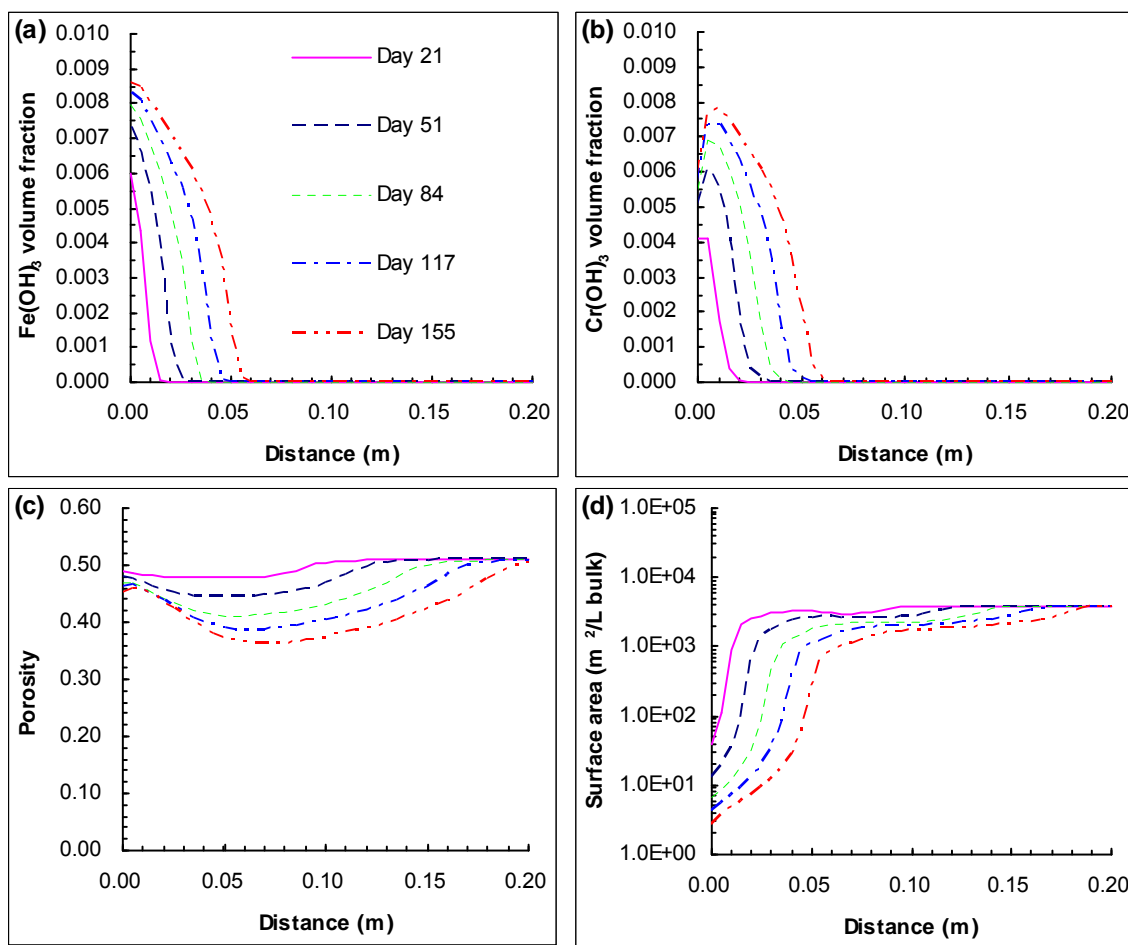


Figure 4.3 Simulated profiles for column B: (a) Fe(OH)₃(am) volume fraction, (b) Cr(OH)₃(am) volume fraction, (c) porosity, and (d) reactive surface area.

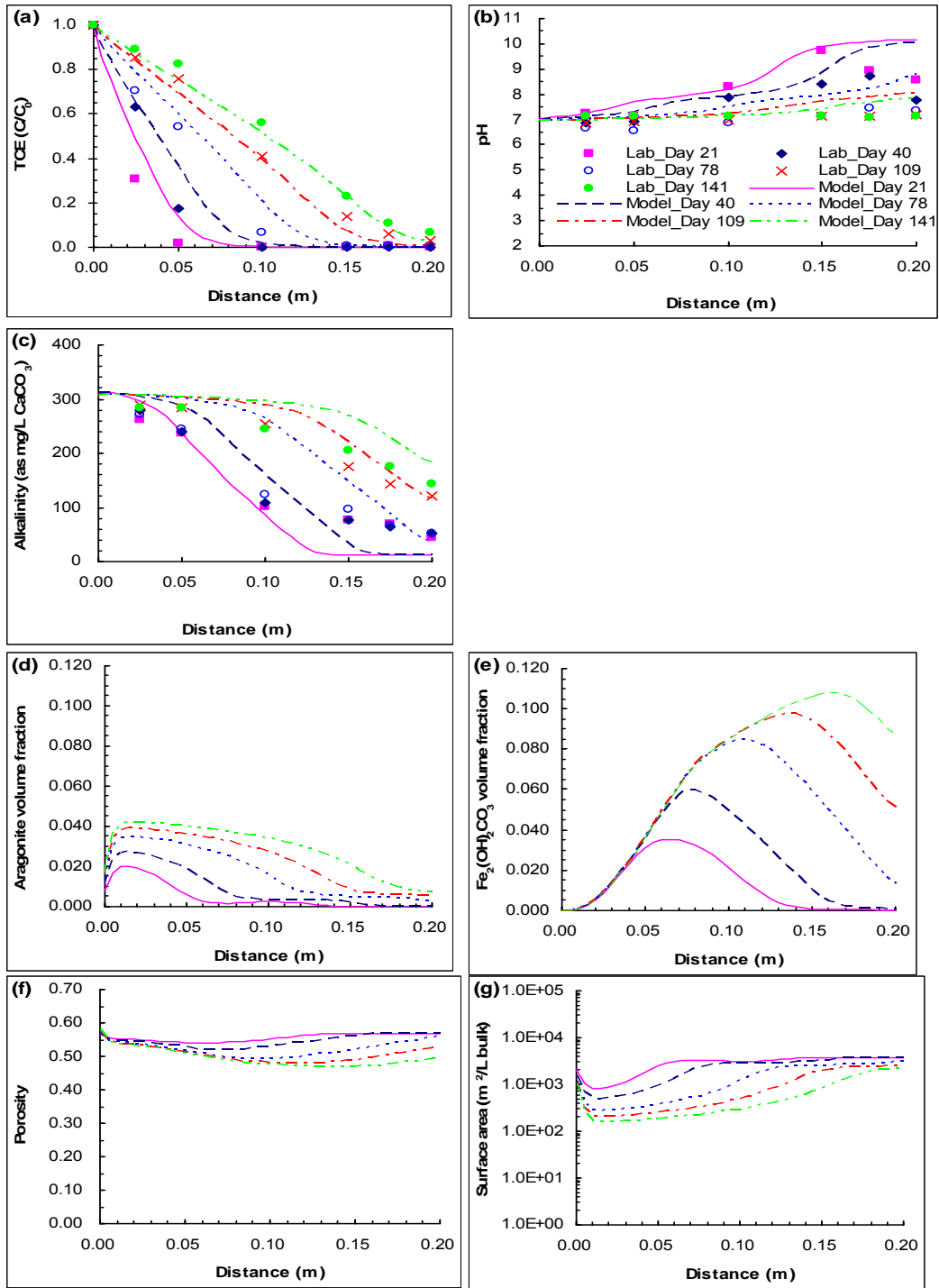


Figure 4.4 Laboratory and simulated profiles for column C: (a) TCE, (b) pH, and (c) alkalinity, (d) aragonite volume fraction, (e) $\text{Fe}_2(\text{OH})_2\text{CO}_3$ volume fraction (f) porosity, and (g) reactive surface area.

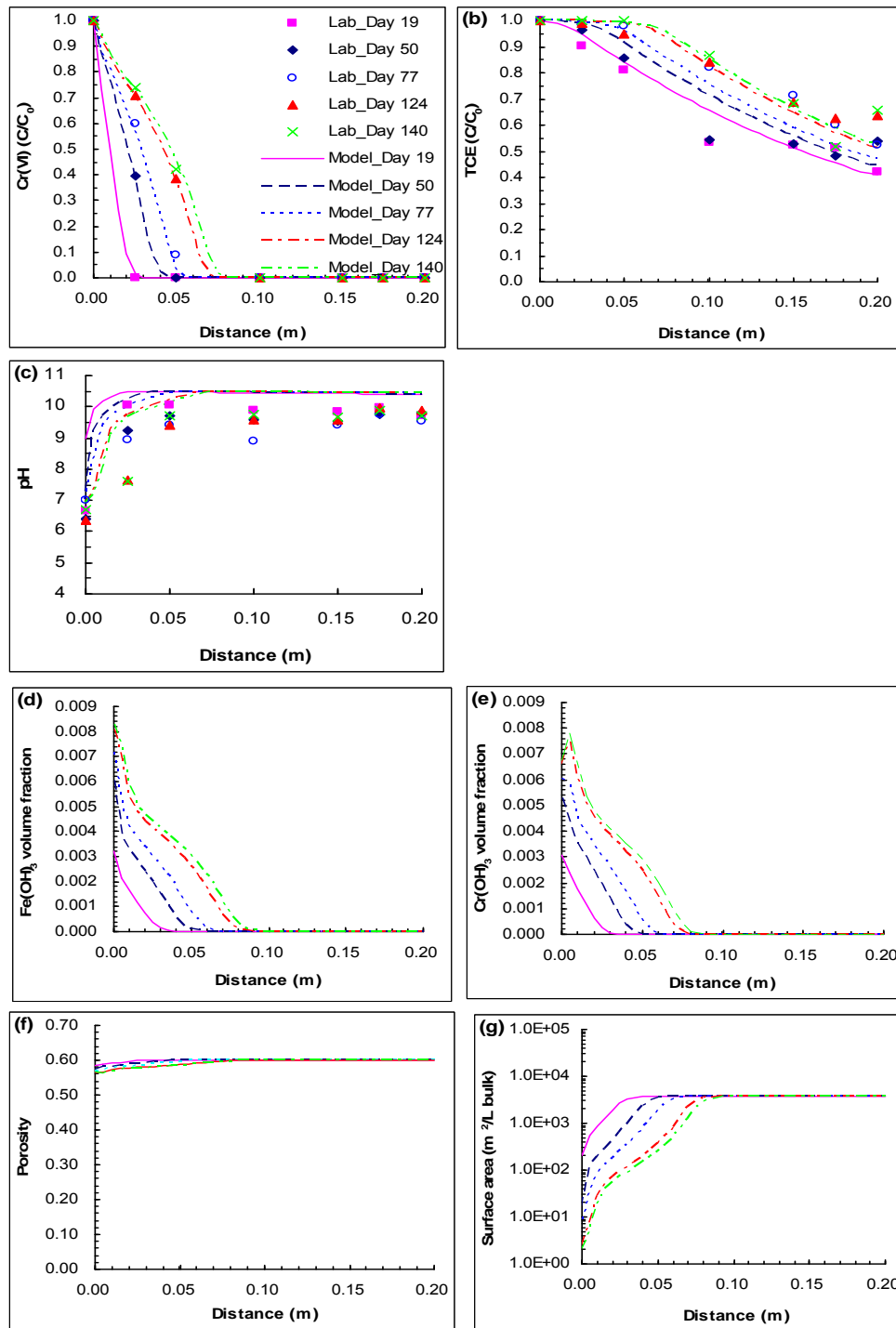


Figure 4.5 Laboratory and simulated profiles for column D: (a) Cr(VI), (b) TCE, and (c) pH, (d) Fe(OH)₃(am) volume fraction (e) Cr(OH)₃(am) volume fraction, (f) porosity, and (g) reactive surface area.

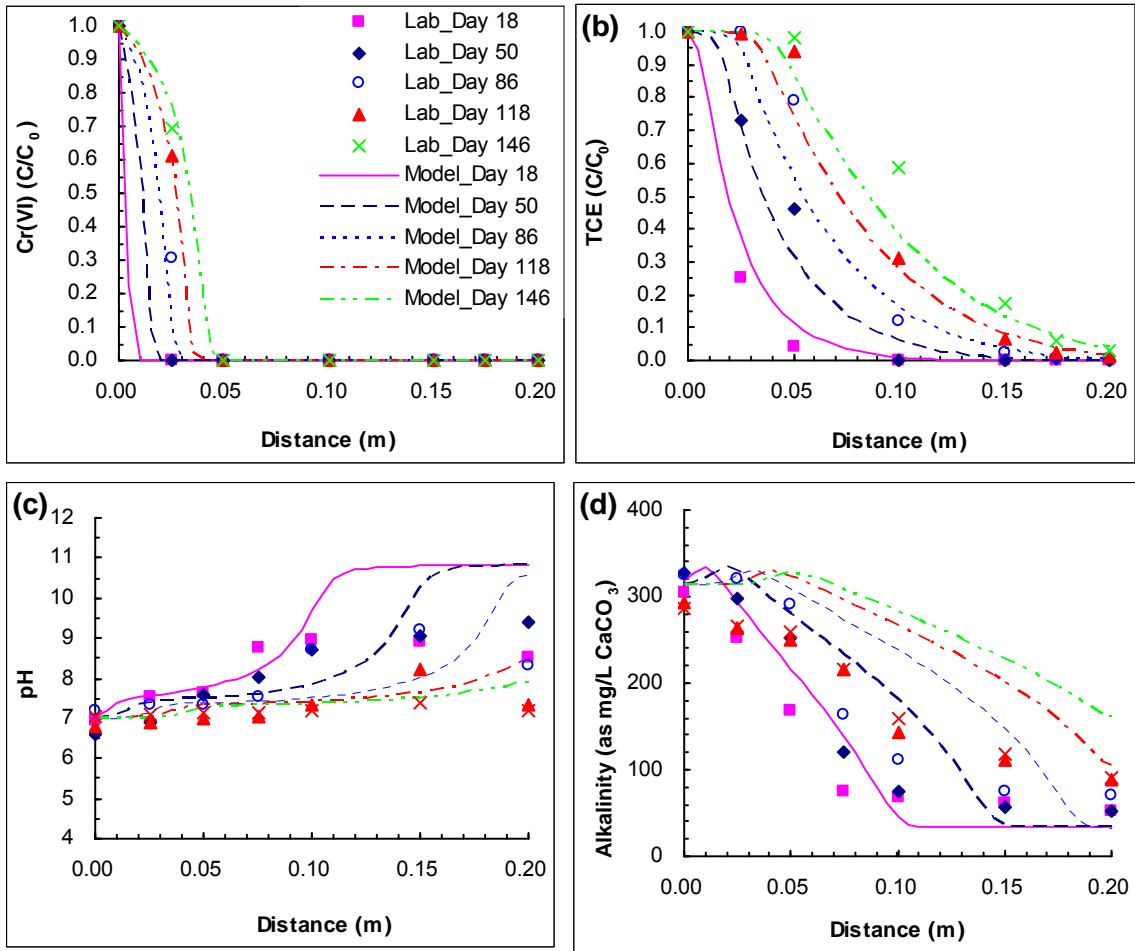


Figure 4.6 Laboratory and simulated profiles for column E: (a) Cr(VI), (b) TCE, (c) pH, and (d) alkalinity.

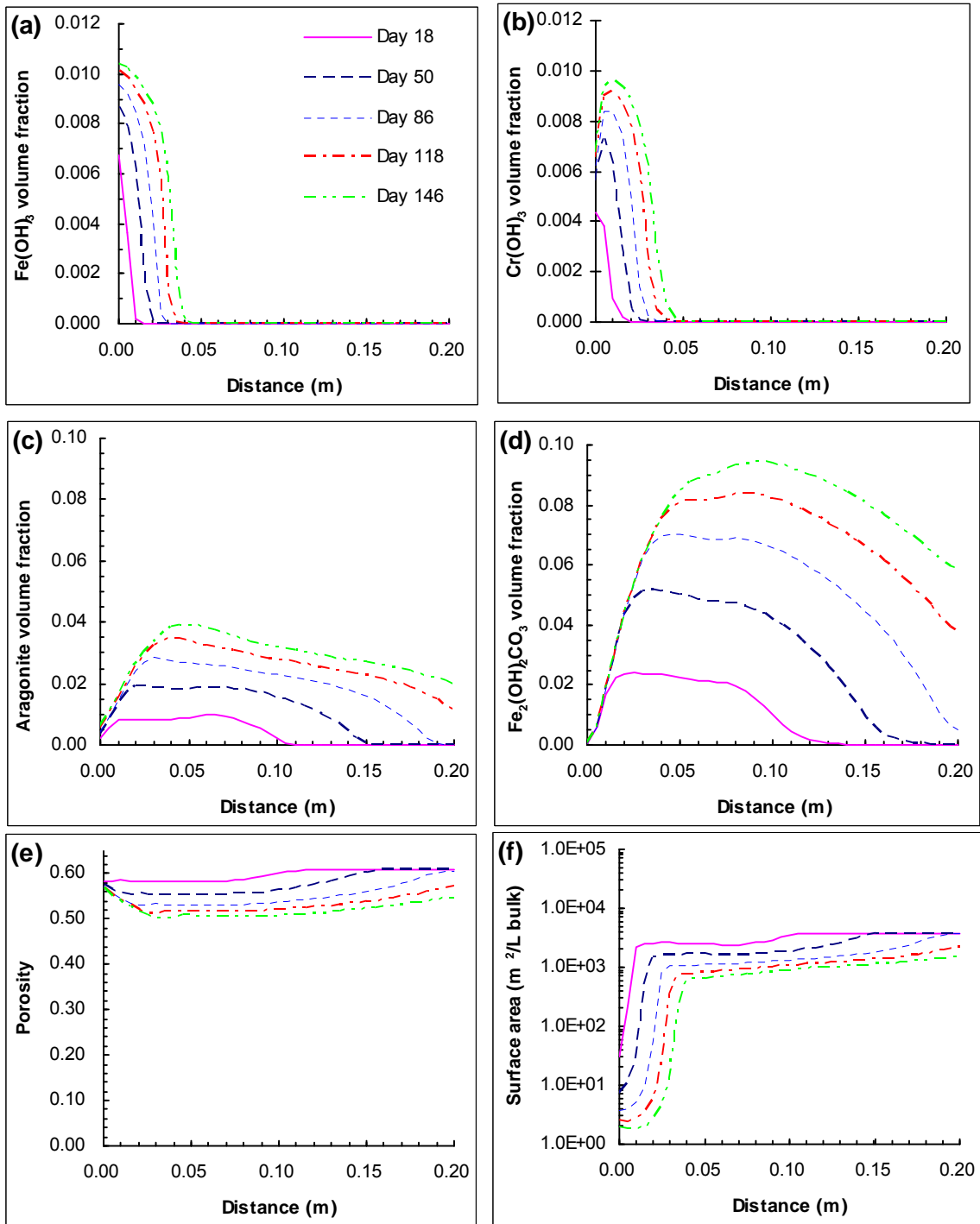


Figure 4.7 Simulation profiles for column E: (a) Fe(OH)₃(am) volume fraction (b) Cr(OH)₃(am) volume fraction, (c) aragonite volume fraction, (d) Fe₂(OH)₂CO₃ volume fraction, (e) porosity, and (f) reactive surface area.

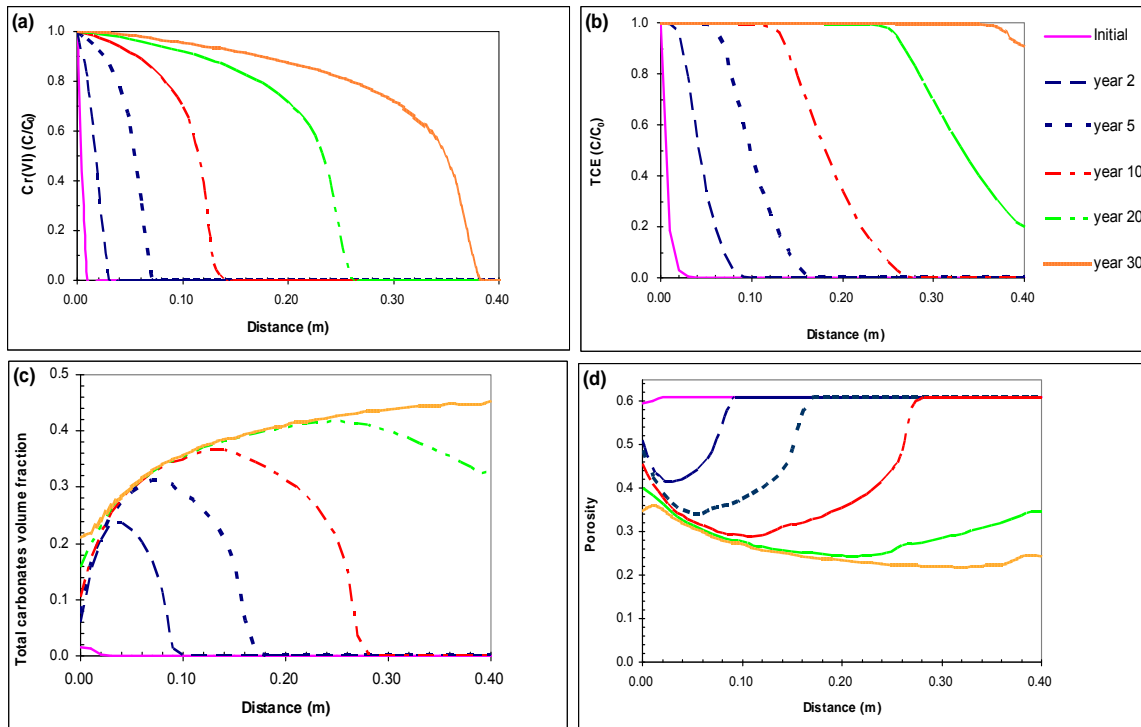


Figure 4.8 A hypothetical scenario simulating long-term performance of an iron PRB of 40 cm thick to treat groundwater containing 10 mg/L Cr(VI), 5 mg/L TCE and 300 mg/L CaCO₃ over 30 years: (a) Cr(VI) profiles, (b) TCE profiles, (c) total carbonate volume fraction, and (d) porosity

Chapter 5 Conclusions

When Cr(VI) exists as the only contaminant, it is reduced very quickly by granular iron; no Cr(VI) was detected at ca. 3hr of residence time when 508 PV of solution had passed through the column. Cr(VI) profiles migrated from the influent end further into the column over time, suggesting progressive passivation of iron in the lower portion of the column. The gradual increase in corrosion potential at Port I (+180 mV shift) with the migration of Cr(VI) profiles indicates the formation and accumulation of higher valent iron oxides, such as hematite and goethite, together with Cr(III) reaction products, on the iron surface as passivating material. Raman spectroscopic measurements at the conclusion of the experiment confirmed the presence of passive iron oxide films.

When Cr(VI) and TCE exist as co-contaminants, migration of both Cr(VI) and TCE profiles were observed. For Cr(VI), the rate of migration was similar to the rate where Cr(VI) was the only contaminant. A similar gradual increase in corrosion potential at Port I, and detection of iron passive oxides, together with Cr(III) products, at the end of the experiment were observed. The results suggest that the Cr(VI) reduction rate was decreased by the passivation of the metallic iron by Fe(III)/Cr(III) reduction products, and further, that TCE did not affect Cr(VI) reduction significantly. On the other hand, the presence of Cr(VI) affected TCE degradation significantly, resulting in further migration of the TCE profiles. Furthermore, over time and with the continued addition of solution, the TCE profiles became progressively less consistent with the pseudo-first-order rate model. The migration of the TCE profiles can be divided into two segments. The first segment is near the influent end, where the TCE degradation rate decreased rapidly until there was eventually no degradation at late time. In the second segment, beyond the first, TCE degradation continued to follow pseudo-first-order kinetics. The migration of Cr(VI) and TCE profiles suggest that Cr(VI) reduction is much more competitive than TCE degradation. The first segment of the TCE profiles is expected to extend further into the column with the migration of the Cr(VI) profiles over time.

The addition of dissolved CaCO₃ enhanced TCE and Cr(VI) reduction significantly by the pH-buffering effect. The iron was, however, passivated from the initial enhancement by the formation of passivating oxides and secondary carbonate precipitates. The enhancement was much greater than the passivation over the experimental period. For example, for columns receiving CaCO₃, the half-lives of TCE degradation decreased significantly from 2.4 hr and 3 hr before CaCO₃ addition to 30 min at the beginning of CaCO₃ addition. Over time, the TCE profiles in column receiving TCE + CaCO₃ and the second segment of TCE profiles in column receiving TCE + Cr(VI) + CaCO₃

migrated. There was a transition zone where the iron was slightly active for TCE degradation at the end of the experiment for column E receiving CaCO_3 , and there was no such zone for column D without CaCO_3 . Cr(VI) profiles migrated up to 10 cm along the columns for columns without CaCO_3 (columns A and D), but only 5 cm along the columns when CaCO_3 was added (columns B and E).

The modified MIN3P model reproduced the observations from the columns in which TCE co-exists with Cr(VI) and CaCO_3 quite well, suggesting that this model has applicability to predict the long-term performance of an iron PRB to treat groundwater containing Cr(VI), TCE and CaCO_3 . However, there are some potential limitations existing in the modified MIN3P model, such as inconsistent volume fractions of secondary carbonate minerals and Fe(III)/Cr(III) products between experimental measurements and model simulation results, reactive surface area concept, and the inability to represent the changes in iron corrosion rate. The simulation by this model of hypothetical iron PRB to remediate groundwater where TCE co-exists with Cr(VI) in the presence of CaCO_3 suggests that a thicker wall and a higher porosity material should be considered for the design of iron PRB to secure the complete remediation of TCE in long-term.

References

- Alowitz, M.J., and M. Scherer. 2002. Kinetics of Nitrate, Nitrite, and Cr(VI) Reduction by Iron Metal. *Environmental Sciences and Technology*. 36, 299-306.
- Arnold, W.A., and A. L. Roberts. 2000. Pathways and Kinetics of Chlorinated Ethylene and Chlorinated Acetylene Reaction with Fe⁰ Particles. *Environmental Sciences and Technology* 34, 1794-1805.
- Astrup, T., S. L. S. Stipp, and T.H. Christensen. 2000. Immobilization of Chromate from Coal Fly Ash Leachate Using an Attenuating Barrier Containing Zero-valent Iron. *Environmental Science and Technology*, 34 (19), 4163-4168.
- Boucherit, N., A. H. Goff, and S. Joiret. 1992. Influence of Ni, Mo, and Cr on Pitting Corrosion of Steels Studied by Raman Spectroscopy. *Corrosion*. 48 (7), 569-579.
- Blowes, D.W., C.J. Ptacek, and J.L. Jambor. 1997. In-Situ Remediation of Cr(VI) Contaminated Groundwater Using Permeable Reactive Walls: Laboratory Studies. *Environmental Science and Technology*, 31 (12), 3348-3357.
- Blowes, D.W., R.W. Gillham, C.J. Ptacek, R.W. Puls, T.A. Bennett, S.F. O'Hannesin, C.J. Hanton-Fong, and J.G. Bain. 1999a. An In-Situ Permeable Reactive Barrier for the Treatment of Hexavalent Chromium and Trichloroethylene in Ground Water: Volume 1, Design and Installation. EPA/600/R-99/095a, U.S. Environ. Prot. Agency, Washington, D.C., September 1999.
- Blowes, D.W., R.W. Puls, R.W. Gillham, C.J. Ptacek, T.A. Bennett, J.G. Bain, C.J. Hanton-Fong, and C.J. Paul. 1999b. An *In Situ* Permeable Reactive Barrier for the Treatment of Hexavalent Chromium and Trichloroethylene in Ground Water: Volume 2, Performance Monitoring. EPA/600/R-99/095b, U.S. Environmental Protection Agency, Washington, DC, September 1999.

- Blowes, D.W., C.J. Ptacek, S.G. Benner, C.W.T. McRae, T.A. Bennett, and R.W. Puls. 2000. Treatment of Inorganic Contaminants Using Permeable Reactive Barriers. *Journal of Contaminant Hydrology*, 45, 123-137.
- Blowes, D. 2002. Tracking Hexavalent Cr in Ground water. *Science*, 295, 2024-2025.
- Bonin, P. M. L., M. Odziemkowski, E. J. Reardon, and R. W. Gillham. 2000. In situ identification of carbonate-containing green rust on iron electrodes in solutions simulating groundwater. *Journal of Solution Chemistry*. 29 (10) 1061-1074.
- Brunauer, S., P.H. Emmett, and E. Teller. 1938. Adsorption of Gases in Multimolecular Layers. *Journal of American Chemical Society*, 60, 309-319.
- EnviroMetal Technologies Inc. (ETI), <http://www.eti.ca> (accessed September 2006).
- Erdem, M., F.Gur, and F. Tumen. 2004. Cr (VI) reduction in aqueous solutions by siderite. *Journal of Hazardous Materials*, B113, 217-222.
- Farrell, J., Kason, M., Melitas, N., and Li, T. 2000. Investigation of the long-term performance of zero-valent for reductive dechlorination of trichloroethylene. *Environmental Science and Technology*, 34, 514-521.
- Frost, R.L., A. W. Musumeci, N. M. Martens, M. O., Adebajo, and J. Bouzaid. 2005. Raman Spectroscopy of Hydrotalcites with Sulphate, Molybdate and Chromate in the interlayer. *Journal of Raman Spectroscopy*, 36, 925-931.
- Gillham, R.W. 1999. In Site Remediation of VOC-Contaminated Groundwater Using Zero-Valent Iron: Long Term Performance. In *The 1999 Contaminated Site Remediation Conference "Challenges Posed by Urban & Industrial Contaminants" Organized by the Centre for Groundwater Studies*, Fremantle, Western Australia, March 21-25, 605-614.
- Gillham, R.W., and S.F. O'Hannesin. 1994. Enhanced Degradation of Halogenated Aliphatics by

- Zero-Valent Iron. *Ground Water*, 32 (6), 958-967.
- Gottpagar, J., E. Grulke, T. Tsang, and D. Bhattacharyya. 1997. Reductive Dehalogenation of Trichloroethylene Using Zero-Valent Iron. *Environmental Progress*, 16 (2), 137-143.
- Gui, J. and T. M. Devine. 1991. In situ vibrational spectra of the passive film on iron in buffered borate solution. *Corrosion Science*. 32 (10), 1105-1124.
- Jeen, S.W. 2005. Effects of Mineral Precipitation on Long-Term Performance of Granular Iron Permeable Reactive Barriers: Column Experiments and Numerical Simulation. Ph.D. Thesis, Department of Earth Sciences, University of Waterloo, Ontario, Canada, 232pp.
- Jeen, S.W., R. W. Gillham, and D. W. Blowes. 2006. Effects of Carbonate Precipitates on Long-Term Performance of Granular Iron for Reductive Dechlorination of TCE. *Environmental Science and Technology*, 40 (20), 6432-6437.
- Kohn, T., K.J.T. Livi, A.L. Roberts, and P.J. Vikesland. 2005. Longevity of Granular Iron in Groundwater Treatment Processes: Corrosion Product Development. *Environmental Science and Technology*, 39 (8), 2867-2879.
- Li, T., and J. Farrell. 2002. Reductive dechlorination of trichloroethene and carbontetrachloride using iron and palladized-iron cathodes. *Environmental Science and Technology* 34, 173-179.
- Liang, L., A.B. Sullivan, O.R. West, G.R. Moline, and W. Kamolpornwijit. 2003. Predicting the Precipitation of Mineral Phases in Permeable Reactive Barriers. *Environmental Engineering Science*, 20 (6), 635-653.
- Lu, Q. 2005. Effects of Oxidant (Nitrate) on the TCE Degradation by Granular Iron. M.Sc. Thesis, Department of Earth Sciences, University of Waterloo, Ontario, Canada, 57pp.
- Mackay, D. M., D. L. Freyberg, P. V. Roberts, and J.A. Cherry. 1986. A Natural Gradient

- Experiment on Solute Transport in a Sand Aquifer 1. Approach and Overview of Plume Movement. *Water Resource Research*, 22 (13), 2017-2029.
- Maslar, J.E., W.S. Hurst, W.J. Bowers Jr., J.H. Hendricks, M.I. Aquino, and I. Levin. 2001. In situ Raman spectroscopic investigation of chromium surfaces under hydrothermal conditions. *Applied Surface Science*, 180 (2001) 102-118.
- Matheson, L.J., and Tratnyek, P.G. 1994. Reductive dehalogenation of chlorinated methanes by iron. *Environmental Science and Technology*, 28(12), 2045-2053.
- Mayer, K.U. 1999. A Numerical Model for Multicomponent Reactive Transport in Variably Saturated Porous Media. Ph.D. Thesis, Department of Earth Sciences, University of Waterloo, Ontario, Canada, 286 pp.
- Mayer, K.U., D.W. Blowes, and E.O. Frind. 2001. Reactive Transport Modeling of an In Site Reactive Barrier for the Treatment of Hexavalent Chromium and Trichloroethylene in Groundwater. *Water Resources Research*, 37 (12), 3091-3103.
- Mayer, K.U., E.O. Frind and D.W. Blowes. 2001. Multicomponent reactive transport modeling in variably saturated porous media using a generalized formulation for kinetically controlled reactions. *Water Resources Research*, 38 (9), 1174, doi:10.1029/2001WR000862.
- Mackenzie, P.D., D. P. Horney, and T.M. Sivavec. 1999. Mineral Precipitation and Porosity Losses in Granular Iron Columns. *Journal of Hazardous Materials*, 68, 1-17.
- Oblonsky, L. J. and T.M. Devine. 1995. A surface enhanced Raman spectroscopic study of the passive films formed in borate buffer in iron, nickel, chromium and stainless steel. *Corrosion Science*. 37(1), 17-41.
- Odziemkowski, M.S., T.T. Schuhmacher, R. W. Gillham, and E. J. Reardon. 1998. Mechanism of oxide film formation on iron in simulating groundwater solutions: Raman spectroscopic studies. *Corrosion Science*. 40 (2/3), 371-389.

- Odziemkowski, M.S. and R. P. Simpraga. 2004. Distribution of oxides on iron materials used for remediation of organic groundwater contaminants – implications for hydrogen evolution reactions. *Canadian Journal of Chemistry*. 82 (10), 1495-1506.
- O'Hannesin, S.F., and R.W. Gillham. 1998. Long Term Performance of an In Site Iron Wall for Remediation of VOCs. *Ground Water*, 36 (1), 164-170.
- Okwi, G.J., N.R. Thomson, and R.W. Gillham. 2005. The Impact of Permanganate on the Ability of Granular Iron to Degrade Trichloroethene. *Ground Water Monitoring & Remediation*, 25 (1), 1-6.
- Orth, W.S., and R.W. Gillham. 1996. Dechlorination of Trichloroethene in Aqueous Solution Using Fe^0 . *Environmental Science and Technology*, 30 (1), 66-71.
- Pankow and J.A. Cherry. 1996. Dense Chlorinated Solvents and other DNAPLs in Groundwater. Waterloo Press. Chapter 1. (Pankow, J.F., , S. Feenstra, J.A. Cherry, and M.C.Ryan), Dense Chlorinated Solvents in Groundwater: Background and History of the Problem, pp 1-52.
- Powell, R. M., R. W. Puls, S. K. Hightower, and D. A. Sabatini. 1995. Coupled Iron Corrosion and Chromate Reduction: Mechanisms for Subsurface Remediation. *Environmental Science and Technology*, 29 (8), 1913-1922.
- Pratt, A. R., D.W. Blowes, and C.J. Ptacek. 1997. Products of Chromate Reduction on Proposed Subsurface Remediation Material. *Environmental Science and Technology*, 31 (9), 2492-2498.
- Ritter, K., M. S Odziemkowski, R. Simpraga, and R. W. Gillham. 2002. An in situ study of the role of surface films on the granular iron in the permeable iron wall technology. *Journal of Contaminant Hydrology*, 55, 87-136.
- Ritter, K., M. S Odziemkowski, R. Simpraga, R. W Gillham, and D. E. Irish. 2003. An in situ study

- of the effects of nitrate on the reduction of trichloroethylene by granular iron. *Journal of Contaminant Hydrology*, 65, 121-136.
- Roberts, A.L., L.A. Totten, W.A. Arnold, D.R. Burris, and T.J. Campbell. 1996. Reductive Elimination of Chlorinated Ethylenes by zero-Valent Metals. *Environmental Science and Technology*, 30 (8), 2654-2659.
- Schlicker, O., M. Ebert, M. Fruth, M. Weidner, W. Wust, and A. Dahmke. 2000. Degradation of TCE with Iron: The Role of Competing Chromate and Nitrate Reduction. *Ground Water*, 38 (3), 403-409.
- Standard methods for the examination of water and wastewater (16th edition). 1985. American Public Health Association, American Water Works Association, Water Environment Federation: Washington DC.
- Thieme, M. and D. Scharnweber. 1993. The Hydrothermal Chromate Treatment of Carbon Steel, the Electrochemical and Surface Analytical Characterization of Protecting Oxide Layers. *Corrosion Science*, 34(3), 363-381.
- U.S. Environmental Protection Agency, [http:// www.epa.gov/safewater/mcl.html](http://www.epa.gov/safewater/mcl.html) (assessed May 2006)
- Yabusaki, S., K. Cantrell, B. Sass, and C. Steefel. 2001. Multicomponent Reactive Transport in an In Situ Zero-Valent Iron Cell. *Environmental Science and Technology*, 35 (7), 1493-1503.
- Zhang, Y., and R.W. Gillham. 2005 Effects of Gas Generation and Precipitates on Performance of Fe⁰ PRBs. *Ground Water*, 43 (1), 113-121.